Institut für Nutzpflanzenwissenschaften und Ressourcenschutz (INRES)
Pflanzenkrankheiten und Pflanzenschutz

Hyperspectral in-field sensing of foliar diseases of wheat

Dissertation

zur Erlangung des Grades

Doktor der Agrarwissenschaften (Dr. agr.)

der Landwirtschaftlichen Fakultät

der Rheinischen-Friedrich-Wilhelms-Universität Bonn

von

David Bohnenkamp

aus

Münster

Bonn 2020

Referentin: Prof. Dr. Anne-Katrin Mahlein
Korreferent: Prof. Dr. Jens Léon

Tag der mündlichen Prüfung: 23.10.2020

Angefertigt mit Genehmigung der Landwirtschaftlichen Fakultät der Universität Bonn

Summary

The major aim of this work was to prove the suitability of hyperspectral sensors for the detection of foliar diseases of wheat under field conditions. Hyperspectral sensors, measurement protocols and analysis methods were evaluated both under controlled and field conditions. Findings from controlled conditions were used to gain knowledge about the requirements for successful measurement routines using hyperspectral sensors and to transfer this knowledge to field measurements. Therefore, hyperspectral measurements were performed on different scales, under laboratory conditions (measuring distance 11-45 cm) as well as under field conditions using a ground-based vehicle (50 cm) and an unmanned aerial vehicle (UAV drone) (20 m).

Under controlled conditions, the hyperspectral dynamic of five different foliar diseases of wheat was investigated in detail. Certain spectral changes were found to be characteristic for a specific disease and defined as turning points. The turning points of each disease were combined in a spectral library. The spectral library in combination with algorithms from machine learning was successfully used to detect, identify and quantify the diseases on wheat leaves. A spatial referencing method based on a non-linear 2D polynomial transformation model was developed to perform a retrospective analysis of diseased pixels on wheat leaves. By retrospectively going back in time and automatically choosing the same pixels over different measurement days, an earliest detectability test for different diseases was performed. The pure spore spectra of brown rust and yellow rust were used as input data for a least-squares factorization to differentiate between the two diseases by a signal decomposition. The mixed signal of a diseased plant leaf was decomposed, and the presence of pure spore spectra was detected to identify the disease. A deep learning approach using 3D convolutional neural networks was used to perform a disease detection and identification on hyperspectral data without previous data labelling.

The findings from laboratory experiments were used to conceptualize two measurement field platforms. Data preprocessing routines were developed with the purpose to normalize and process the field data. Bringing the data into a comparable form allows to compare the images of one measurement day and on different measurement dates. The data was analyzed using algorithms from machine learning. A feature selection was performed to describe certain wavebands that can be used for yellow rust detection as most significant disease during vegetation period 2018. The classification of yellow rust was successfully performed both on the ground and UAV scale with high classification accuracies. The outcome of this study proved the suitability, and with further improvement of analysis methods, the potential of hyperspectral sensors for an in-field disease detection in winter wheat.

Kurzfassung

Das Ziel der vorliegenden Arbeit war es, die Eignung von Hyperspektralsensoren zur Detektion von Blattkrankheiten des Weizens im Feld zu erproben. In Experimenten, durchgeführt unter kontrollierten Bedingungen, wurden Messroutinen etabliert, die eine Übertragung von Hyperspektralmessungen vom Labor in das Feld ermöglichen. Hierfür wurden Messungen auf verschiedenen Skalen durchgeführt. Unter kontrollierten Bedingungen lagen die Messdistanzen zwischen 11-45 cm. Feldmessungen wurden mit einer bodenbasierten Plattform auf 50 cm Messhöhe und einer Drohne auf 20 m Flughöhe durchgeführt. Unter kontrollierten Bedingungen wurden die spektralen Dynamiken von fünf verschiedenen Blattkrankheiten des Weizens detailliert untersucht. Krankheitsspezifische Veränderungen des Pflanzenspektrums konnten identifiziert und als Wendepunkte (Turning Points) für jede individuelle Pathogenese definiert werden. Für diese Wendepunkte der Blattkrankheiten wurde eine spektrale Bibliothek erstellt. Durch die Anwendung der spektralen Bibliothek (eingesetzt als Trainingsdaten für Klassifikationsalgorithmen) auf weitere hyperspektrale Datensätze, war es möglich Krankheiten zu detektieren, zu identifizieren und zu quantifizieren. Mit einer räumlichen Referenzierungsmethode, basierend auf einem 2D polynomialen Transformationsmodell, konnte eine retrospektive Analyse von kranken Pixeln auf Weizenblättern durchgeführt werden. Durch die retrospektive Analyse in Kombination mit einer automatischen Auswahl der gleichen Pflanzenpixel an verschiedenen Messtagen mittels Transformationsmodell, war eine Aussage zur frühestmöglichen Detektierbarkeit einer Krankheit möglich. Die reinen Sporenspektren von Braun- und Gelbrost dienten als Trainingsdaten für eine Methode der kleinsten Quadrate, um zwischen den beiden Krankheiten durch eine Zerlegung des Spektrums in seine reinen Komponenten zu unterscheiden. Zur Bestimmung der Krankheit wurde das Spektrum eines infizierten Blattes faktorisiert und auf Anwesenheit krankheitsspezifischer Signaturen untersucht. Ein Deep Learning Ansatz, basierend auf 3D konvolutionellen neuronalen Netzen, wurde genutzt, um eine Krankheitsdetektion und –identifikation in hyperspektralen Datensätzen durchzuführen, die nicht auf vorherigem Datenlabelling beruht.

Aufbauend auf den Laborergebnissen wurden zwei Feldmessplattformen etabliert. Datenprozessierungsroutinen wurden entwickelt, um Felddaten zu normalisieren und sie in eine vergleichbare Form zu bringen. Dies ermöglichte eine Vergleichbarkeit von Datensätzen, die an verschiedenen Messtagen aufgenommen wurden. Die Datensätze wurden mit verschiedenen Ansätzen des Machine Learning analysiert. Eine Feature Selection wurde durchgeführt, um krankheitsspezifische Wellenlängen für den in Saison 2018 vorherrschenden Gelbrost zu bestimmen und diese zur Detektion im Feld zu nutzen. Die Erkennung von Gelbrost konnte erfolgreich auf beiden Feldplattformen mit einer hohen Gesamtgenauigkeit erreicht werden. Die Erkenntnisse von verschiedenen Skalenebenen zeigen, dass eine Krankheitserkennung mit Hyperspektralsensoren im Feld möglich ist und im Zuge sich stetig verbessernder Analysemethoden ihr großes Potential auf diesem Gebiet entfalten kann.

Table of contents

Index of abbreviations ..... **VII**

Cumulative publications ..... **VIII**

1 Introduction **9**

1.1 Precision agriculture for plant protection measures 9

1.2 Site-specific application approaches 10

1.3 Sensor technology for hyperspectral imaging 13

1.4 Disease interaction determines the optical properties of wheat leaves 15

1.4.1 Wheat disease detection - controlled conditions 21

1.4.2 Wheat disease detection - field conditions 23

1.5 Effect of weather conditions on hyperspectral field measurements 25

1.6 Effect of biological heterogeneity of wheat on hyperspectral field measurements 28

1.7 Effect of the measurement scale on hyperspectral in-field wheat disease detection 30

1.8 Artificial intelligence as a tool for data analysis 33

1.9 Objectives of the study 36

2 Hyperspectral library of foliar diseases of wheat **37**

2.1 Abstract 37

2.2 Introduction 37

2.3 Materials and methods 40

2.4 Results 45

2.5 Discussion and conclusion 55

2.6 Acknowledgements 58

2.7 References 58

3 Spatial referencing of hyperspectral images for tracing of plant disease symptoms **62**

3.1 Abstract 62

3.2 Introduction 62

3.3 Materials and methods 66

3.4 Results 71

3.5 Discussion 75

3.6 Conclusion 77

3.7 Acknowledgements 77

3.8 References 77

4 Hyperspectral signal decomposition and symptom detection of wheat rust disease at the leaf scale using pure fungal spore spectra as reference **81**

4.1 Abstract 81

4.2 Introduction 81

4.3 Materials and methods 84
4.4 Results 88
4.5 Discussion and conclusion 91
4.6 Acknowledgements 94
4.7 References 95
5 Detection of plant diseases in hyperspectral images by 3D-CNN 98
5.1 Abstract 98
5.2 Introduction 98
5.3 Materials and methods 100
5.4 Results and discussion 104
5.5 Conclusion 108
5.6 References 108
6 In-field detection of yellow rust in wheat on the ground canopy and UAV scale 111
6.1 Abstract 111
6.2 Introduction 112
6.3 Materials and methods 114
6.4 Results and discussion 124
6.5 Conclusion 136
6.6 Acknowledgements 137
6.7 References 137
7 Discussion and conclusion 141
8 References 151
9 Acknowledgements 158

Index of abbreviations

BR Brown rust (caused by *Puccinia triticina*)

CNN Convolutional Neural Network

DL Deep Learning

DTR Tan spot (caused by *Drechslera tritici-repentis*)

GIS Geo Information System

GPS Global Positioning System

HI Hyperspectral Imaging

HIS Hyperspectral Imaging sensors

ML Machine learning

NIR near-infrared range (700-1000 nm)

PM Powdery mildew (caused by *Blumeria graminis* f. sp*. tritici*)

RGB Red light (560-700 nm), green light (520-560 nm) and blue light (400-490 nm)

SAM Spectral angle mapper

STB Septoria tritici blotch (caused by *Zymoseptoria tritici*)

SVM Support vector machine

SWIR short-wave-infrared range (900-2500 nm)

UAV Unmanned aerial vehicle

VI Vegetation index

VIS Visible spectrum (400-700 nm)

VNIR Visible spectrum and near-infrared spectrum (400-1000 nm)

YR Yellow rust (caused by *Puccinia striiformis*)

Cumulative publications

1. Bohnenkamp, David; Behmann, Jan; Steiner, Ulrike; Mahlein, Anne-Katrin (2019). Hyperspectral library of foliar diseases of wheat. Submitted to: *Phytopathology*. Submission date: 12-Sep-2019. Current status: Major Revision. Resubmission planned for June 2020.
2. Behmann, Jan; Bohnenkamp, David; Paulus, Stefan; Mahlein, Anne-Katrin (2018b): Spatial referencing of hyperspectral images for tracing of plant disease symptoms. In: *Journal of Imaging* 4 (12), S. 143. DOI: 10.3390/jimaging4120143.
3. Bohnenkamp, David; Kuska, Matheus; Mahlein, Anne-Katrin; Behmann, Jan (2019a): Hyperspectral signal decomposition and symptom detection of wheat rust disease at the leaf scale using pure fungal spore spectra as reference. In: *Plant Pathology* 68 (6), S. 1188–1195. DOI: 10.1111/ppa.13020.
4. Behmann, Jan; Bohnenkamp, David; Mahlein, Anne-Katrin (2019): Detection of plant diseases in hyperspectral images by 3D-CNN. Submitted to: *MDPI Sensors*. Submission date: 12-Sep-2019. Current status: Minor Revision.
5. Bohnenkamp, David; Behmann, Jan; Mahlein, Anne-Katrin (2019b): In-Field detection of yellow rust in wheat on the ground canopy and UAV scale. In: *Remote Sensing* 11 (21), S. 2495. DOI: 10.3390/rs11212495.

Parts of the introduction are published in *Phytopathology Research*:

> Bock, Clive H.; Barbedo, Jayme G. A.; Del Ponte, Emerson M.; Bohnenkamp, David; Mahlein, Anne-Katrin (2020): From visual estimates to fully automated sensor-based measurements of plant disease severity: status and challenges for improving accuracy. In: *Phytopathology Research* 2 (9). DOI: 10.1186/s42483-020-00049-8.

1 Introduction

1.1 Precision agriculture for plant protection measures

Precision agriculture in crop production can be described as the correct assessment and reaction to heterogeneity in the field. Today agriculture is used to once novel approaches like global positioning systems and the Internet of Things. These technologies are integrated in the daily routines of crop management. Meanwhile agricultural tools and data platforms are developed with high pressure and enable a more economic and ecological agricultural practice (West et al. 2003). Main areas of interest are field cropping measures like seeding, fertilization or plant protection. There is a high demand for techniques that are able to ensure both, a site-specific monitoring of parameters within field and a site-specific reaction to the monitored heterogeneity. Depending on the interrogation, investigations have to be performed on different scales: the ground canopy scale, the UAV scale (drones, fixed wings) and the satellite scale. Traditional agricultural management practices operate under the assumption that the demand for an agricultural measure is distributed homogeneously over the entire field. Today, the chemical plant protection measures are under high discussion, but the crop yield needs to be protected from diseases and pests. Modern crop varieties are no product of natural evolution. They have been selected intensively for high yield over centuries. Compared to their wild forms, the most high-yield varieties are less resistant to pathogens, viruses and insects that cause yield losses (Boyd et al. 2013; Parnell et al. 2017). Plant diseases reduce the quality and quantity of agricultural products, thus resulting in increased costs for crop production and the value chain (Bos und Parlevliet 1995). First plant disease patches are often disparately allocated within one field and homogeneous application of a chemical compound might not be necessary (West et al. 2003). So far, a precise and early detection of a plant disease is still challenging. To fulfil the demands of integrated crop protection (careful consideration of all available plant protection methods and subsequent integration of appropriate measures that discourage the development of populations of harmful organisms and keep the use of plant protection products and other forms of intervention to levels that are economically and ecologically justified and reduce or minimize risks to human health and the environment), it is important to detect, identify and capture the accurate state of disease occurrence and severity and to monitor disease spread in fields by visual assessments (Bock et al. 2010; De Boer und López 2012; Mahlein 2016). With regard to the inevitable subjectivity of human raters, disease ratings are error prone and influenced by the individual rater and primary

infection sites are often not obvious (Nutter and Schultz 1995; Nutter et al. 2006; Bock et al. 2010). Objective disease detection techniques can be realized by new automated methods with high sensitivity, specificity and reliability (Mahlein et al. 2018). Automated detecting methods can consist of a sensory system in combination with an analysis pipeline including computational power and detection algorithms. Spectral sensors offer potentials for a site-specific real-time detection of diseases. Therefore, it is crucial for a sensor to be highly specific in detection of single diseases.

The current thesis focused on the detection, identification and quantification of wheat diseases. The global wheat production system is, among others, limited by foliar diseases that cause severe economic losses each year (Oerke 2006; Torriani et al. 2015). The most important wheat diseases are tan spot (DTR), septoria tritici blotch (STB), brown rust (BR), yellow rust (YR) and powdery mildew (PM). In German winter wheat cropping systems, fungicide applications are planned considering the cropping region, the weather conditions and the suitable infection conditions (Miedaner 2018). Depending on the region and the present conditions during the year, one to three fungicide applications are conducted. In regions with comparatively moist weather conditions (Schleswig-Holstein, Mecklenburg-Hither Pomerania) three fungicide applications in winter wheat are the rule while in regions that are characterized by pre-summer droughts usually only one fungicide application is conducted (Miedaner 2018). In years with an early occurrence of YR, high pressure of eyespot, STB and DTR or high infection risk for fusarium head blight, two fungicide applications are the rule. As this strategy has economic benefits, large farms prefer this twofold strategy (Miedaner 2018). A reduction of the number of fungicide applications leads inevitably to a higher demand for the right time point of applications. In this regard, forecasting systems actually do help and sensors could help to optimize the conduction of plant protection measures depending on the present weather conditions and the current field conditions in the future.

1.2 Site-specific application approaches

The basis for navigation and autonomous driving applications are Geo Information Systems (GIS) based on data from geographic coordinates (Clarke 1986). Numerous automated approaches and intelligent machines, like agricultural robots, autonomous tracking systems and others have been invented and are the focus of research and development in modern agricultural techniques (Robert 2016). As part of the agricultural digitalization, increasing

computer power, GIS, global networks, sensitive optical sensor systems, robotic and actuator technologies have been developed (Suprem et al. 2013).

The goal of a plant protection measure considering the spatial variability of diseases in one field can only be addressed by robust disease mapping systems and plant phenotyping methods (Mahlein et al. 2018). Successful approaches of site-specific application measures in the field were shown for fertilizers, growth regulators and a selective weed control system (Reckleben 2014; Fernández-Quintanilla et al. 2018). The basis for site-specific disease measures is the precise and reliable detection of the respective disease. Optical sensors are able to identify primary disease foci and areas differing in disease incidence and can, in addition to this, even characterize disease symptom types (Mahlein et al. 2010; Mahlein et al. 2012; Leucker et al. 2016). Various investigations show that different types of optical sensors can be used to accelerate the assessment of plant diseases and other field parameters (Hillnhütter et al. 2011; Liebisch et al. 2015; Brugger et al. 2017; Mahlein et al. 2019). The majority of so far conducted research indicates that hyperspectral imaging sensors (HIS) offer high potentials for improving crop measurements under environmental conditions in the field (Whetton et al. 2018a; Whetton et al. 2018b; Yu et al. 2018). After the successful detection and identification of the disease as a basis, a measurement must be derived. An interface has to convert the detection into a site-specific plant protection measure. The success of the conduction is depending on the technology. Site-specific application approaches for plant protection measures require an adapted syringe that is able to apply a chemical compound by accessing a single nozzle (or a few nozzles) of the system to be as precise as possible. A possible workflow of the derivation of a site-specific plant protection measure is shown in Figure 1. The first step is the detection of a certain disease. As part of the spatial mapping of the disease in the field, a global positioning system (GPS) is essential to generate a site-specific distribution map. This application map could then be used to apply a fungicide to individual zones in the field. As multispectral sensors combine low costs and an easy implementation of the data to the application system, this type of sensor is widely used for different purposes. These sensors base on the principle to determine the crop biomass through calculation on different wavebands. Due to the specific calculation of wavebands certain values called vegetation indices can be derived for crop parameter determination (Berntsen et al. 2006; Reckleben 2014). However, a sensor that meets all demands of precision farming, is not realistic. Several

sensory systems should be combined to integrate interfaces for synergy effects out of sensors, GPS, forecasting models and autonomous data analysis pipelines.

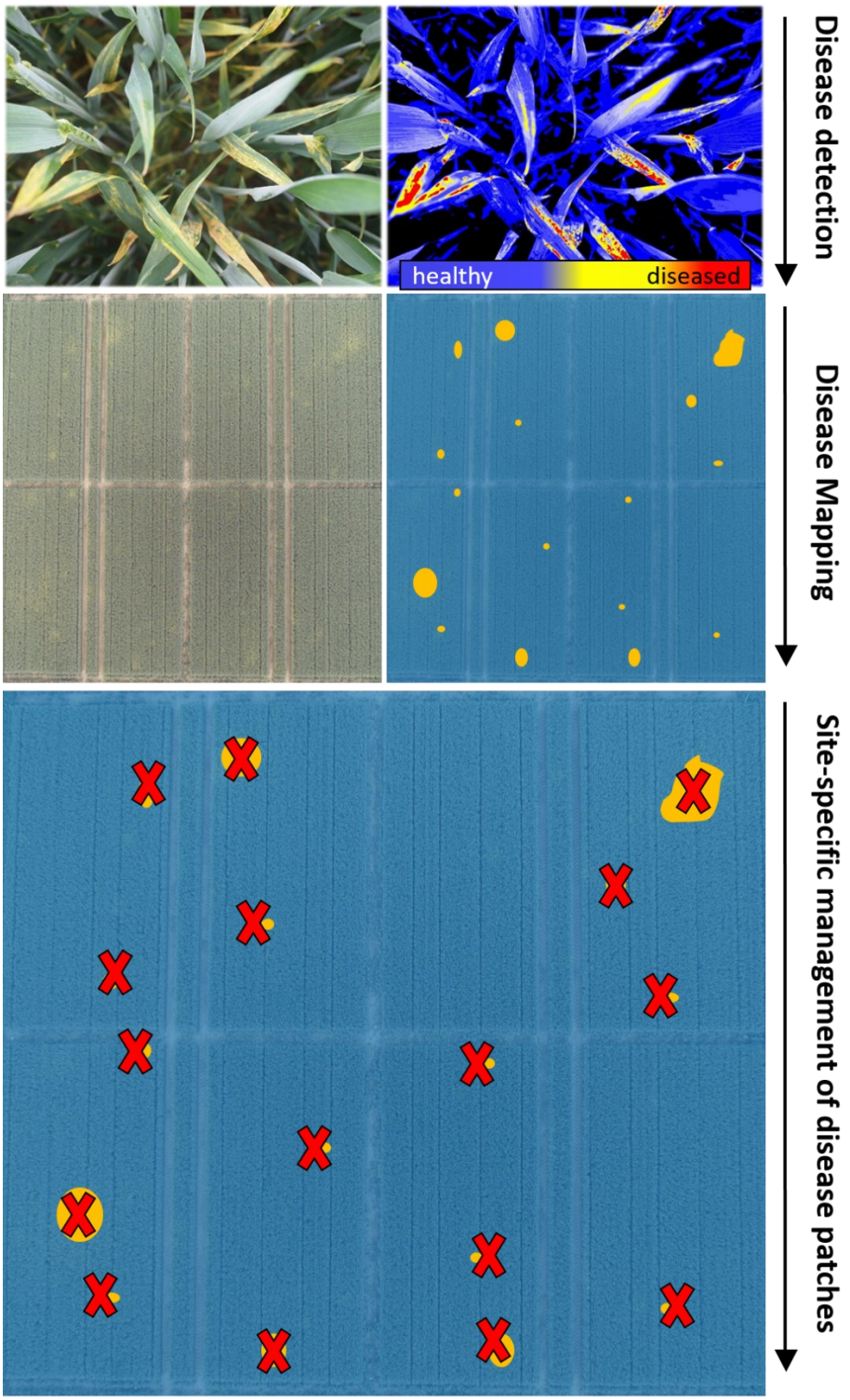

Fig. 1: Possible workflow for the derivation of a site-specific application of fungicides against yellow rust in a wheat field with a patchy distribution of the disease. First: disease detection, followed by disease mapping and the derivation of a site-specific application of a fungicide to eradicate secondary infections due to disease patches.

1.3 Sensor technology for hyperspectral imaging

Hyperspectral sensors measure the amount of light that is reflected by the crop stand. Different to conventional cameras with a red, green, and blue channel (RGB) and high spatial resolution, hyperspectral sensors include high resolution optical techniques with an increased technical resolution (Mahlein et al. 2018). Relevant spectral regions of the electromagnetic spectrum are the ultraviolet range (UV 250-400 nm), the visible range (VIS 400-700 nm), the near-infrared range (NIR 700-1000 nm) and the shortwave infrared range (SWIR 1000-2500 nm) with a spectral resolution of up to 1 nm (Steiner et al. 2008). Spectral sensors can be characterized by their spectral resolution (width of wavebands), by their spectral scale (UV, VIS, NIR and SWIR) and on the measuring principle. Non-imaging sensors average the spectral information in their field of view, while imaging sensors provide spectral information in each pixel of the image in an additional dimension z (Mahlein et al. 2018; Thomas et al. 2018). Compared to non-imaging systems and depending on their intended purpose, hyperspectral imaging sensors (HIS) are often preferred as they deliver additional information such as shape, gradient or color of the spatial dimension (Behmann et al. 2015). In many applications, multispectral sensors cover the RGB range with additional wavebands in the NIR. These sensors provide less data due to their lower spectral resolution but they are often lightweight and less cost-intensive (Mahlein et al. 2018). In contrast, HIS are more complex compared to RGB or multispectral sensors. HIS are heavier, more expensive and the measurement process takes more time which demands high standards to the measurement protocol. HI sensor setups typically consist of a hyperspectral sensor, a light source and a control unit for measuring, storing and processing the data. The light source can either be artificial (lamps of known electromagnetic characteristics) or natural (sunlight). Today the measurement unit can be mounted to vehicles, robots, drones, UAVs, tractors, airplanes, satellites and also be handheld in the field (Behmann et al. 2018a; Mahlein et al. 2018; Thomas et al. 2018; Whetton et al. 2018b; Abdulridha et al. 2019; Bohnenkamp et al. 2019a). By being able to attach the measuring units to different vehicles or measurement platforms, HI can be performed on various scales depending on the desired parameter to be measured. The suitable measurement platform is also determined by the measuring principle of the sensor. Non-imaging hyperspectral sensors provide a spectrum that is averaged over a certain area without spatial information. The focal length of the viewing angle and the distance to the target determine the size of the measured area. This might lead to inaccuracies through the lack of

spatial information pared with spectral information loss due to incongruous size of the measured area (Thomas et al. 2018). Thus an early detection of plant disease symptoms by non-imaging sensors is limited (Mahlein et al. 2012). Imaging sensors capture a one-dimensional spectral information in combination with a two-dimensional spatial information of an image. Push broom and whisk broom scanners capture the spectral information of a pixel point or a pixel line at the same time (Fig. 2). The image emerges by the movement of the sensor. These systems provide high spatial and spectral resolution, but depending on the image size, the image acquisition time may take up to minutes. This limits the application of the sensor types to motionless objects (Thomas et al. 2018). Filter-based sensors work like push and whisk broom sensors with the difference that the spatial dimensions of a full image are captured in once while only one waveband is measured at a time. This system does not require movement of the sensor and image acquisition, depending on the exposure time, is generally faster than for push and whisk broom sensors but image quality is still depending on the motionlessness of the object. Another type of sensor are hyperspectral snapshot cameras, with a measuring principle similar to RGB-cameras. Although they have a lower spatial and/or spectral resolution compared to push or whisk broom, they are promising for field application due to their fast image acquisition time (Thomas et al. 2018).

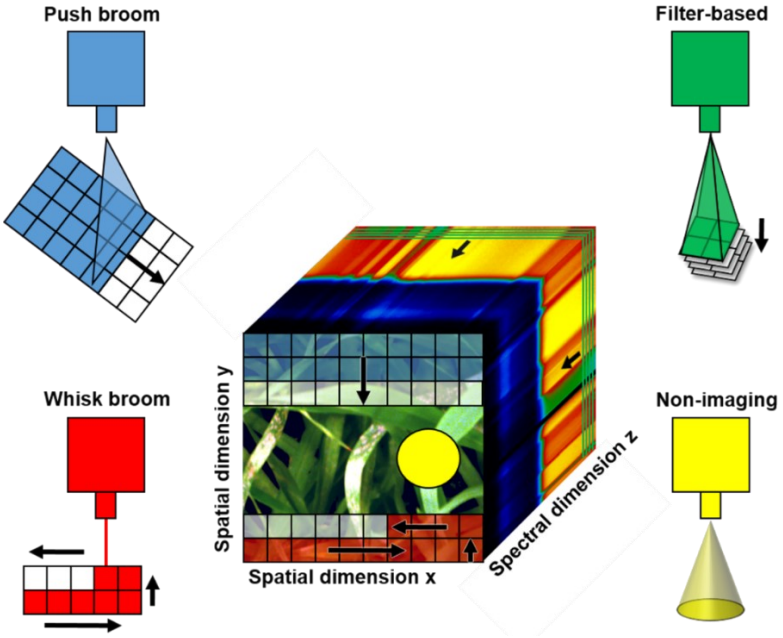

Fig. 2: Various types of sensor systems for spectroscopic image acquisition. Push broom scanner (blue), whisk broom scanner (red), filter-based sensor (green) and non-imaging sensor (yellow). The measurement principle of each sensor type is illustrated at the hyperspectral data cube in the center (According to Thomas et al. (2018)).

1.4 Disease interaction determines the optical properties of wheat leaves

The optical properties of plants are mainly determined by their reflectance, transmission and absorbance of light which are governed by leaf properties such as the waxy cuticle, the cell wall and others. Transmission and absorbance are influenced by pigments and water (Gates et al. 1965; Heim et al. 2015). The reflectance of plants is always a complex signal and caused by multiple biochemical interactions resulting in a mixed signal (Gates et al. 1965; Carter und Knapp 2001; Gay et al. 2008; Pandey et al. 2017). The reflectance in the visible range is mainly characterized by the absorption of leaf pigments such as chlorophyll, carotenoids and anthocyanins (Gay et al. 2008). NIR and SWIR stimulate molecular motions that induce a strong absorption or reflection by compounds that show characteristic spectral patterns. Additionally, the NIR reflectance of plant leaves is mainly determined by the leaf and cell structures (Gates et al. 1965; Elvidge 1990). A healthy plant shows a high reflectance in the NIR (Reckleben 2014). NIR and SWIR region show water absorption bands with strong presence in the SWIR region. Even plant water content can be determined by using SWIR imaging (Seelig et al. 2008).

The biochemical processes and the structure of plant leaves can be influenced by plant pathogens. During host-pathogen interactions, physiological and biochemical changes in the host tissue take place that might influence the optical properties in a characteristic way (Mahlein et al. 2010). The result of this interaction is often a disease symptom. The detectability of a disease is essentially influenced by the lifestyle and the resulting disease symptoms of the respective disease. In plant pathology, foliar fungal pathogens are mainly characterized as pathogens with a necrotrophic lifestyle and pathogens with a biotrophic lifestyle. Necrotrophic pathogens (e.g. *Zymoseptoria tritici*) kill their host cells and feed from the nutrients provided by the dead organic matter that enable fungal proliferation in the host tissue (Steinberg 2015). Biotrophic fungi, such as mildews and rusts, keep their hosts tissue alive as long as possible to derive nutrients from living photosynthetic active leaf area. The provision of nutrients can be ensured due to colonialization of the host and the formation of haustoria as feeding organs (Dracatos et al. 2018).

The symptom type of the disease determines the detectability of the disease. This work focuses on the detection of foliar diseases of wheat. Five diseases were investigated (Fig. 3). The diseases caused by necrotrophic pathogens are represented by tan spot (DTR) and septoria tritici blotch (STB). *Drechslera tritici-repentis* (Died.) Shoemaker is the causal agent of

tan spot. *D. tritici-repentis* grows comparatively fast and is a necrotrophic ascomycete that produces a toxin causing typical tan spots in the center of the symptom. Further symptom development can result in chlorosis or necrosis, or both depending on the race of the pathogen and the genetic background of the wheat cultivar. DTR can cause large necrotic lesions on susceptible cultivars (Tomas 1987; Dushnicky et al. 1998a; Dushnicky et. al. 1998b). *Zymoseptoria tritici* (Desm.) Quaedvliet & Crous causes *Septoria* tritici blotch (STB). The ascomycete has a biotrophic and a necrotrophic phase. The biotrophic phase is innocuous for the plant and is initially asymptomatic but the necrotrophic phase leads to collapse of cells and initial small chlorotic spots resulting in necrotic lesions that can encompass entire leaves. Pycnidia are formed in the substomatal cavities of mature necrotic lesions (Steinberg 2015). In the disease symptom, the pycnidia appear as tiny black spots formed in a necrotic lesion. STB is the key wheat disease in high input wheat cropping regions along with high rainfall. In Europe it is estimated that 70 % of fungicide use in wheat is primarily targeted towards STB (Torriani et al. 2015). Beside the formation of chlorotic spots, the biotrophic diseases become apparent by the intense production of fungal structures on the leaf surface and are represented by three different pathogens. *Puccinia triticina* Eriks. is the fungal agent of brown rust (BR). BR shows small chlorotic spots as initial symptoms about 5 days after infection. During pathogenesis chlorotic spots increase and develop uredinia in their center, bearing reddish to brown urediniospores (Bolton et al. 2008). *Puccinia striiformis* f. sp. *tritici* causes yellow rust on wheat (YR). First symptoms are tiny chlorotic spots that can occur already 6 to 8 days after infection. Copious production of urediniospores in uredinia appears about two weeks after infection on susceptible cultivars (Chen et al. 2014). *Blumeria graminis* f. sp. t*ritici* (DC.) Speer (*Bgt*) is the causal agent of wheat powdery mildew (PM). First symptoms occur 4 days after infection when tiny white spots become visible (Te Beest et al. 2008).

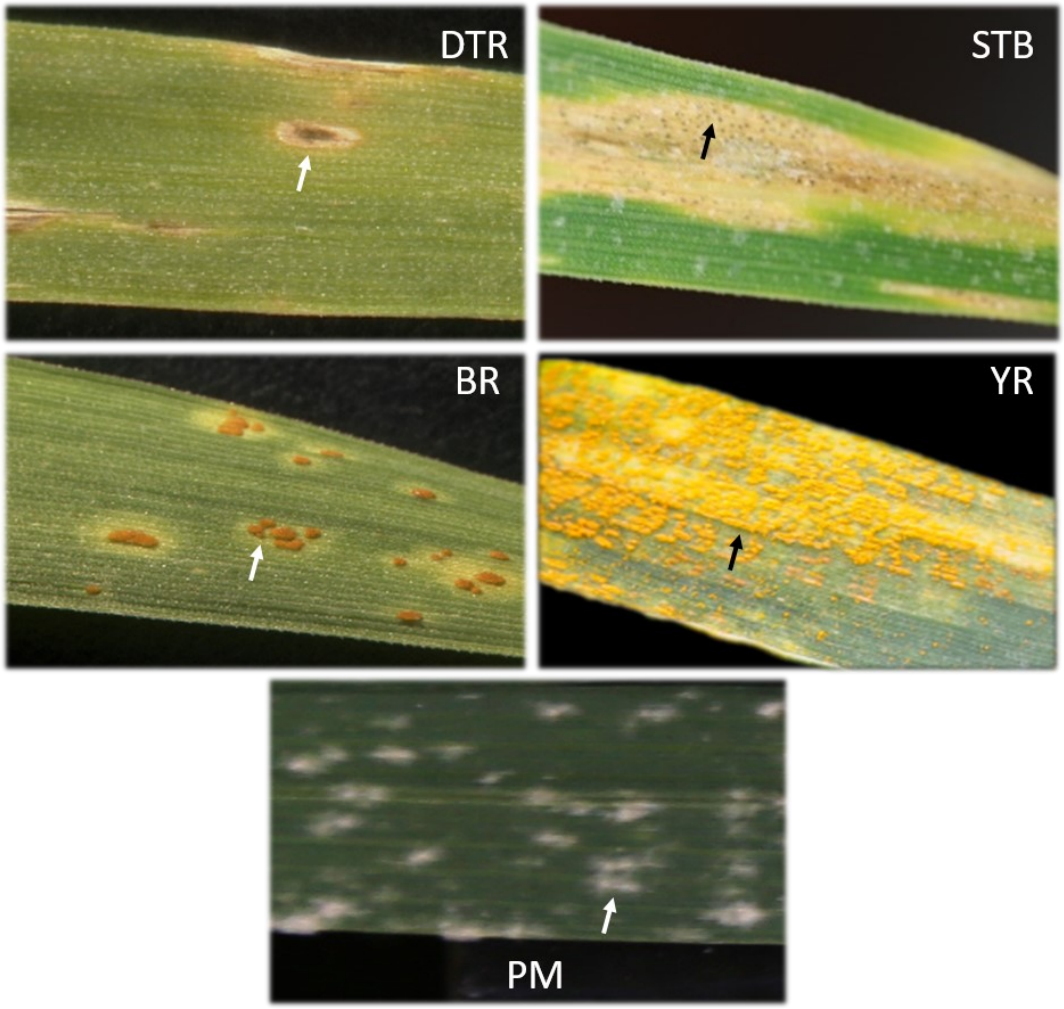

Fig 3: Symptom appearance of the different foliar diseases of wheat. Tan spot: chlorotic halo (DTR), septoria tritici blotch: pycnidia in necrotic lesions (STB), brown rust: red to brown uredinium and chlorotic halo (BR), yellow rust: yellow to orange uredinia with chlorotic tissue along leaf veins (YR), powdery mildew: hyaline to white powdery pustules (PM).

Plant diseases can be detected either indirectly through the detection of structural changes in the host tissue (chlorophyll degradation, loss of water and necrosis) or directly through the observation of the formation of fungal structures on or in the host (pigmented spores or hyphae). Each individual host-parasite interaction has a specific spatial and temporal dynamic which has an impact on different wavebands of the electromagnetic spectrum during pathogenesis (Wahabzada et al. 2015, Wahabzada et al. 2016). The individual lifestyle of fungal pathogens has a significant influence on the detectability. Interactions with necrotrophic pathogens become detectable mostly through the formation of an initial chlorosis that usually results in necrotic tissue. In this case the disease is detected indirectly because spectral peculiarities depend on the biochemical process of first chlorophyll degradation followed by cell mortification (Wahabzada et al. 2015; Mahlein et al. 2018). The

symptom of necrotrophic diseases is a lesion of dead cells of the leaf. The spectral signature is mainly influenced by the internal cell scaffold due to a loss of chlorophyll, the loss of water, cell wall structure and lignin (Elvidge 1990). Furthermore, biotrophic diseases can cause a degradation of chlorophyll and lead to chlorosis. Additionally, the formation of fungal structures on the leaf surface is common (rusts and powdery mildews). They become visible through dense formation of hyphae, spore producing units and a massive production of the spores as propagules. These propagules can either influence the reflectance of the leaf through their pigmentation with, for instance, carotenoids such as many rust diseases (Wang et al. 2018; Bohnenkamp et al. 2019b) or dense masses of hyaline spores like powdery mildews (Dean et al. 2012). The spectral signature of rust fungi can be determined by the colors of the spores (Bohnenkamp et al. 2019b). Most common, asexual urediniospores are produced polycyclic during the vegetation period. Spectral signatures of hyaline and colorless structures of powdery mildews show a characteristic parallel shift of the curve because a dense compaction of hyaline structures leads to an increased reflectance intensity due to backscattering of the incoming light. In general, the detectability of the disease is highly depending on the effect of environmental factors. Under controlled, nearly perfect laboratory conditions and with an up to date measuring setup of technique a detection, identification and quantification of a disease is possible. In contrast, the detection under field conditions is often limited by occurring weather conditions and the phenotypic appearance of the crop stand itself. A common method to detect plant stress and plant diseases is the use of classic vegetation indices (VI's) (Ashourloo et al. 2014; Behmann et al. 2014). A classic VI is the Normalized Different Vegetation Index (NDVI). The NDVI can be used to visualize the heterogeneity of the vitality of a crop stand (Behmann et al. 2014). The use of the NDVI is not suitable for the detection of a specific disease (direct detection) but it provides a relative value for the vitality of the crop stand. This value can be used for indirect disease detection (not using disease specific bands) as it visualizes diseased regions with a loss of vitality. VI's are calculated out of different wavebands that show characteristic spectral shifts in certain spectral regions. These wavebands can be derived either using multispectral sensors (that measure only the desired wavebands) or by hyperspectral sensors where the entire spectral range can be used to calculate various VI's out of the spectral range. The use of VI's allows a reduction of the data complexity. By measuring the entire spectral range, different disease specific VI's (DVI's) can be derived from the spectral information (Mahlein et al. 2013). In

literature, various works focus on the use of single or a combination of established classic VI's for disease detection (Devadas et al. 2009; Cao et al. 2013; Zheng et al. 2018a; Chen et al. 2019) but also DVI's can be powerful tools for the detection. DVI's have been developed for various diseases of different crop plants. The majority of DVI's targets the detection of biotrophic diseases such as wheat yellow rust (Zheng et al. 2018b), brown rust (Ashourloo et al. 2014), sugar beet rust (Mahlein et al. 2013) or other rust diseases like myrtle rust (Heim et al. 2019). But also DVI's for necrotrophic diseases like cercospora leaf spot have been developed (Mahlein et al. 2013). An overview of different classic and established VI's and DVI's is given in Table 1. Several studies focused on the detection of rust diseases of wheat such as yellow and brown rust (Ashourloo et al. 2014; Zheng et al. 2018b). The robustness of the detection is often limited to the measuring conditions and the pre- or absence of other diseases and abiotic stresses. Zheng et al. (2018a) described that VI's for YR detection might be only suitable for several or even one specific growth stage of wheat (sprouting or flowering) or the developmental stage of the disease (chlorosis or sporulation). YR disease starts with yellow chlorotic spots as initial symptoms. With further development YR starts to produce masses of spores in uredinia. A high dynamic in the disease appearance is present. This limits the potential and the time of application for one specific DVI. Desirable are DVI's with robustness amongst different growth stages (Zheng et al. 2018a). Regardless of the kind of sensor used for the detection, optical measurements always depend on characteristic spectral features that must be analyzed in the correct way.

Table 1: Examples of spectral vegetation indices that were used to detect plant diseases. Classic VI's were developed to provide information about the general vitality of a crop canopy, disease specific VI's (DVI's) were developed to detect a certain disease including disease specific wavebands.

Type	Name	Inference/Disease	Calculation	Reference
Classic Indices	Normalized Difference Vegetation Index (NDVI)	Chlorophyll	$(R_{800}-R_{670})/(R_{800}+R_{670})$	Rouse et al. (1974) Tucker et al. (1981)
	Plant senescence Reflectance Index (PSRI)	Pigment content, Senescence	$(R_{680}-R_{500})/R_{750}$	Merzlyak et al. (1999)
	Carotenoid Reflectance Index (CAR1)	Carotenoids	$1/R_{510}-1/R_{550}$	Gitelson et al. (2002)
	Anthocyanin Reflectance Index (ARI)	Anthocyanins/Yellow rust (wheat)	$1/R_{510}-1/R_{700}$	Gitelson et al. (2001) Zheng et al. (2018)
	Photochemical Reflectance Index (PRI)	Photosynthesis, Carotenoids/Yellow rust (wheat)	$(R_{570}-R_{531})/(R_{570}+_{531})$	Gamon et al. (1992) Zheng et al. (2018)
	Normalized Difference Spectral Index (NDSI)	Leaf spot diseases (peanut)	$(R_{800}-R_{670})/(R_{800}+R_{670})$	Rouse et al. (1974) Chen et al. (2019)
Disease Specific	Cercospora Leaf Spot Index (CLS)	Cercospora leaf spot (sugar beet)	$(R_{698}-R_{570}/(R_{698}+R_{570})-R_{734}$	Mahlein et al. (2013)
	Sugar Beet Rust Index (SBRI)	Sugar beet rust (sugar beet)	$(R_{570}-R_{513})/(R_{570}+R_{513})+(1/2*R_{704})$	Mahlein et al. (2013)
	Powdery Mildew Index (PMI)	Powdery mildew (sugar beet)	$(R_{520}-R_{584})/(R_{520}+R_{584})+R_{724}$	Mahlein et al. (2013)
	Leaf Rust Disease Severity Index 1 (LRDSI_1)	Brown rust (wheat)	$6.9*(R_{603}/R_{455})-1.2$	Ashourloo et al. (2014)
	Leaf Rust Disease Severity Index 2 (LRDSI_2)	Brown rust (wheat)	$4.2*(R_{639}/R_{455})-3.8$	Ashourloo et al. (2014)
	Red Edge Disease Stress Index (REDSI)	Yellow rust (wheat)	$(705-665)*(R_{783}-R_{663})-(783-665)*(R_{705}-R_{663})2\times R_{665}$	Zheng et al. (2018)
	Lemon Myrtle-Myrtle Rust Index (LMMR)	Myrtle rust (myrtle)	$(R_{545}/R_{555})^{5/3}*R_{1505}/R_{2195}$	Heim et al. (2019)

R_i: indicates reflectance at waveband *i*.

1.4.1 Wheat disease detection - controlled conditions

The measuring environment is of high importance for the success of disease detection procedures. Most research tackling the detection of plant diseases with optical sensors is performed under controlled conditions in a laboratory. In this case, the measuring environment can be efficiently controlled by ensuring homogeneous light conditions, a constant room temperature and a proved measurement design, e.g. for measuring horizontal aligned plant leaves (Mahlein et al. 2012), or the preprocessing and normalization of data (Bohnenkamp et al. 2019b). Confounding natural weather conditions, such as rain and changing illumination conditions through clouds, or the heterogeneity of a crop stand can be excluded. Hyperspectral camera systems can be mounted to autonomous moving devices (e.g. a linear stage) that allow a defined movement speed of the sensor over the object to be measured (Fig. 4). The light sources can be mounted to this linear stage to ensure a homogeneous illumination during measurement. Controlled conditions allow to produce repeatable measurement conditions that make it possible to compare data from different measurement dates (Bohnenkamp et al. 2019b). Most of these works using HS imaging sensors for disease detection were performed in close-range imaging to investigate and characterize the pathogenesis (Mahlein et al. 2010; Mahlein et al. 2012; Kuska et al. 2015; Lowe et al. 2017; Zhu et al. 2017; Kong et al. 2018; Whetton et al. 2018a; Bohnenkamp et al. 2019b). Hyperspectral close-range imaging provides images with both, a high spectral and spatial resolution, suitable for a pixel wise investigation of diseased crop leaves (Mahlein et al. 2012; Mahlein 2016). Early host-pathogen interactions occur in the submillimeter range. Wahabzada et al. (2015) used a hyperspectral camera for disease detection at close range with a pixel size of 0.12 mm per pixel. The used setup was suitable for the detection of early host-pathogen-interaction responses (Wahabzada et al. 2015). Thus, only close range imaging has a spatial resolution sufficient for detecting these changes in early pathogenesis (Mahlein et al. 2012). Various host-pathogen-interactions on monocotyledonous and dicotyledonous plants have been investigated (Yuan et al. 2014; Leucker et al. 2016; Zhu et al. 2017; Kong et al. 2018; Whetton et al. 2018a; Yao et al. 2019). In cereals, experiments were mostly performed with wheat and barley. Several studies were performed with biotrophic fungi (Kuska et al. 2015; Wahabzada et al. 2015; Whetton et al. 2018a; Bohnenkamp et al. 2019b; Yao et al. 2019) but also investigations with necrotrophic fungi have been conducted (Iori et al. 2015; Wahabzada et al. 2015; Behmann et al. 2018b). A central part of investigations is the characterization of

the spectral dynamic of pathogenesis to link these findings with biochemical processes of the host-pathogen-interaction. The gain of knowledge is used to train models for an autonomous detection and identification of one present disease or mixed infections. The scope for investigations under controlled conditions can be the development of robust measuring protocols for phenotyping approaches for disease resistance of cultivars and antifungal compounds in the greenhouse or the development of detection routines for field approach. Therefore, the horizontal fixation of cereal plant leaves allows a detailed monitoring of the spectral leaf properties under disease pressure over time. These findings must be combined with data from high throughput facilities that gather additional information on plant disease appearance on different leaf levels and leaf geometries. A milestone out of these findings should be the development of data sets that include not just the quantification of directly measurable diseases on a certain leaf but also calculations and/or estimations for the disease occurrence on the whole plant. Detection models have to take into account that the degree of the disease cannot be represented in just one image from top view. Lower leaves are often covered by upper leaves. High throughput information of hundreds of diseased crop plants is needed to develop calculations for the specific true amount of the disease. This information is of essential importance to develop robust detection models for field approaches under environmental conditions.

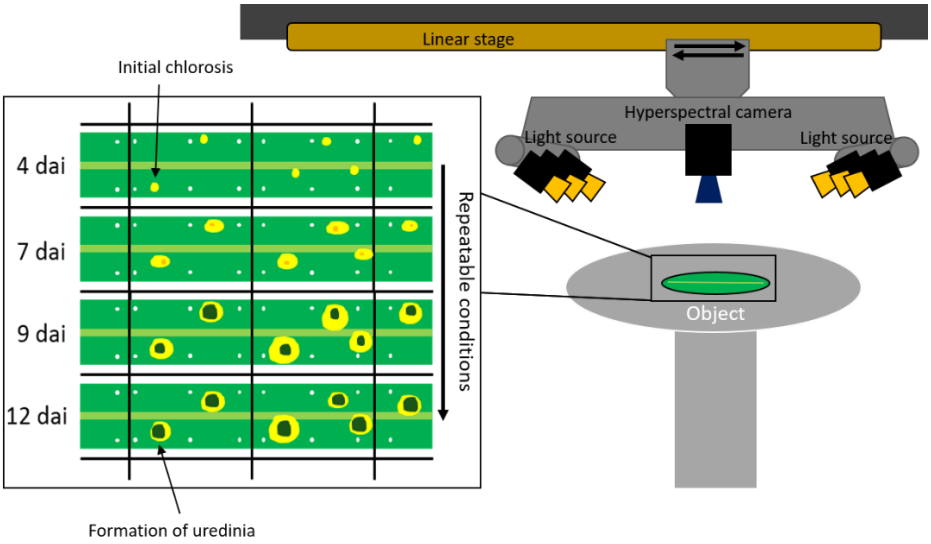

Fig. 4: Schematic overview of a hyperspectral line scanning measuring system for controlled conditions. Scheme shows linear stage with attached camera system (hyperspectral line scanner), defined light sources and the object to be measured (nadir distance to the camera 40 cm). A time series of brown rust (zoom) is displayed (from first symptoms to late stage symptoms and sporulation) to show how reproducible data is generated.

1.4.2 Wheat disease detection - field conditions

Optical measurements under field conditions are extraordinarily challenging (Bravo et al. 2003; West et al. 2003). A wheat crop stand is a geometric complex structure with several hundreds of tillers per square meter forming the canopy. The leaf architecture of crop plants can either be erectophile or planophile with the effect that an erectophile architecture allows views to the lower leaf levels (from nadir view) (Sandmeier et al. 1998). Wheat plants seem to be a mixture out of both types with an occurring secondary irradiance (light is reflected or transmitted) in between the crop stand that might brighten shadowed areas. The crop architecture and the leaf angle are important factors influencing the measurements of reflectance. The way of light through the crop canopy is a complex phenomenon. The wheat canopy is composed of many leaf layers of different altitudes with variability in leaf size, orientation, shape and coverage of the ground surface (Campbell 2002). Upper leaves cast shadows that mask lower leaves. The overall reflectance is a combination of leaf reflectance and shadowing. Compared to single-leaf-measurements under controlled conditions, the crop canopy reflectance tends to be lower due to shadowing. In a crop canopy, the relative decrease of the NIR is much lower than the visible light. This can be explained by the fact that 3-5 % of the visible light is reflected by the field canopy compared to 10 % of visible light in single-leaf-measurements from controlled conditions. 35 % of the NIR is reflected in the field while 50 % are reflected under controlled conditions (Campbell 2002). Fig. 5 shows a simplified schematic description of the way that light of different spectral regions takes through the crop canopy. Infrared radiation is transmitted through the upper leaves and reflected from lower leaves and retransmitted back through upper leaves. Reflection of NIR also happens when light that was transmitted through leaves, reaches the soil below the canopy and then is reflected back. The visible light consists of the red, green and blue range. Red and blue light is largely absorbed by the crop canopy for photosynthesis and green light is largely reflected through the presence of chlorophyll (plants appear green) (Campbell 2002).

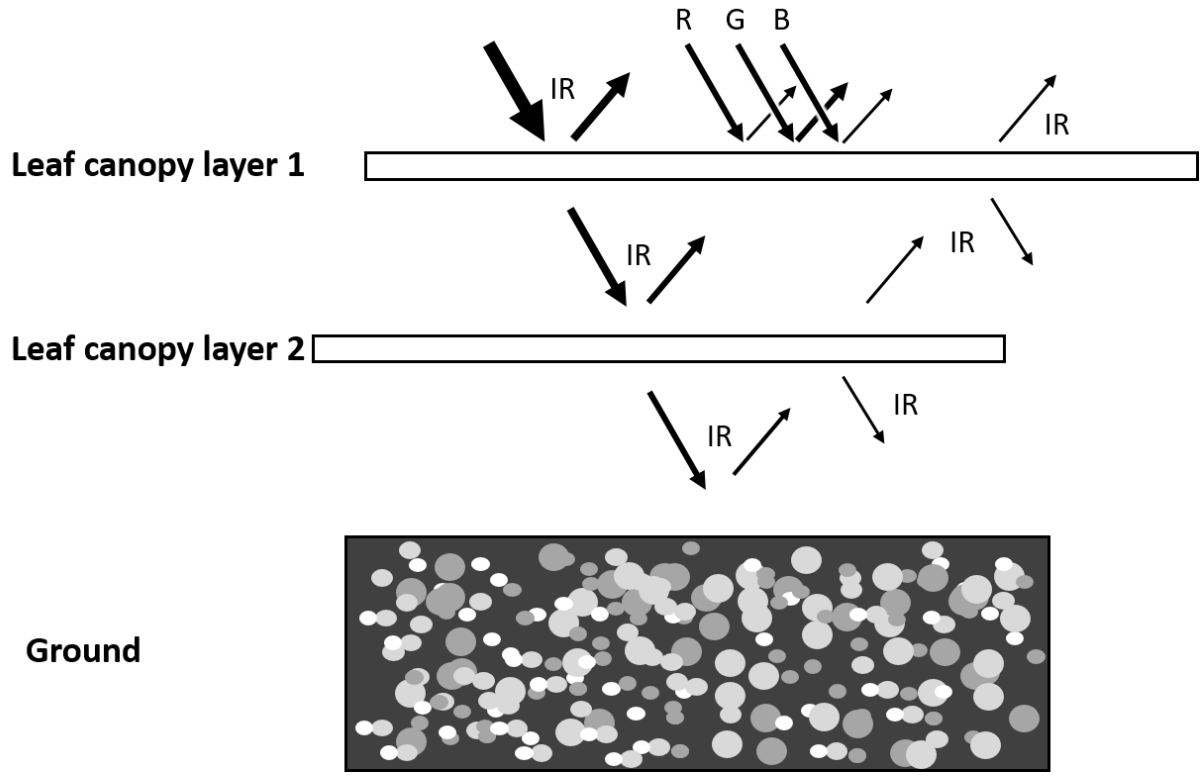

Fig. 5: Simplified cross sectional view of the way of light through a crop canopy. Light can be reflected, transmitted or absorbed. The measured signal is the result of the complex interaction of light from different spectral regions of the electromagnetic spectrum with the crop canopy layers and the soil. IR: infra-red light, R: red light, G: green light, B: blue light (Adapted from Campbell (2002)).

Additional to these highly complex tasks, another factor that is highly specific for a single crop has to be taken into account - the leaf geometry. The leaf geometry has a significant distortion effect on the spectrum. The composition of shadowed and illuminated canopy components is highly dependent on the leaf orientation and structural properties of the plant species, phenology and health status. Regarding analysis of field data, Jay et al. (2016) showed that the disturbing effect of changing weather conditions could be significantly removed, but the negative effect of leaf geometry remains in the data. The PROCOSINE model might be an approach to handle these effects (Jay et al. 2016).

Additionally, infection biology and epidemiology of a disease have a big impact on its detectability. The inoculum of many pathogens is soil borne or located in crop debris on the ground. Diseases often spread from the bottom leaves to the upper leaves through wind or most likely through the kinetic energy of rain droplets (STB). Such a disease will appear and manifest initially on lower leaf levels long before the upper leaves or the flag leaf of wheat can be colonized. The control thresholds for fungicide applications (counting disease incidence)

for STB depend on the wheat growth stage. In BBCH 32-37 it is 30 % disease incidence (on the upper four leaves) while in 39-61 it is 10 % (Miedaner 2018). A detection device for practical approach should be able to objectively determine these specific control thresholds for each disease. Septoria tritici blotch has an additionally long latency phase where no symptoms are visible (biotrophic phase). This hampers a profound measurement by nadir on top of a crop canopy as the upper leaves just don't show disease symptoms. To gather the infection status of a crop stand infected by a pathogen that initially infects the lower leaf levels, a sensor system ought to be moved through the crop stand to cover each leaf level. Other diseases like tan spot have also soil borne inoculum and can have a particularly rapid disease development when it comes to favorable conditions (Strelkov and Lamari 2003). The latency phase usually takes only a few days and disease monitoring might occur late when symptoms already became visible on the leaf surface. Exclusively wind-borne pathogens initially infect the upper leaves where the spores land on and germinate. This favors the detection of foliar rust diseases or powdery mildews. Especially in early phase of the vegetation period, YR shows an initially patchy distribution in the field where chlorotic spots (as first symptoms) can become visible on all present leaves. Brown rust is a typical disease of the later/warmer season and might initially become visible as chlorotic spots on all present leaves. Powdery mildew can occur during the whole season on stems and leaves. Several authors have shown that a general detection of crop stress in the field is possible. Likewise, the detection of more specific biotic crop stress caused by plant diseases is possible (West et al. 2003; Whetton et al. 2018b; Yu et al. 2018; Zheng et al. 2018a). Most of these works use multispectral imaging or hyperspectral non-imaging sensors, but only a few of them used a hyperspectral imaging measurement system. As there is a huge variation of hyperspectral cameras on the market, hyperspectral measurements in the field demand high quality equipment and measurement platforms suitable for their purpose (Mahlein et al. 2018; Thomas et al. 2018).

1.5 Effect of weather conditions on hyperspectral field measurements

The image quality of field data in general is influenced by various factors. Environmental conditions are not controllable in the field. Disturbing weather conditions such as wind (blurred images) and rain or dew causing leaf wetness (diffuse backscattering of light) can easily impair spectral images that are obtained in the field. Field measurements should be performed on calm days after leaf drying. The most relevant factor is illumination. Optical measurements are depending on a light source. This can either be the sun as a natural light

source or artificial light on a measurement platform. When the sun is the natural light source, changing illumination conditions over time due to clouds or the diurnal cycle might lead to impractical data. If a hyperspectral camera is used, this could lead to heterogeneous illumination conditions within one image due to the time-delayed image acquisition depending on the spatial and spectral resolution. The spectral information of different images cannot be compared one another (Bravo et al. 2003; West et al. 2003; Roosjen et al. 2016) and one result could be misclassifications (Bohnenkamp et al. 2019a). Figure 6 shows the effect of changing illumination conditions on the image quality during image acquisition with a line scanning camera. In various works, the scientists preferred measuring conditions with a dense cloud coverage under the assumption that the cloud coverage is homogeneous and light conditions are constant (West et al. 2003; Whetton et al. 2018b). Cloudy conditions have an advantage compared to a cloudless sky: the sunlight will be scattered. This leads to the fact that scattered light results in a more homogeneous illumination of the crop canopy with less to no disturbing shadow casted by the measuring device or the upper plant organs. Nevertheless, a cloudy sky can be less homogeneous as it appears. The cloud coverage could be inhomogeneous with locations of less or more dense clouds that are in motion of the wind and heterogeneities in image brightness can change from minute to minute (Mahlein et al. 2018). Illumination changes could occur during single measurements or the measurement day without being noticed. The amount of change is easier to measure under direct light conditions (with no clouds). But here, a strong cast of shadows in the crop canopy could lead to inhomogeneous illumination conditions in between the different leaf levels (Yu et al. 2018). Due to the plant architecture, the flag leaf (F) has the highest sun exposure. The lower leaf levels (F-1, F-2, F-3…) are often covered by the upper leaves. Either way, in the field it is of high importance to be able to perform measurements that are robust against variation in illumination intensity (Wendel and Underwood 2017). The illumination intensity has to be continuously observed. In combination with reflectance standards, that reflect a defined amount of the sunlight, the data can be processed and normalized. By performing a data normalization, the field data can be compared even on different measurement days. A typical standard for field measurements reflects 50 % of the incoming sunlight and can be recorded in each hyperspectral image of the crop canopy (Bohnenkamp et al. 2019a). Interpolation approaches might fail through a lack of continuous illumination observations (Suomalainen et al. 2014; Roosjen et al. 2016). Radiation transfer models have been described that might be

suitable to address these issues (Jay et al. 2016). Especially at close scale imaging, the leaf geometry has a big impact on the accuracy of radiative transfer and thus leads to significant disturbing effects for illumination normalization. Jay et al. (2016) considered the spectral reflectance of the leaf surface in combination with the local leaf orientation. The used model allows a robust sub-millimeter retrieval of foliar hyperspectral reflectance and shows the potential for future works combining close-range imaging considering illumination conditions and the local leaf geometry (Jay et al. 2016).

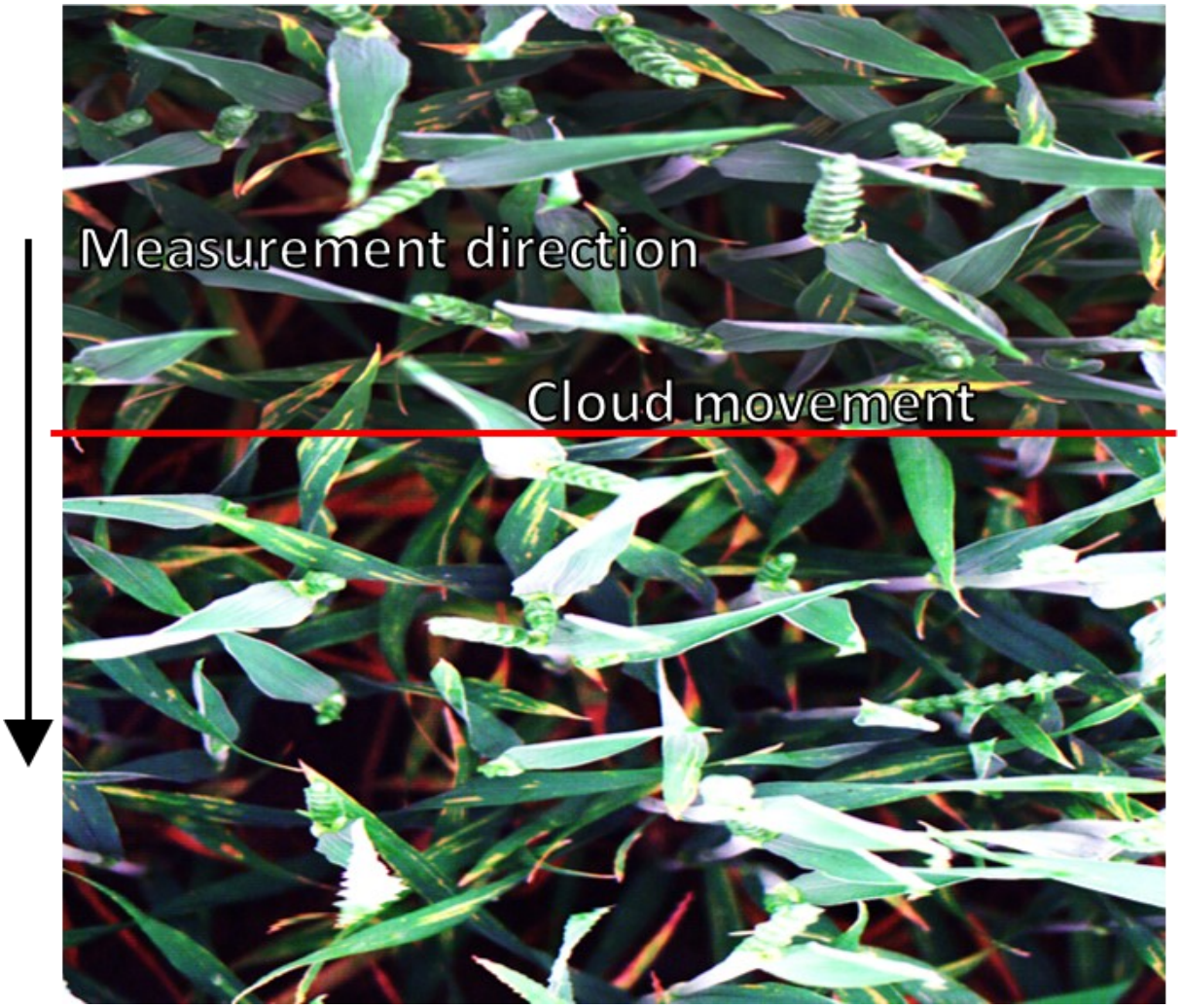

Fig. 6: Effect of changing illumination conditions on the image quality during a hyperspectral image acquisition. The measuring principle is based on a line scanning camera. The image acquisition took about 30 seconds. The used exposure time in the camera settings was adapted to the lower illumination conditions. When the illumination increases, the brighter image parts are overexposed to sunlight. A manual or automatic down-regulation of the exposure time during image acquisition was not possible. Overexposed image parts are the upper plant organs (flag leaf and ears).

1.6 Effect of biological heterogeneity of wheat on hyperspectral field measurements

The biological heterogeneity and the correct dealing with it, is one core determinant for the successful analysis and interpretation of field data. Biological heterogeneity can be defined as the entire dynamic of the phenotypic appearance of a crop stand and single crop plants in the field. With a deeper look into a wheat canopy, it becomes obvious that the wheat plant consists of different plant organs that are located on different altitude levels. A wheat plant has a stem, different leaves with each younger leaf located one leaf level above the older one, and ears (depending on the growth stage). The iteration of different crop growth stages also has an impact on the electromagnetic spectrum (Zheng et al. 2018a). If hyperspectral measurements should be performed in the field, this complex architecture of a wheat plant has to be considered. Different leaf altitudes lead to inhomogeneous illumination conditions on the different leaf levels (Mahlein et al. 2018). Inhomogeneous illumination conditions have to be considered if the spectral properties of different leaves should be compared. A hyperspectral imager is often not capable of detecting the true status of disease incidence on the lower leaves (Whetton et al. 2018b). Additionally, the upper leaves can cast shadow onto lower leaves. Similar to the changing illumination due to weather conditions, the inhomogeneous illumination of a crop stand has to be taken into account for later calculations and corrections. The canopy color changes from week to week due to the plant development in environmental conditions influenced by natural growth, light, age and maturity (senescence), nutrient availability and not least the cultivar color itself. This dynamic of the optical appearance makes it complex to compare spectral properties from one measuring day to another. Additionally, the optical properties can be influenced by symptoms and a premature senescence caused by abiotic and biotic factors. Chlorotic spots, stripes and necrosis can be caused by nutrient deficiencies or plant diseases. These symptoms appear on different leaf levels in different intensities. Typically, leaves of different ages show a diverse susceptibility to stress. When it comes to favorable conditions for plant disease infections, wheat plants exhibit different disease incidences on different leaf levels in combination with mixed infections. Because this heterogeneity is captured in one single hyperspectral image (Fig. 7), these data sets consist of a high complexity for further analysis. From nadir view, the lower leaves show higher YR infestation than the upper leaves, but this status can hardly be represented in the images. Due to the lower reflectance intensities of the older leaves the

detectability of the disease could vanish. This effect might be strengthened through color changes of the leaves resulting from maturity.

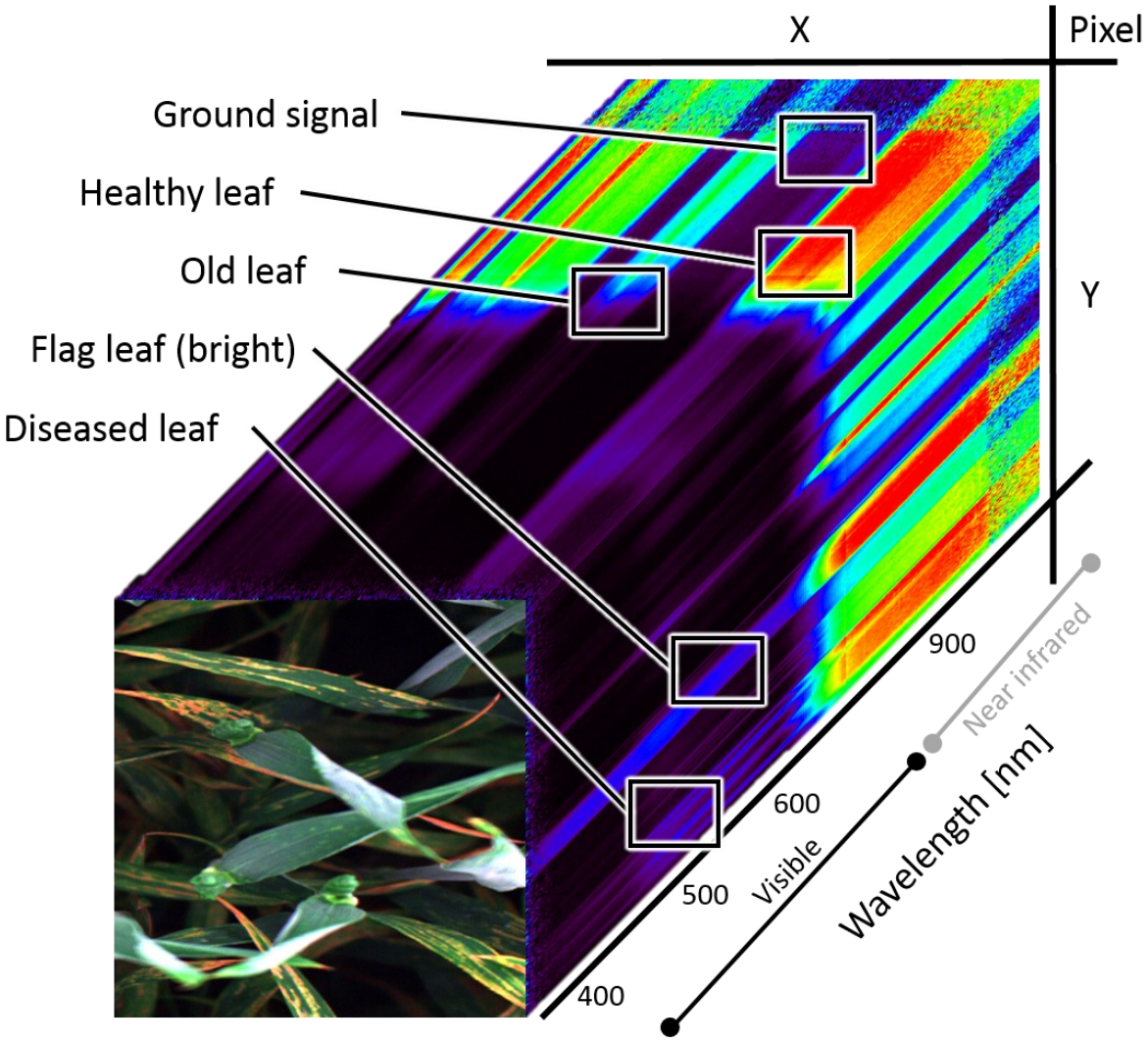

Fig. 7: Data cube of a hyperspectral image taken in the field. The data cube illustrates the biological heterogeneity that is present in each hyperspectral field image. The spectral information is influenced by ground signals, different leaf altitude signals and disease signals on different leaf altitudes.

1.7 Effect of the measurement scale on hyperspectral in-field wheat disease detection

To define a measuring setup, it is of high importance to be aware of what needs to be measured. Choosing the right sensor in combination with the right measurement scale is the key requirement for successful field measurement platforms. Possible targets could be an early detection and identification of wheat diseases, a quantification of the disease symptoms or a quantification of disease incidence in the field. UAV measurements in a height of 50 m to the crop stand in combination with a low spatial resolution hyperspectral camera will not be sufficient to perform an early detection of single initial chlorotic spots caused by YR compared to a measuring device that is moved closely above the leaf canopy in combination with a high spatial resolution optics and a submillimeter pixel size. The measurement purpose always determines the measurement scale. Various works under laboratory conditions showed that a pixel wise analysis of disease symptoms close-range imaging is possible (Kuska et al. 2015; Wahabzada et al. 2015; Leucker et al. 2016; Bohnenkamp et al. 2019b). The most precise measurements can be performed under laboratory conditions through the exclusion of environmental factors. The measurements are often performed on close-scale (measuring distance from the object of interest to the optics: several millimeters – 60 cm) and can either be addressed to answer basic research issues or the gathering of huge data sets in high throughput devices (high throughput phenotyping). Disease detection of foliar wheat diseases in the field so far is mostly performed with ground-based vehicles (Bravo et al. 2003; West et al. 2003; Moshou et al. 2004; Whetton et al. 2018b; Yu et al. 2018; Azadbakht et al. 2019). Various works focused on the detection of diseases using VI's in combination with a non-imaging spectrometer. Whetton et al. (2018b) used a hyperspectral imaging camera on a ground-based vehicle for the detection of YR and fusarium head blight. A ground-based detection is often performed in a distance of 20-60 cm over the crop canopy. This distance, in combination with a camera that provides a suitable spatial resolution, can image a disease symptom by several pixels with a submillimeter size. In this case diseased pixels can be differentiated from healthy plant pixels. In addition to that this separation enables a quantification of diseased pixels possible by simply counting the pixels. This allows for a disease quantification. Non-imaging sensors average the spectral information over a certain area and do not provide a spatial distribution of pixel information in one image. Hence, a direct quantification of the disease is not possible and has to be done through the calculation of gradients or regressions out of the averaged spectral reflectance.

UAV drones equipped with multispectral cameras are frequently used to acquire canopy data from a larger scale. Measurements are often performed in 20-100 m height above the wheat canopy (Bohnenkamp et al. 2019a). With a UAV, a larger area can be monitored compared to ground-based vehicles or rating. One disadvantage of the measuring distance is the resulting lower spatial resolution. The higher the altitude the bigger the ground pixels of the image. This means that the same camera that is used on a UAV (pixel size several centimeters) or a satellite (pixel size several meters) can have a submillimeter pixel size at ground canopy scale. Figure 8 shows the effect of the measuring distance (UAV and ground-based measurements) on the pixel size. This effect means a loss of information and a higher number of mixed signals due to transition areas from diseased to healthy, leaf to plant and leaf to soil pixels. Contrary, Zhang et al. (2019) proved that hyperspectral cameras can be used for sufficient disease detection of YR on the UAV-scale combining the advantages of spectral and spatial information of hyperspectral imaging. In general, the issue of the scale is always the compromise between the desired information content (size of one pixel) and the throughput/flexibility of the measuring platform. This fact can be upscaled to plane and satellite measurements. A UAV drone in 20 m height is capable of detecting early patches of YR. But a ground-based system with the same camera might be able to detect first changes several days earlier and this could be the time that is necessary to initiate an effective plant protection measure. Choosing the right measurement scale is always a compromise between a high throughput (UAV scale) and a high resolution (ground canopy scale). Each scale makes different demands to data processing and analysis but they have one thing in common: for future commercialization of new sensory systems in agriculture, data analysis pipelines have to automatically analyze the data and to derive a measure online in the field where it is operating.

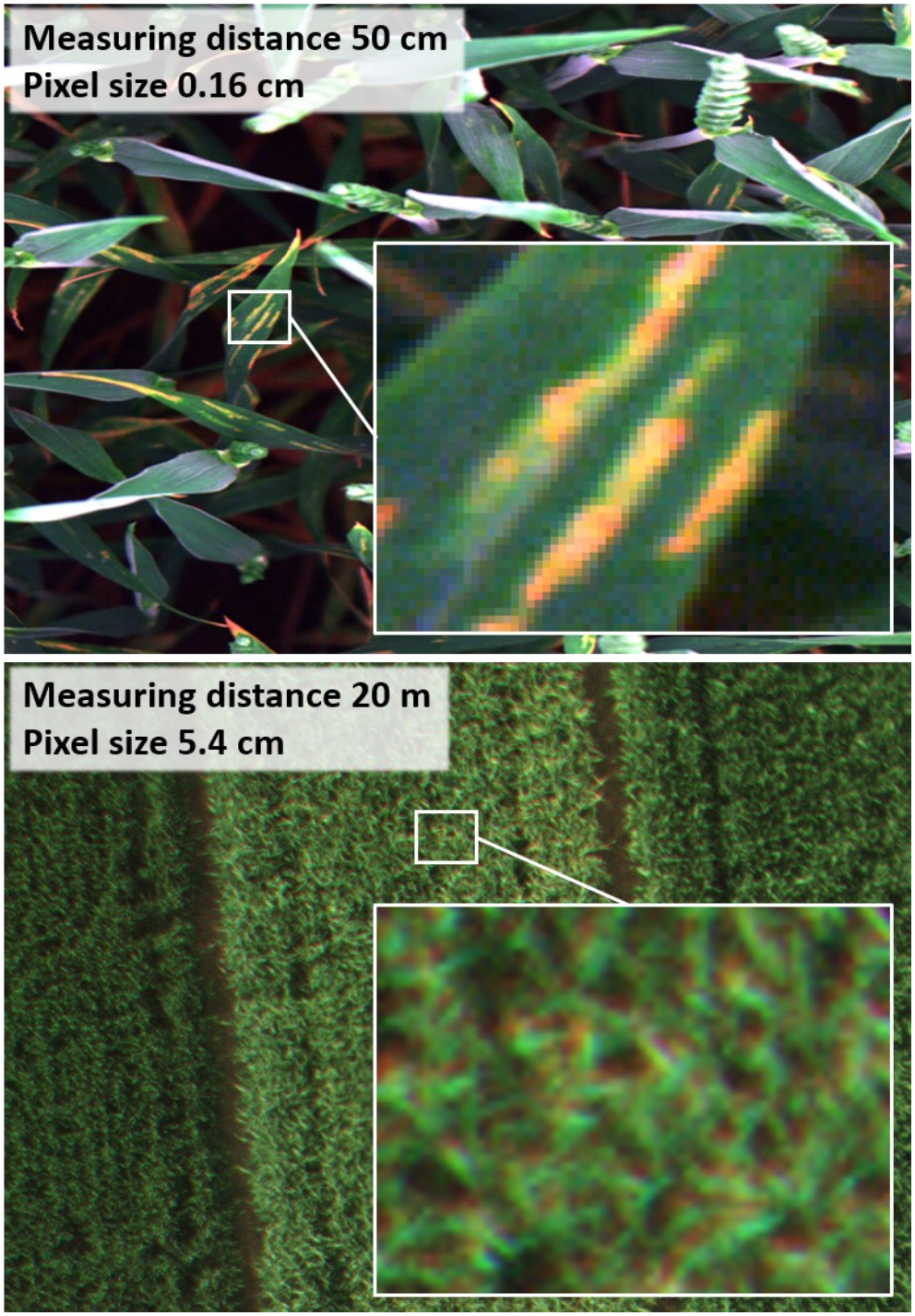

Fig. 8: Comparison of the calculated theoretical pixel size on the ground canopy (top image, 50 cm measuring distance) and the UAV scale (bottom image, 20 m measuring distance). At the ground canopy scale (top zoom image) one pixel has the size of 0.16 cm in the displayed image. One YR symptom can be represented by many pixels. At UAV scale (bottom zoom image) one pixel has the size of 5.4 cm. The spectral information of either 0.16 cm or 5.4 cm is averaged in one pixel. At UAV scale, a higher throughput is possible but a loss of information occurs due to decreased spatial resolution.

1.8 Artificial intelligence as a tool for data analysis

Much as hyperspectral sensors are promising for the detection of diseases in agricultural crops, they are very complex when it comes to the analysis and interpretation of their generated data. Data from hyperspectral images are big in size (up to several gigabytes). The analysis is challenging as a small proportion of relevant information from the hyperspectral signal has to be extracted (Behmann et al. 2015). To enable reliable results under challenging environmental conditions, such as sunlight and/or cloudy weather, complex algorithms are needed (Wendel and Underwood 2017). Machine learning (ML) has emerged in the era of big data technologies (Liakos et al. 2018). Usually, ML involves a learning process with the object to learn from training data to perform a certain task such as the classification of plant diseases in an image. An individual example is described by a set of attributes, also known as features or variables. ML tasks can be classified in supervised and unsupervised learning models. In supervised models, training data is provided as input data to the algorithm (Liakos et al. 2018). The training data is labeled but can be error prone due to the manual annotation of a human being (Bohnenkamp et al. 2019a). Unsupervised models do not rely on labeled training data while the algorithm works unsupervised based on the data distribution with the goal of discovering hidden patterns (Liakos et al. 2018). Machine learning approaches are able to cope with hundreds of wavebands of hyperspectral sensors, whereas for multispectral sensors VI's are adequate. ML in combination with hyperspectral cameras can be used for the detection, identification and quantification of plant diseases. They learn a model out of the data itself with the ability to unveil hidden features of the data (Behmann et al. 2015; Lowe et al. 2017; Mahlein et al. 2018; Bohnenkamp et al. 2019a). The combination of hyperspectral imaging data with analysis approaches from machine learning offers high potentials for a robust detection of plant diseases (Golhani et al. 2018).

Representative supervised classification algorithms are the spectral angle mapper (SAM) and the support vector machine (SVM) (Fig. 9). These algorithms rely on the labeling of training data for model generation (Bohnenkamp et al. 2019a). The SAM calculates the spectral resemblance (a spectral angle) between a reference spectrum and the spectrum to be classified. The SAM algorithm uses the mean spectra of the input classes as reference spectra (Kruse et al. 1993). The SVM creates a decision boundary between classes for classification. The efficiency results in a parametrization by support vectors (Cortes and Vapnik 1995). Compared to the SAM the SVM does not use the mean spectra of a certain class as input data.

Instead, it can be trained on the whole data set and can use the spectrum of each pixel as input data. The SAM and the SVM were successfully used for the detection of YR of wheat even under field conditions (Bohnenkamp et al. 2019a). The scientists were able to reach an accuracy of > 90 % for YR detection both on the ground canopy and the UAV scale. Huang et al. (2019) used SVM to detect powdery mildew in winter wheat. Whetton et al. (2018b) used a PLS regression with a leave-one-out cross-validation for the detection of YR and fusarium head blight in the field. Azadbakht et al. (2019) showed a detection with high accuracy of wheat brown rust hyperspectral imaging at different leaf area index levels with different machine learning techniques using support vector regression, boosted regression trees, random forest regression and Gaussian process regression.

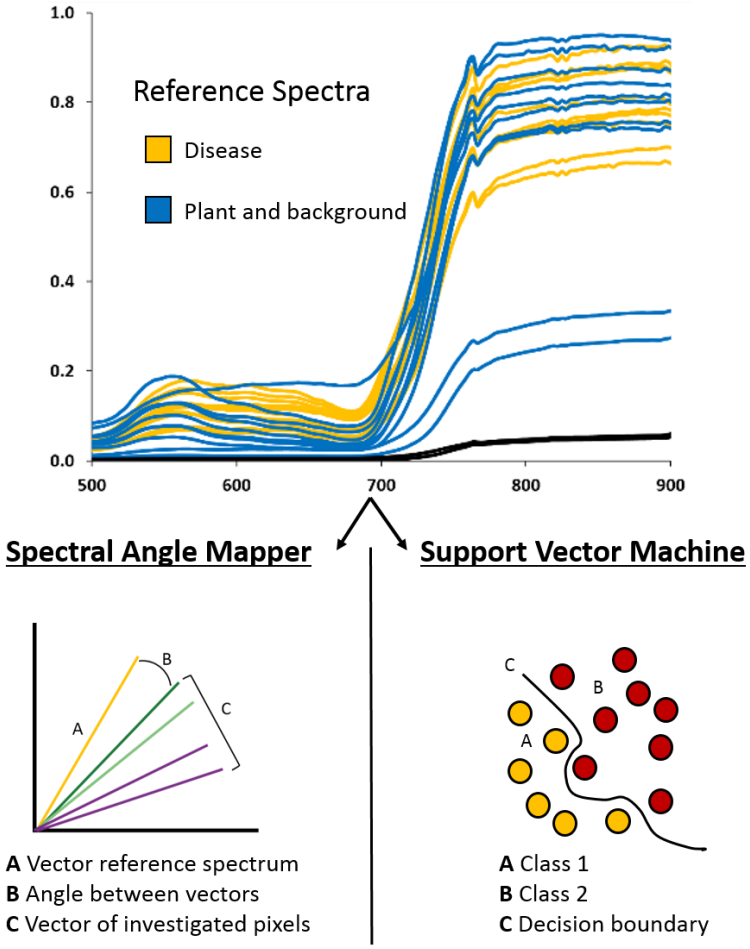

Fig. 9: Schematic comparison of the two different supervised classification algorithms spectral angle mapper (SAM) and support vector machine (SVM). Different ways of handling reference spectra. Classification through the calculation of the angle between vectors of spectra (SAM) and classification by creating a decision boundary using supporting vectors (SVM). The handling of reference data determines the suitability of an algorithm for a certain task.

A powerful tool to improve the detectability of plant diseases in hyperspectral images is the use of neural networks (NN) from deep learning that are based on and adapted from the human nervous system (Golhani et al. 2018). Like the vast network of neurons in the human brain, NNs are interconnected complex networks of nodes. Different to predefined features from ML, deep learning (DL) models determine more abstract and more informative data representation (Mahlein et al. 2018). DL models do not depend on labelled training data and are self-learning approaches. Major types of NNs are Single-Layer Perceptron (SLP), Multi-Layer Perceptron (MLP), Radial-Basis Function (RBF) networks, Kohonen's Self-Organising Map (SOM) networks, Probabilistic Neural Network (PNN) and Convolutional Neural Network (CNN). Due to the unique capabilities such as learning, generalization and imaging, CNNs show high potentials to improve the reliable diagnosis of plant diseases and have a higher degree of diagnosability compared to other ML techniques (Golhani et al. 2018). CNNs as part of deep learning constantly achieve new accuracies in image recognition and segmentation (Chen et al. 2018). NNs were used in various applications for disease detection. (Moshou et al. 2004) used MLP and SOM for the automatic detection of YR in wheat with a detection accuracy of 99 %. (Zhang et al. 2019) used a deep convolutional neural network approach to detect YR in hyperspectral UAV images with a detection accuracy of 80-90 %. The constantly good accuracy over different growth stages during vegetation period was particularly interesting. In the future, a fundamental goal for disease detection techniques will be the early detection of diseases. In the best case the combination of a sensor and ML/DL algorithms should be capable to detect the disease before it becomes visible for the human eye. Future plant disease detection pipelines will include recent analysis methods from machine and deep learning to reach high detection accuracies even at early growth stages and under constantly challenging environmental conditions.

1.9 Objectives of the study

This study aimed to test the potential of hyperspectral sensors for the in-field detection of foliar diseases of wheat with regard to a site-specific detection and disease mapping.

The first goal (I) was to generate characteristic spectral signatures from different diseases under laboratory conditions with hyperspectral sensors by monitoring the spectral dynamic of tan spot, septoria tritici blotch, brown rust, YR and powdery mildew during disease development. The spectral dynamic has been monitored, and spectral changes should be explained with biochemical processes that happen during host pathogen interaction for better understanding of how to extract the spectral fingerprint of a disease out of the mixed signal of a plant leaf. This interaction was investigated simultaneously using different microscopic methods.

(II) Once this information was generated, recent data analysis methods were performed on this data. Different approaches from machine learning were used to detect, identify and quantify the different foliar diseases from fixed horizontally aligned plant leaves and out of plant leaves with natural leaf angles.

(III) To ensure a transduction of HI to the field, a ground-based vehicle was conceptualized and developed for canopy field measurements of winter wheat. Additionally, a data processing pipeline was developed to produce data that are comparable both over different images and different measurement days. High attention was given to ensure a data-based scale and knowledge transfer.

(IV) The insights from (I, II, III) were used to additionally establish a UAV based measuring system to simultaneously monitor the wheat canopy performance on the UAV scale from 20-100 m with a suitable analysis pipeline for UAV data.

(V) The suitability of hyperspectral sensors for an in-field detection of plant diseases should be assessed through the identification of disease specific wavebands to give an evaluation and recommendation on the future potential for the field approach of hyperspectral and multispectral sensors for disease detection.

2 Hyperspectral library of foliar diseases of wheat

This work has been submitted to the Journal “Phytopathology” of the American Phytopathological Society. Submission date: 12-Sep-2019. The current status is “Major Revision”. Involved authors: David Bohnenkamp, Jan Behmann, Ulrike Steiner, Anne-Katrin Mahlein.

David Bohnenkamp performed the experiments (100%), DB analyzed the data and wrote the paper (80%).

2.1 Abstract

This work established a hyperspectral library of important foliar diseases of wheat in time series to detect spectral changes from infection to symptom appearance induced by different pathogens. The data were generated under controlled conditions at the leaf-scale. The transition from healthy to diseased leaf tissue was assessed, spectral shifts were identified and used in combination with histological investigations to define developmental stages in the pathogenesis for each disease. The spectral signatures of each plant disease that are indicative of a certain developmental stage during pathogenesis - defined as Turning points - were combined into a spectral library. A spectral angle mapper algorithm was used to test the potential of this library for the detection and quantification of foliar diseases in hyperspectral images. The classifier provided reliable results for the biotrophic fungi. Classification of necrotrophic fungi was less reliable due to the development of unspecific necrosis. But even the temporal coincidence of misclassifications indicated characteristics for identification of necrotrophic diseases. The potential of applying spectral analysis methods, in combination with a spectral library for the detection and identification of plant diseases is shown. Further evaluation and development of these algorithms might lead to a robust detection and identification of plant diseases at different developmental stages and could promote the development of site-specific management techniques of plant diseases under field conditions.

2.2 Introduction

Precision crop protection will make use of sophisticated sensors that help to enable a site-specific plant disease management at the right time and the right spot for application to avoid dispensable fungicide use (West et al. 2003; Mahlein et al. 2018). It is important to develop technical systems that fulfil these demands that are expected from modern precision agriculture (Bock et al. 2010; Mahlein et al. 2012b). Therefore, reliable identification of disease

symptoms and determination of disease incidence in the field are necessary. Hyperspectral cameras are one promising technique for field applications (Hillnhütter et al. 2011). These cameras are able to detect and identify structural and physiological changes that are caused by plant diseases, in and on the leaf surface because structural changes lead to characteristic shifts of the leaf reflectance spectrum. By measuring the reflected light, hyperspectral cameras are able to detect these changes in the electromagnetic spectrum from 400–2500 nm (Mahlein 2016).

Hyperspectral measurements in the field are particularly challenging (Bravo et al. 2003; West et al. 2003), because measuring systems have to combat disturbing and inhomogeneous weather conditions such as sunlight and wind (Bravo et al. 2003; Bravo et al. 2004). To introduce hyperspectral imaging technology into practical use in agriculture, basic knowledge, generated under controlled conditions, is necessary (Thomas et al. 2017). Various research has focused on the field detection of the biotrophic rust diseases of wheat, such as yellow rust (Bravo et al. 2003; Whetton et al. 2018), brown rust (Ashourloo et al. 2014) and powdery mildew (Cao et al. 2015).

In the field, different developmental stages of a disease can occur coincidentally. Plant diseases lead to specific symptom types with different size, shape and appearance on the host. While some fungi produce masses of fungal structures and spores on the leaf surface, for instance biotrophic fungi, the spectral signal of the leaf is considerably determined by features of these structures. Typical features might be the pigmentation of spores or a dense mycelium (Wahabzada et al. 2015). The symptoms of necrotrophic fungi are mainly characterized by the appearance of necrotic leaf area. Spore production is often less obvious compared to biotrophic fungi. The crucial point is the detection of spectral patterns that are individual to one certain disease, even if the symptoms are similar. To ensure this determination with hyperspectral sensors, the host-pathogen interaction has to be investigated in detail.

In this work, diseases causing necrosis are represented by two important pathogens of wheat. *Drechslera tritici-repentis* (Died.) Shoemaker is the cause of tan spot (DTR). *D. tritici-repentis* grows comparatively fast and is a necrotrophic ascomycete that produces a toxin leading to typical tan spots giving its name. Further symptom development can result in chlorosis or necrosis, or both depending on the race of the pathogen and wheat cultivar (Thomas and Bockus 1987). *Zymoseptoria tritici* (Desm.) Quaedvliet & Crous causes *Septoria* tritici blotch

(STB). The ascomycete has a biotrophic and a necrotrophic phase. The biotrophic phase is innocuous for the plant and is initially asymptomatic but necrotrophic phase leads to collapse of cells and initial small chlorotic spots resulting in necrotic lesions that can encompass entire leaves. Pycnidia are formed in the substomatal cavities of mature necrotic lesions (Steinberg 2015).The biotrophic diseases become apparent by the intense production of fungal structures on the leaf surface and are represented by three different pathogens. *Puccinia triticina* Eriks. is the fungal agent of brown rust (BR). BR shows small chlorotic spots as initial symptoms about 5 days after infection. During pathogenesis chlorotic spots increase and develop uredinia in their centre, bearing urediniospores (Bolton et al. 2008). *Puccinia striiformis* f. sp. *tritici* causes yellow rust on wheat (YR). First symptoms are tiny chlorotic spots that can occur already 6 to 8 days after infection. Copious production of urediniospores in uredinia appears about two weeks after infection on susceptible cultivars (Chen et al. 2014).*Blumeria graminis* f. sp. t*ritici* (DC.) Speer (*Bgt*) is the causal agent of wheat powdery mildew (PM). First symptoms occur 4 days after infection when tiny white spots become visible(Te Beest et al. 2008).

Aim of this study was to build up a spectral library for five different foliar diseases of wheat from infection to symptom development. Controlled conditions were chosen to establish a data set that shows the potential of a spectral library for disease detection which can be transferred across scales. Susceptible cultivars and one field isolate of each pathogen were used. Cultural practices excluded the influence of other pests, diseases, or nutrient deficiencies. The spectral library then was tested as training data in algorithms for autonomous disease detection and quantification. (i) Hyperspectral time series measurements were performed to observe the spectral changes of infected wheat leaves during pathogenesis. (ii) Simultaneous investigations of infected plant tissue with microscopy were used to interpret spectral changes during time series in accordance to the pathogenesis. (iii) Findings of hyperspectral measurements and histological investigations were utilized to define four spectral Turning points for each disease. These Turning points represent spectral signatures of a plant disease that is indicative of a developmental stage during pathogenesis. The definition of Turning points shall favor the time-independent and simultaneous determination of disease stages resulting from the occurrence of different infection incidents in the field. The outcome of this work show for the first time a detailed and comparative characterization of the spectral disease dynamics of wheat foliar diseases. These findings are

merged in a hyperspectral library as a spectral compendium for wheat disease detection, identification and quantification.

2.3 Materials and methods

Plant cultivation

Spring wheat plants (*Triticum aestivum*), cv. Taifun and cv. Chamsin (KWS SAAT SE, Einbeck, Germany) were grown in plastic pots of 13 cm diameter and 11.5 cm height in commercial substrate ED73 (Balster Erdenwerk GmbH, Sinntal-Altengronau, Germany) in a greenhouse under controlled conditions at 22/20°C day/night temperature, 60 ± 10% RH and a photoperiod of 16h per day. The plants were watered as necessary. After reaching BBCH growth stage 30 (sprouting) (Meier et al. 2001) plants were inoculated. According to Bundessortenliste (2018) cv. Taifun has a susceptibility of 8 for brown rust, 6 for yellow rust and 5 for powdery mildew. Chamsin shows a susceptibility of 6 for both DTR and STB (Bundessortenliste, BSA, 2018).

Pathogen cultivation

Experiments were performed with *D. tritici-repentis* (causal agent of tan spot, DTR), *Z. tritici* (causal agent of s*eptoria* leaf blotch, STB)*, P. triticina* (causal agent of brown rust, BR)*, P. striiformis* (causal agent of yellow rust, YR)*,* and *B. graminis* f. sp. *tritici* (causal agent of powdery mildew of wheat, PM). A spot and chlorosis inducing isolate of *Drechslera tritici-repentis* was used. The pathogen was cultured on oatmeal medium and stored at 18°C and a photoperiod of 12h. *Z. tritici* was isolated from a field in Rinkerode (Drensteinfurt, North Rhine-Westphalia, Germany). The hemi-biotrophic pathogen was cultivated on ISP2 medium (International Streptomyces Project Medium 2) and stored at 18°C and a day/night rhythm of 12/12h. *Puccinia triticina* was isolated from a trial field in Bonn (Germany). *P. triticina* was cultivated on wheat of cv. Taifun in the greenhouse conditions outlined above. A field isolate of *Puccinia striiformis* was used. It was cultured on wheat of cv. Catargo in a Panasonic climate cabinet (Panasonic Corporation, Kadoma, Japan) at 17/13°C day/night temperature, 70% RH and a photoperiod of 16h per day. Plant leaves were moistened using a spray flask daily. *Blumeria graminis* f. sp. *tritici* was isolated from a trial field in Bonn (Germany). *B. graminis* is an obligate biotrophic ascomycete and was cultured on wheat of cv. Taifun in a separate chamber in the greenhouse under conditions as per description.

Inoculum preparation and incubation

D. tritici-repentis was inoculated on wheat plants cv. Chamsin with a spore suspension in 0.01% Tween-20-water (2 x 10^4 conidia/ml) and incubated for with 24h without light followed by 24h with diffuse light in 100% RH in the greenhouse.

Z. tritici was inoculated on wheat plants cv. Chamsin with a spore suspension in 0.01% Tween-20-water (2,5 x 10^6 conidia/ml) and incubated for with 48h without light followed by 48h with diffuse light in 100% RH in the greenhouse. After incubation the plants were transferred into a separate greenhouse chamber with 18/16°C day/night temperature, 60 ± 10% RH and a photoperiod of 16h per day. During the following days, plants were misted from above once per hour for 5 secs by using a nebulizer nozzle at the finish of a watering system.

P. triticina was inoculated on wheat plants cv. Taifun with spore suspension in Tween-20-water (8 x 10^4 conidia/ml) and incubated for with 48h in diffuse light at 100% RH in the greenhouse.

P. striiformis urediniospores suspended in 3M™ Novec™ 7100 mineral oil (IoLiTec-Ionic Liquids Technologies GmbH, Heilbronn, Germany), were applied on wheat plants cv. Taifun by using an air brush. The plants were incubated in a climate cabinet for 24h, 100% RH and 10°C without light. After incubation conditions were set back to 17/13°C day/night temperature, 70% RH and a photoperiod of 16h per day. Until symptom appearance plant leaves were moistened using a spray flask once per day.

B. graminis f. sp. *tritici* was inoculated with conidia by consistently agitating and moving sporulating plants above the plants to be infected. Inoculated plants (cv. Taifun) were kept in a separate chamber in the greenhouse.

Hyperspectral time series measurements

The investigated pathogens have characteristic latency phases and differing dynamics of disease development, thus the interval for hyperspectral imaging was individual, depending on the pathogen. This individuality resulted in distinct time series and measuring days per pathogen. The individual workflows for each disease are presented in figure 1. Disease process of DTR was measured daily from 3 to 15 days after inoculation (dai). STB was measured every day from 4 to 31 dai while BR was measured daily from 3 to 12 dai. The time series of YR was

taken daily from 2 to 31 dai and from 1 to 12 dai with an additional measurement 16 dai PM was measured.

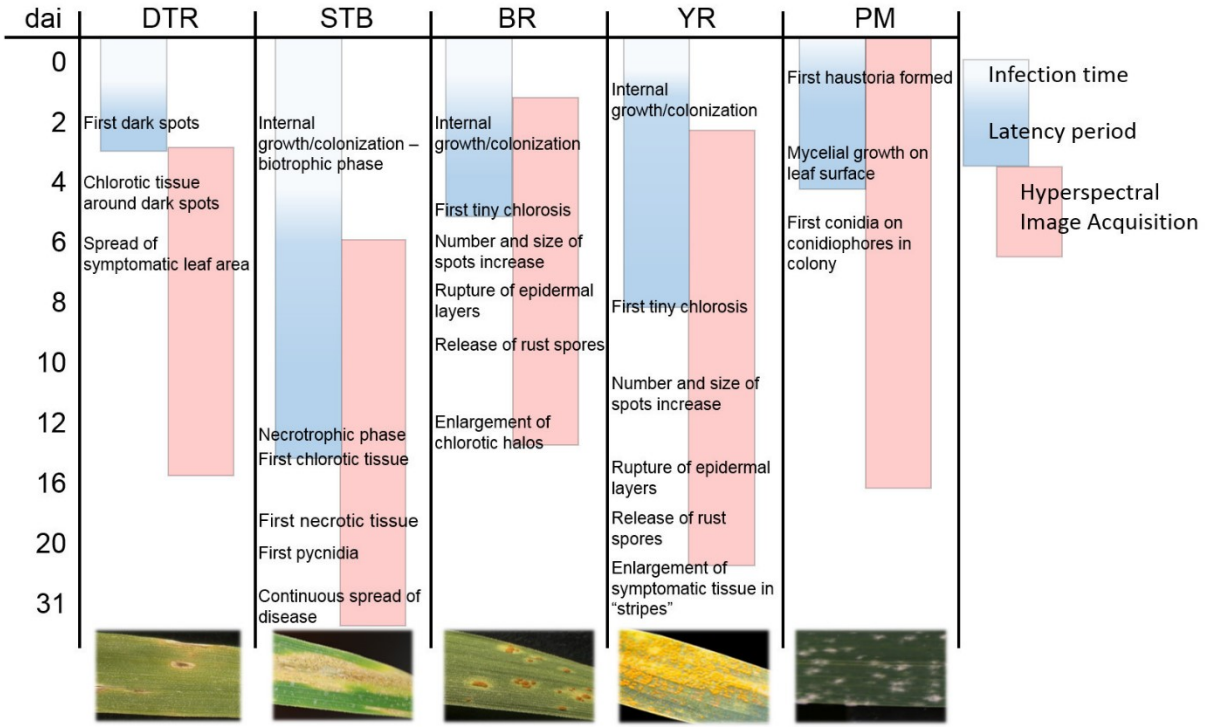

Fig. 1. Sketches of temporal progress and workflow depending on the individual lifestyle of foliar diseases of wheat. Each column contains the duration, in days after inoculation (dai), of the incubation, the latency period, the hyperspectral image acquisition and biological processes in relation to specific time points during pathogenesis. Tan spot (DTR), septoria tritici blotch (STB), brown rust (BR), yellow rust (YR) and powdery mildew (PM).

Hyperspectral imaging was performed with a Specim V10 (VNIR 400-1000 nm) and a Specim SWIR (1000-2500 nm) camera (Specim, Spectral Imaging Ltd., Oulu, Finland). Camera details, measuring setup, and data processing are described in detail in Behmann et al. (2018).

In each of the five time series 16 intact leaves were measured multi-temporal. Four leaves were used from the mock control while 12 leaves were on inoculated plants. According to Behmann et al. (2018) Leaves were fixed in trays by threads to achieve a homogeneous and stable horizontal alignment with adaxial leaf side to the lens of the camera. The threads of the tray formed segments of the leaves. The segments were marked with white marker spots of about 1 mm diameter to facilitate the manual assignment of certain pixels or symptoms on the leaf on different measuring dates. With this experimental design, measurement conditions were kept as homogeneous as possible during the whole time series to gain reproducible data. Plants were provided with water and nutrients as necessary to prevent abiotic stress. All

experiments were repeated three times. Through a distance of 42.5 cm from the object to the lenses of the cameras one pixel had the size of 0.02 mm^2 in VNIR and 0.22 mm^2 in SWIR. For the calculation of reflectance based on radiance measurements, image acquisition consisted of four images: the barium sulfate based white reference (WR) plus its dark current (DC_W) and the plant image (PI) plus its dark current (DC_P). Images were normalized by calculating the ratio of the dark-subtracted plant image and the dark-subtracted white reference as follows: $(PI\text{-}DC_P)/(WR\text{-}DC_W)$. The reflectance spectra were smoothed using a 1D Savitzky-Golay filter (Savitzky and Golay, 1964). Parameters for the smoothing process were five centered supporting points and a third degree polynomial.

Data analysis of hyperspectral images

The data analysis of hyperspectral images was done in ENVI Classic 5.3 (Exelis Visual Information Solutions, Boulder, CO, USA). The "Region of Interest (ROI)" tool was used to observe spectral changes of the leaf surfaces retrospectively. Therefore, certain pixels of a disease specific symptomatic area at the end of the time series measurements was chosen and traced back in time retrospectively as described by Mahlein et al. (2012a). Each spectrum of the VNIR range is represented by 50 pixels and each spectrum of the SWIR range is represented by 10 pixels due to lower resolution of the camera.

Each pathogenesis was characterized by defining four representative hyperspectral Turning points. These Turning points consist of a spectral signature of a plant disease that is prestigious to a developmental stage of the pathogen during pathogenesis. Spectral changes were linked to simultaneous biochemical processes that happen in the host tissue due to host pathogen interaction.

The spectral information of disease dynamics was combined in a spectral library. The spectral library was used to train a classifier for image analysis. The classification of hyperspectral images was performed by the spectral angle mapper algorithm (SAM) (Kruse et al. 1993). SAM is a supervised classifier that can assign a pixel to one of the learned classes. Thereby, each of the classes is represented by one reference spectrum and the spectral catchment area. The spectral resemblance between the pixel and each reference spectrum was calculated by the spectral angle between the vectors of the reference spectrum and the spectrum to be classified (Kruse et al. 1993). The classification of hyperspectral images was done by using a fixed set of hyperspectral data and two disease-plant-complex specific spectra of the spectral

library as reference spectra. The fixed set included a spectrum of the non-infected control, an early stage spectrum of the specific disease and a late stage spectrum of each disease. The spectral catchment area was set to a value of 0.2 for each control to favor the classification of green leaf area and 0.1 for the other classes. These values were identical in each classification and just the spectra of early symptoms and the control were exchanged for other diseases. A classification of early symptoms of different diseases was consciously avoided. The classification results were analyzed by using the ROI tool over the classified leaf to get proportionally information about the number of pixels classified into a certain class. Percentage values were round to the first decimal places. The spectral information for illustration of time series measurements was plotted in SigmaPlot version 11.0 (Systat Software GmbH, Erkrath, Germany).

Microscopic methods

Microscopically investigations of the host-parasite interaction over time were done by fluorescence microscopy. Sampling was performed on each day that hyperspectral images were taken. Fungal structures were stained with the fluorochrome Uvitex 2B according to Dugyala et al. (2015). Leaf sections of 25 mm^2 were bleached in Farmer's Fixative (3:1, ethanol:acetic acid), then soaked in 0.1M Tris-HCl and stained with 0.01 % Uvitex 2B. Samples were stored in 50% Glycerol. Fungal structures showed a bright blue fluorescence while plant cells did not incorporate the dye. Fluorescence microscopy was done by using a Leitz DMRB microscope (Leica Microsystems, Wetzlar, Germany) with a 100- and a 200-fold magnification combined with a Hitachi CCD HV-C20 camera (Hitachi Europe GmbH, Düsseldorf, Germany). The used filters for fluorescence excitation were in the range from 340-380 nm, 355-425 nm and 490-560 nm. For image acquisition and management, the imaging software Discus (Carl H. Hilgers, Königswinter, Germany) was used.

2.4 Results

Hyperspectral signatures of foliar diseases corresponding to histological development

The data of fluorescence microscopy and hyperspectral imaging were compared to define four spectral Turning points (TP) for each disease. Each Turning point shows a specific spectral signature that represents a certain developmental stage of pathogenesis. To ensure that the spectral changes were not caused by leaf senescence or other environmental factors, the spectra of non-infected leaves were compared over the time series. No significant spectral differences were found.

Tan spot

Spectral signatures 3, 7 and 10 dai (TP1, TP2 and TP3) of DTR diseased leaves were slightly different to the uninfected control (Fig. 2 (I) A). Microscopy showed a rapid fungal growth in the host tissue in the first hours after inoculation. However, hyperspectral measurements could not be performed to monitor early development due to requirements for inoculation. Microscopy images represent fungal development in the host tissue during the first seven days. With ongoing pathogenesis, a further spread of the disease was observed. This spread of necrotic area was defined as the Turning points as it affects the spectral signature more than the fungal growth in the first three days. The Green peak stayed visible but a slight continuous increase of reflectance in the range of 580 – 780 nm could be observed. Microscopically investigation of the host tissue showed a yellowish auto fluorescence in the walls of epidermal cells that were penetrated by *D. tritici-repentis* 24 h after inoculation. A yellow auto fluorescence could be detected between intercellular spaces of mesophyll cells 48 hai. Dark spots with no auto fluorescence appeared 72 hai. These spots were surrounded by yellow fluorescing mesophyll cells similar to that initial spot observed 48 hai. From 79 hai on the black spots and the auto fluorescing border tissue emerged. On TP 4, 15 dai, there was a distinct increase in the spectral Blue range from 440 to 500 nm and a strong increase in the range of 550 to 650 nm. On 15 dai there was still a strong absorption from 650 to 700 nm. The NIR range showed a clear tendency to decrease in further pathogenesis. The typical plateau of healthy plant leaves in the NIR mitigates with disease development. While TP2 and 3 (7 and 10 dai) are nearly congruent in the NIR range, the NIR-plateau is vanished at TP4 (15 dai). From TP2 to 3 (7 to 10 dai) the disease progress does not affect the NIR range. The SWIR range is mainly affected by the water absorption bands at 1420 nm and 1920 nm. Spectral signatures

show a strong increase of this bands over time. The differences of TP2 and 3 appear more obvious in SWIR than in VNIR. At 15 dai there is a strong increase in reflection intensity over the entire range. In general, the SWIR curve loses its round shape in later days of pathogenesis and the spectrum seems more erratically.

Septoria tritici blotch

The spectral signatures of the Turning points for STB diseased leaves showed a continuous increase of reflectance in VIS and NIR range, while no fungal structures of *Z. tritici* could be observed in the host tissue before 15 dai (Fig. 2 (I) B). TP1 and TP2 (15 and 21 dai) were very similar to each other in the blue range from 400 – 500 nm and in the NIR range from 700 to 900 nm, but TP2 (21 dai) showed an increased reflectance from 550 to 700 nm. The SWIR range showed a slight increase for TP1 and TP2 but no strong differences between them. A dense mesh of mycelium in the intercellular space of the mesophyll tissue was visible on TP2. First pycnidia were formed. A strong increase in the blue range from 400 to 500 nm and from 550 to 700 nm could be observed on TP3 (28 dai). The Green peak almost disappeared. A distinct increase of the water absorption bands appears, but the spectral signature preserves its shape. The intercellular space was completely filled with mycelium. Pycnidia developed a dark color. Especially on TP4 (31 dai) the Green peak was completely vanished. The curve is steeper and shows a strong descent from 650 to 680 nm, which was also observed for the DTR interaction. The curve is slightly flatted in the NIR plateau and shows an increased reflectance compared to the control. The whole reflectance in the SWIR is increased and the distances between highest and lowest peaks decrease. Ripe pycnidia were visible. Necrotization of plant leaves was intense. Residues with a yellow auto fluorescence could be observed in fluorescence microscopy.

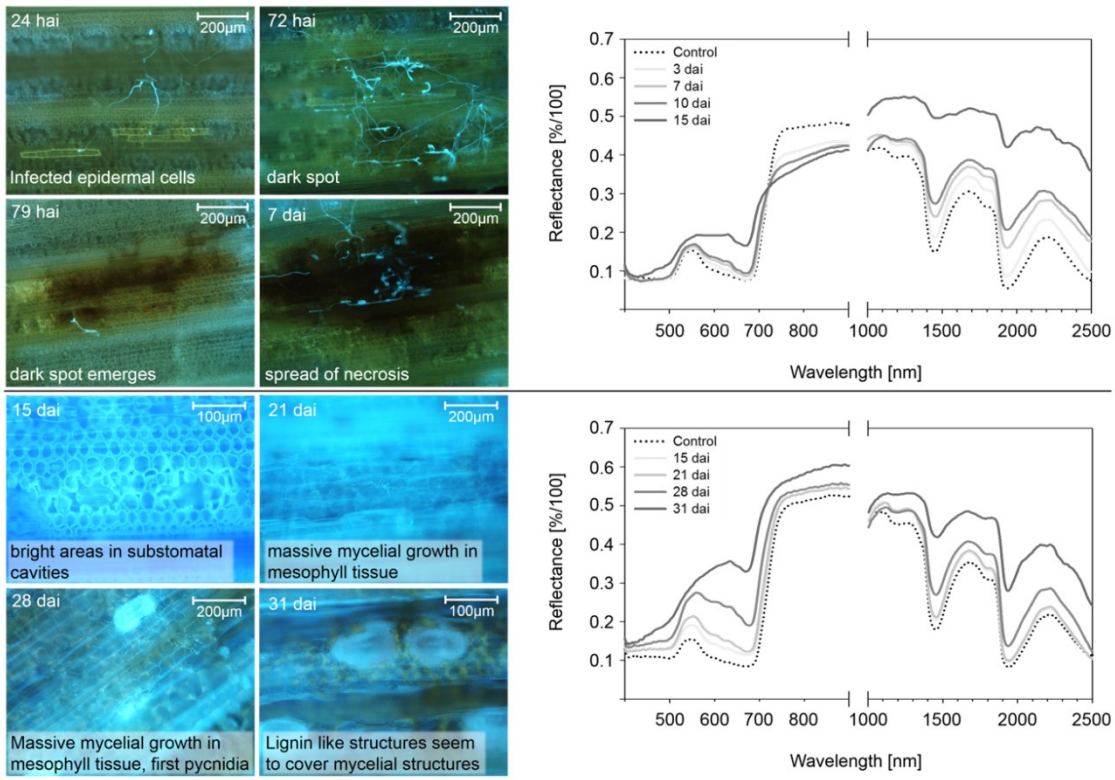

Fig. 2 (I). Histological development of necrotrophic diseases of wheat (left) corresponding to hyperspectral signatures (right). Combination of data from time series of fluorescence microscopy and hyperspectral measurements. Histological development and spectral dynamics are shown for the four measuring dates with Turning points indicating new processes in disease development and shifts in the spectral signature. **A** tan spot disease, **B** septoria tritici blotch. Each spectrum VNIR n=50 pixels, each spectrum SWIR n=10 pixels.

Brown rust

On TP1 and TP2 (4 and 7 dai) the spectral signatures of BR diseased leaves showed similar intensities in the range of 400 to 500 nm (Fig. 2 (II) A). Compared to TP1, TP2showed a greater increase from 500 to 700 nm, but the Green peak could still be observed. The NIR range was still equal and the plateau on the same level. Mycelial structures were observed in between the mesophyll cells on TP1. The mycelium spread and formed primary uredinia at TP2. At this time point colonies were not ripe and completely covered by the cuticle. Urediniospores showed different fluorescence colors and seemed to be in different ripening stages. On TP3 (9 dai) a distinct increase of the absorption in the blue range was visible. The intensity was decreased to the values of the control again. The curve was also decreased from 500 to 580 nm, but showed a further increase from 580 to 700 nm. The Green peak was strongly mitigated. The NIR plateau started to decline under the control, but subtended the earlier

days at 800 nm. A rupture of the cuticle and a release of urediniospores was observed. On TP4 (12 dai) a stronger absorption in the blue range was observed. The absorption rates were higher than those of the non-infected control. The absorption had a maximum at 430 nm. The Green peak is flattened and the curve slightly shifted to higher wavelengths. There was a decrease of the intensity from 550 to 600 nm, but the reflectance intensity was still higher compared to the control. A strong increase from 600 to 700 nm occurred on TP4. Compared to the other diseases, BR did not show the descent at 650 to 700 nm. The NIR plateau was flattened. In histological investigations, a showed massive sporulation and a distribution of urediniospores was observed on the whole leaf sample. The SWIR region was not affected by BR thus far. An increase over the time series could be observed, but water absorption bands stayed clearly visible over the time. TP1 and TP2 were almost congruent. The intensity increased the next days until TP4 but the shape of the curve did not seem to be affected.

Yellow rust

The spectral signatures of YR diseased leaves on TP1 (7 dai) showed a first slight increase over the whole VNIR range (Fig. 2 (II) B). A first spread of fungal hyphae can be observed in the mesophyll. TP2 (10 dai) showed further increase of the reflectance intensity especially from 550 to 680 nm. From 680 to 900 nm TP1 and TP2 were congruent. Fungal colonies showed a stripe-type colonization of the host tissue. On TP3 (15 dai) the spectral signature showed a strong increase in the range from 400 – 680 nm, especially the range 500 to 700 nm was intensely increased. The NIR range seemed to be steady and was almost congruent with TP1 and TP2. Primary uredinia could be found in colonies and were completely covered by the epidermis. The uredinia contained hyaline to dark brown urediniospores, looking similar to those color types observed in the BR interaction. On TP4 (21 dai) a further increase from 400 to 700 nm could be observed. Especially the region at 550 to 650 nm showed a strong increase. The descent from 640 to 680 nm was also visible in the YR interaction. The NIR plateau was still visible and TP4 showed the same reflectance levels in the NIR region like TP1, TP2 and TP3. Sporulation of uredinia could be observed, the epidermis was ruptured. The SWIR region showed a distinct increase of the spectrum on TP4. TP1, TP2 and TP3 were on one level with the control and almost congruent. The SWIR region was not influenced by YR.

Powdery mildew

In general, the spectral signatures of PM Turning points act as a parallel shift of the spectrum (Fig. 2 (II) C). The spectrum of TP1 (4 dai) looked like a parallel shift of the control with increased intensity. The Green peak was clearly visible. Mycelial growth on the leaf surface could be observed. TP2 (9 dai) showed an increased reflectance intensity from 400 to 700 nm. The Green peak seemed more indistinct. The Blue peak signified a peak at 460 nm. The NIR region was decreased compared to TP1 and on the level of the control. A dense growth of mycelium could be observed. Fungal sporulation was visible. The Green peak was nearly vanished on TP3 (12 dai) and the Blue peak at 460 nm was more distinct. The NIR region slightly increased compared to TP1. The spectral signature of TP4 (16 dai) showed a strong increase of reflectance from 400 to 900 nm. A clear Blue peak was visible at 460 nm while the Green peak was completely gone. The curve lost its shape from 400 to 700 nm and developed a high gradient. The values in the NIR region were highest for TP4 but the plateau maintained. The PM interaction did not exhibit a descent in the range from 650 to 680 nm. A strong growth and sporulation was obvious for TP3 and TP4, leaf samples were overgrown by the fungus. The SWIR region showed a continuous increase of the spectral signatures over time with the highest values on TP4. The curves stayed in typical shape and did not show big differences in their course.

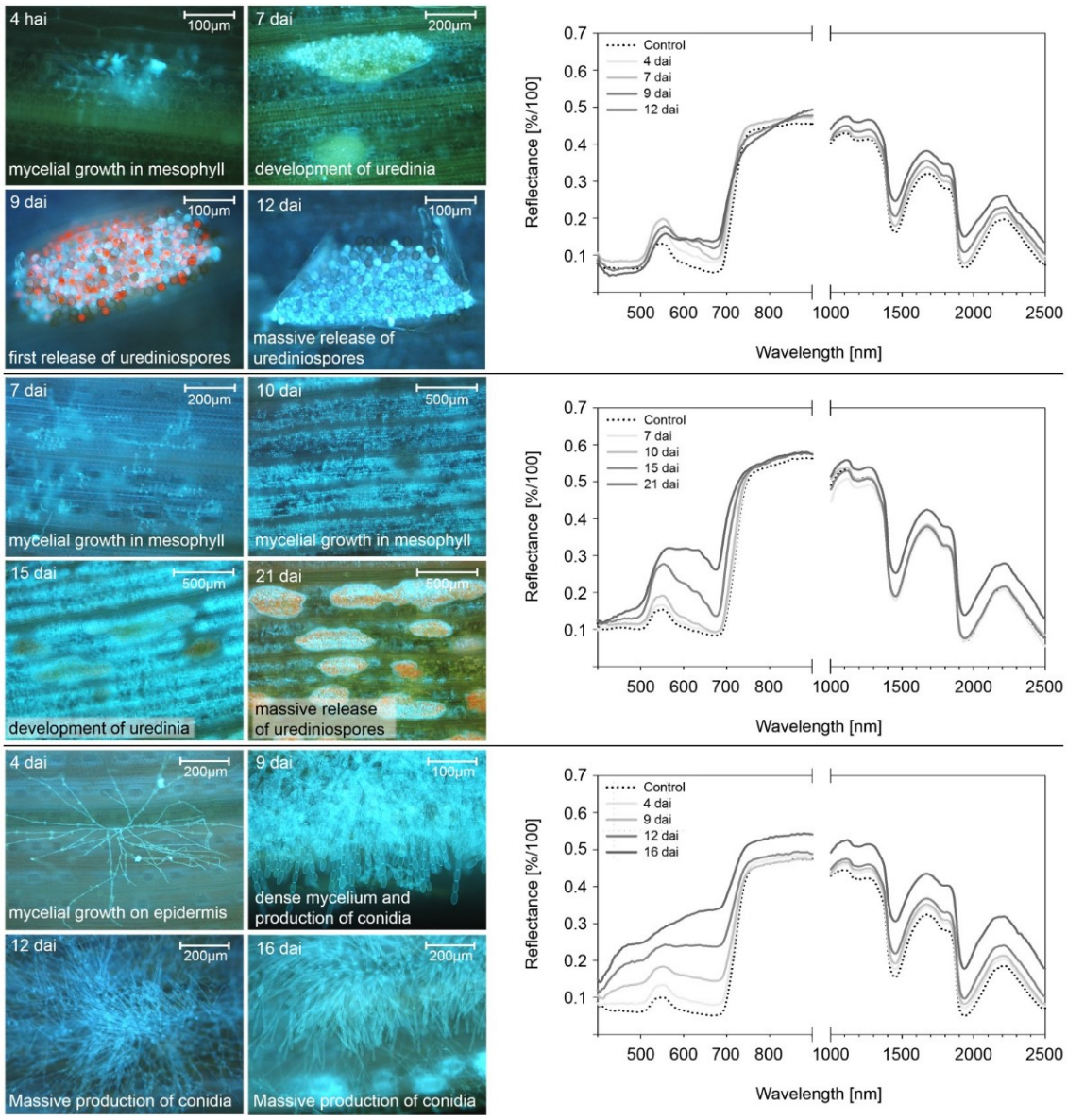

Fig. 2 (II). Histological development of biotrophic diseases of wheat (left) corresponding to hyperspectral signatures (right). Combination of data from time series of fluorescence microscopy and hyperspectral measurements. Histological development and spectral dynamics are shown for the four measuring dates with Turning points indicating new processes in disease development and shifts in the spectral signature. **A** brown rust, **B** yellow rust, **C** powdery mildew. Each spectrum VNIR n=50 pixels, each spectrum SWIR n=10 pixels.

Comparison between spectral dynamics of different diseases

Comparing the spectral information of the different diseases, distinct differences characterize the dynamic of each disease (Table 1). DTR is the only disease that shows a constant decrease of reflectance in the NIR range on all Turning points. The NIR plateau is flattened most, compared to the other diseases. STB and PM are the only diseases that show a constant and strong increase of the NIR plateau while STB seems to have a flattening effect on the plateau. BR shows an increased absorption in the blue range from 400 to 500 nm on later Turning

points while YR shows an increased reflectance. Both rust diseases do not seem to have a strong effect on the NIR plateau while BR shows a decreased reflectance on later Turning points and YR keeps one level of reflectance during pathogenesis. BR is the only disease that does not show the descent from 650 to 700 nm on the last Turning point. The decrease from 500 to 580 nm followed by the increase from 580 to 700 nm is characteristic. YR shows a strong increase from 500 to 650 nm. The PM spectra are parallel shifts with a weakened Green peak while a Blue peak seems to appear on later Turning points. In general, the SWIR region seemed to be similar for all diseases and did not show that distinct characteristics compared to the VNIR region. The necrotrophic diseases, DTR and STB, affected the SWIR region more intense than the biotrophic rust fungi and PM.

	DTR	STB	BR	YR	PM
Blue region	↑	↑	↓	↑	↑
Green peak	→	↑	↓	↑	↑
Red edge	↑	↑	↑	↑	↑
NIR	↓	↑	↓	→	↑
SWIR	↑	↑	→	→	↑

↑ increase ↓ decrease → constant

Table 1. Spectral regions of the electromagnetic spectrum that are influenced by different foliar diseases of wheat. Colored boxes indicate a certain alteration that is specific to one disease. Tan spot (DTR), septoria tritici blotch (STB), brown rust (BR), yellow rust (YR) and powdery mildew (PM).

Classification of necrotizing diseases based on spectral library

The classification of necrotizing diseases showed, that a necrosis is more unspecific compared to the symptoms of biotrophic pathogens. Detailed information about the classification results of all diseases is given in Table 2. Classification results of a leaf infected with DTR 3 dai emerged that already 92.8 % of leaf pixels were classified as early symptomatic and 4.5 % as healthy (Fig. 3). The amount of pixels classified as other diseases was low (<1 %) and often located in transition areas to marker spots. The leaf had a calculated diseased area of 93.3 %. In later pathogenesis 15 dai 42.2 % of the leaf were classified as early symptomatic while 4.5 % were classified as late stage symptoms of DTR. The amount of pixels classified as other diseases was high. Especially pixels classified as YR (21.9 %) and STB (9.8 %) were overrepresented. YR was

classified to a higher amount in the border regions of the necrotic area, while STB and PM classification were located in the center of necrosis. The leaf had a calculated diseased area of 84.3 %.

Classification results of a leaf infected with STB 21 dai showed that 6.7 % of leaf area was classified as early symptomatic and 91.6 % as healthy. The amount of pixels classified as other diseases was low (<1 %). Chlorotic tissue that was already visible by the eye was classified as early symptomatic. Leaf edges and outer transition areas of marker spots were frequently classified as early symptom. Areas of high reflectance values were classified as early symptomatic. The leaf had a calculated diseased area of 6.8 %. The results 31 dai indicated that 30.1 % were divided as early symptomatic, 2.4 % as late stage STB, and 58.5 % as healthy. DTR and YR are represented in higher amounts than STB. Areas of bright illumination were classified as early symptomatic but might occur healthy on the RGB visualization. Necrotic tissue was classified as late symptoms of STB, but these lesions were mostly surrounded by pixels classified as DTR and YR. An especially bright necrosis on the leaf edge was classified as PM. In general, a distinct higher number of pixels was classified as early symptomatic as they were visible as chlorotic on the RGB visualization. In classification results it is obvious that transition areas from early to late symptom show pixels classified as other diseases. The leaf had a calculated diseased area of 39.8 %.

Classification of diseases with biotrophic lifestyles based on spectral library

In general, the classification of the diseases caused by biotrophic pathogens was more specific compared to necrotizing diseases. The amount of pixels classified as other diseases was lower and classifications appeared more zoned. On a BR infected leaf 7 dai, 32 % of leaf area was classified as early symptomatic and 66.3 % was classified as healthy. The leaf showed a clear segregation into these two classes and the amount of pixels classified as other diseases was low (<1 %). Also here these pixels were located in transition areas to the marker spots. Some pixels of leaf veins were classified as early symptomatic. The calculated diseased area was 31.9 %. On 12 dai the leaf was mainly separated into early symptomatic (45.6 %), late stage BR (5 %) and healthy (47.8 %). In most cases, pixels classified as BR were surrounded by early symptomatic pixels. The amount of pixels classified as other diseases was still low (<1 %). The leaf had a calculated diseased area of 50.6 %.

A YR infected leaf showed a clear segregation in early symptomatic (9.7 %) and healthy (88.2 %) 15 dai. The amount of pixels classified as other diseases was low (<1 %). The SAM visualization showed no distinct point chlorosis compared to BR. The leaf had a calculated diseased area of 9.9 %. On 21 dai the leaf showed an increase of early symptomatic pixels up to 24.3 % and 2.9 % late stage YR. Healthy pixels were reduced to 68 %. A great number of spore bunches, 1 % of leaf area, were classified as late symptom of BR instead of YR. DTR has a certain amount of pixels in transition areas from early to late symptoms of YR. Pixels classified as STB are located in the center of YR symptoms. The leaf had a calculated diseased area of 30.7 %.

PM classification of a leaf 9 dai showed a clear segregation of leaf area into early symptomatic (3.8 %) and healthy (93.3 %). In the center of early symptoms, some pixels were classified as late stage symptoms of PM (0.1 %). BR was classified in the transition regions of marker spots (0.3 %). The calculated infection was 4.2 %. On 12 dai 9.4 % of leaf pixels were calculated as early symptomatic and 6.3 % as late stage PM. 79.6 % of leaf area was classified as healthy. At 9 dai the pixels classified as diseased increased in areas where PM was detected. Wrong classifications of other diseases again happened in transition areas from early to late symptoms. These transition areas often consisted of one row of pixels surrounding a late stage symptom of PM. The leaf had a calculated infection of 17.2 %.

	DTR 3 dai	DTR 12 dai	STB 21 dai	STB 31 dai	BR 7 dai	BR 12 dai	YR 15 dai	YR 21 dai	PM 9 dai	PM 16 dai
healthy	4.9	10	91.6	58.1	66.3	47.8	88.2	68	93.3	79.6
early symptom	92.8	42.2	6.7	30.1	32	45.6	9.7	24.3	3.8	9.4
DTR	0.2	4.5	0	3.6	0.1	0.2	0	0.8	0	0.9
STB	0	9.8	0	2.4	0	0	0	0.5	0	0.4
BR	0	0	0	0	0	5	0	1	0.3	0.2
YR	0.2	21.9	0	2.8	0.1	0.1	0	2.9	0	0.2
PM	0.2	5.9	0.2	0.8	0.2	0.2	0.2	0.3	0.1	6.3
dis. leaf area	93.3	84.3	6.8	39.8	31.9	50.6	9.9	30.7	4.2	17.2

Table 2. Spectral angle mapper classification of diseased wheat leafs separated into different classes of the spectral library (in percent pixels of wheat leaf). Values are calculated for two different Turning points during pathogenesis. Grey pixels indicate the amount of pixels classified as early symptomatic and the late stage symptoms of each disease. Tan spot (DTR), septoria tritici blotch (STB), brown rust (BR), yellow rust (YR) and powdery mildew (PM).

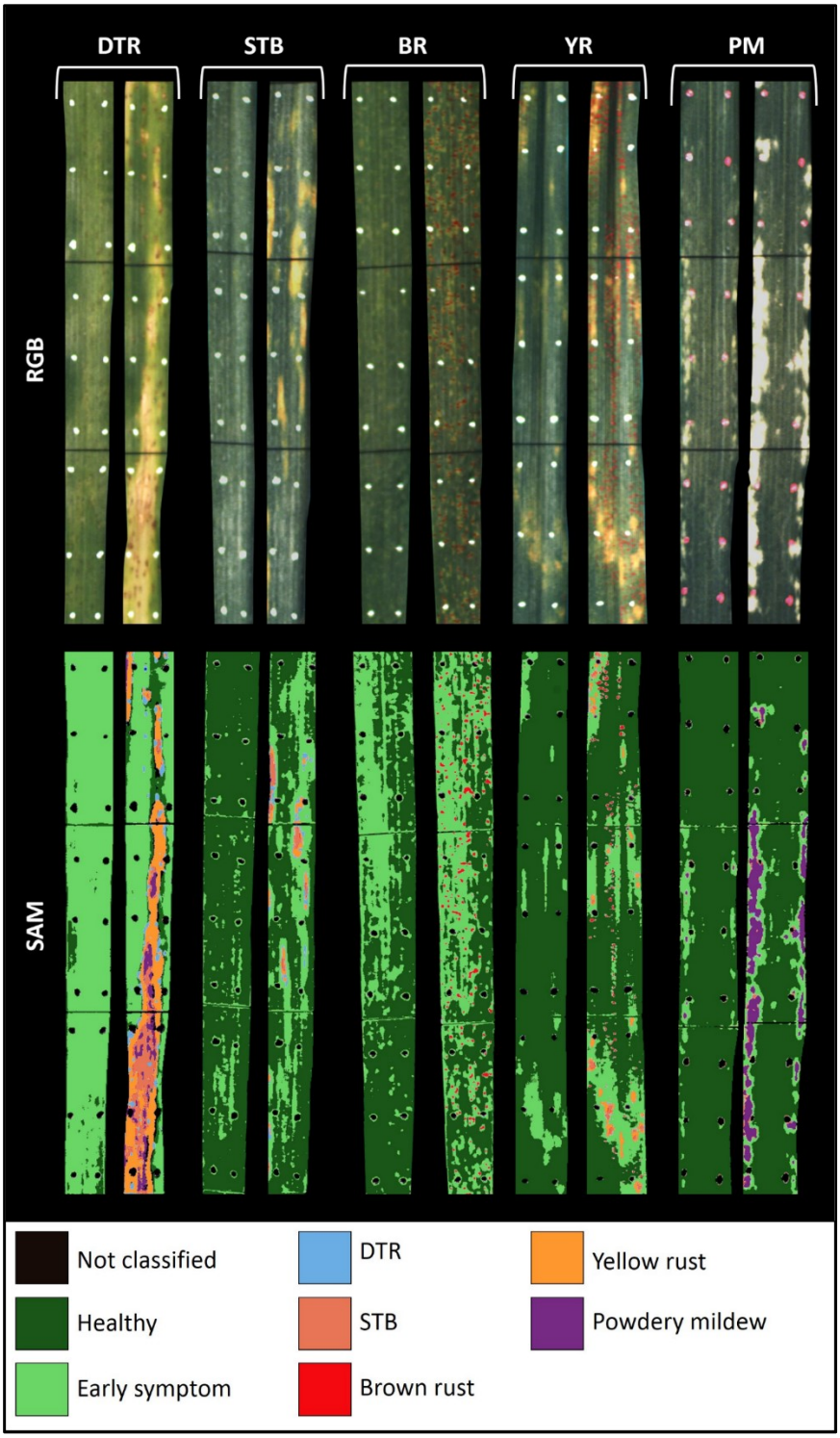

Fig. 3. Spectral angle mapper (SAM) classifications of early and late stage symptoms of different foliar diseases of wheat corresponding to RGB visualizations of hyperspectral images. Each disease is presented on two measuring dates during pathogenesis. SAM classification images are presented below the corresponding hyperspectral image. First image of each disease group shows an RGB visualization of the early stage symptomatic leaf followed by the corresponding SAM image. The next leaf shows the RGB visualization of the late stage symptomatic leaf followed by its SAM classification (Reference spectra base on the spectral information shown in figure 2). Tan spot (DTR), septoria tritici blotch (STB), brown rust (BR), yellow rust (YR) and powdery mildew (PM).

2.5 Discussion and conclusion

Plant diseases exhibit different biological features that can be linked to certain spectral alterations during pathogenesis. Reflectance values of a healthy leaf are low at 400 – 700 nm due to photosynthetic active pigments, which absorb peculiarly from 425 – 492 nm (Blue region) and 645 – 700 nm (Red region). Reflectance values in the NIR (700 – 1300 nm) are high due to the multiple scattering at the air-cell interfaces within leaf tissue (Gates et al. 1965; West et al. 2003; Kuska et al. 2015). The generation of hyperspectral time series showed that each disease led to characteristic spectra, depending on the pathogenesis. Individuality can also be a sum of spectral properties of different regions over the spectral range, resulting in a specific combination of spectral features (Table 1). Necrotrophic fungi cause the collapse of leaf structures and necrotic lesions on the leaf. The necrotic area is more unspecific in contrast to characteristic spore stocks of rust fungi and powdery mildew. Fungal structures of biotrophic pathogens on the leaf surface had more impact on the individual spectral fingerprint than structures of the necrotrophic pathogens.

The spectral dynamic of DTR showed a characteristic decrease of reflectance in the NIR plateau (Fig. 2(I)). The NIR plateau is mainly influenced by the plants leaf tissue and cell structure (Elvidge 1990). A degradation of those compounds like fructose, glucose, starch and proteins leads to a decrease in the NIR plateau of DTR infected leaves. Mahlein et al. (2012a) and Leucker et al. (2016) showed that dark pigments, toxin production and cell degradation in the centers of Cercospora leaf spot symptoms might lead to a reduced reflectance intensity. The dark tan spot is caused by a host specific toxin produced by the fungus (Tomas and Bockus 1987). Thus the presence of the dark tan spot could explain the decrease of the NIR plateau. An enrichment of substances that emit a yellow fluorescence was observed with microscopy. These substances might be part of a lignin-based defense mechanism of the plant against the pathogen (Dushnicky et al. 1998). The SAM classification of DTR showed that misclassifications into YR (21.9 %) and STB (9.8 %) were present in the late pathogenesis stages. Only 4.5 % of pixels were classified as late stage symptoms of DTR. This low amount can be explained by the annotation of pixels for the extraction of reference spectra by human beings. Reference pixels were taken over time from the same dark spots that appeared as first symptoms. The overrepresentation of YR and STB could be due to the unspecificity of necrosis with absence of masses of characteristic fungal structures.

STB infected leaves showed an increased reflection in all spectral regions (Fig. 2(I)). Through degradation of chlorophyll the Green peak disappeared. In comparison to DTR, the NIR plateau increased, although the symptoms and the necrosis resemble to a DTR symptom. This increase might happen because STB does not form dark spots except for pycnidia with a size of 60 – 200 µm (Eyal et al. 1987). In the used measuring setup for VNIR image acquisition, pycnidia with an average size of 60 – 200 µm were too small to visualize in one pixel with a side length of 0.15 mm. The increase in the Blue region is caused by the degradation of pigments, such as chlorophylls (Lichtenthaler and Bushmann 2001). Classification results of the STB pathogenesis indicated higher amounts of pixels classified as DTR and YR than for STB (2.4 %). STB is augmented classified in the necrotic centers, while DTR and YR are classified in transition areas from chlorotic to necrotic tissue. The transition areas could be similar in kind to the late stage symptoms of the disease. Another reason is the unspecificity of STB necrosis compared to DTR or necrosis induced by total degradation of chlorophyll through YR.

Leaves affected by BR showed a characteristic decrease of reflectance in the Blue region, an increase from 580 to 700 nm and a decrease of the NIR plateau around 750 nm (Fig. 2(II) a). The pigmented urediniospores of *P. triticina* are red to brown in color (Bolton et al. 2008; McTaggart et al. 2014). The color of these spores is related to the presence of carotenoids (Hennessy and Sackston 1972). Carotenoids are pigments that absorb light in the Blue region (Elvidge 1990; Lichtenthaler and Buschmann 2001). A massive production of spores leads to higher absorption rates in the Blue region and consequential decreased reflectance intensities. The increased reflectance at 580 to 700 nm (red color range) was caused by the pigmentation of the spores. The absence of a descent at 650 to 700 nm was characteristic to BR. This descent stayed visible in the other pathogen time series and showed absorption maxima of chlorophyll a and b (Chapelle et al. 1992). Presumably the signal of these maxima were superimposed by the density of spores in the uredinium. The density of urediniospores could also affect the NIR-plateau due to the overlay of leave tissue. The leaf structure signal was amended and the NIR plateau decreased. The classification results of BR disease showed a clear segregation in diseased and healthy leaf area.

The spectra of YR disease showed a constant increase of reflectance from 400 to 700 nm. YR did not show an increased absorption in the Blue range in contrast to BR, although urediniospores of YR contain carotenoids (Zwetko and Pfeifhofer 1991). This could be

explained by a total degradation of chlorophyll that absorbs in the Blue range (Lichtenthaler and Buschmann 2001) and a different carotenoid composition (Irvine et al. 1954; Zwetko and Pfeifhofer 1991) and. All carotenoid pathways have in common the introduction of conjugated double bonds on phytoene to produce different colored intermediates and the cyclization (introduction of α- or β-ionone rings) of one or the two ends of the polyene chain to generate the characteristic carotenoid structures. After formation of the colorless phytoene conjugated double bonds are introduced in the molecule. An increasing number of double bonds in the molecules shifts the absorption maximum towards longer wavelength, resulting in the different yellow to red colors of the desaturation products. An additional affect may be a varying thickness or density of the spore layer between YR and BR allowing a higher leaf signal proportion in the YR spectra. The NIR plateau is unaffected and plant structure seems to be obtained during infection with biotrophic fungi. Maybe the effect of YR on the NIR plateau is also less strong because of the varying density of spores on the leaf compared to BR and the leaf signal is still dominant. In general, SAM classification of YR operated and there was little misclassification except for STB and BR. STB was classified in areas with bright pixels were high infection leads to total degradation of chlorophyll or beginning necrosis of the leaf.

The spectral dynamic of PM looks like a parallel shift of the curve with mitigated leaf signal on later Turning points. Kuska et al. (2015) and Wahabzada et al. (2016) described constant reflectance increases of the full VIS NIR range for powdery mildew on barley. The reflectance intensity increases with density of fungal structures on the leaf surface. On later Turning points the Green peak is gone and an increase in the spectral border range in the Blue region emerges. Mycelium and conidia of PM are hyaline and non-pigmented (Zhang et al. 2005). PM forms a dense net of hyphae and spores on the leaf surface that increase reflectance intensity and cover characteristic spectral features of the leaf signal. The SAM classifier was robust on PM detection.

Even under controlled conditions, the spectrum is always a mixed signal with various factors influencing its composition. Actually spectral signatures of different cultivars differ from each other and this difference has to be examined in future works. The SAM is depending on means of spectra. Algorithms that automatically subtract the part of the spectrum that is influenced by cultivar differences or other components could help future characterization of materials in

spectroscopy. Machine learning and improvement of algorithms might favor robust handling of mixed signals (Behmann et al. 2014).

This work presents, for the first time, a library of the spectral dynamics of five foliar diseases of wheat. The spectral dynamic is described with four Turning points for each disease that are combined in a time series. The spectral library was used as input for a SAM classifier to test the potential of gathered spectral information as a compendium for disease detection, identification and quantification. The library could also be used as input data for other algorithms such as support vector machines. Further work is necessary to verify the resilience of this spectral information for a transmission from leaf-scale to higher scales such as the canopy- or UAV-scale und uncontrolled field conditions where biological heterogeneity is present at all times. Because of the use of packed reference spectra as a compendium for wheat diseases, this approach favors a detection of leaf diseases in the field where plants show different developmental stages of disease specific symptoms at the same time. Our results indicate that spectral libraries give high potentials for an automated disease detection and quantification in commercial use, such as field application, fungicide research or plant resistance phenotyping.

2.6 Acknowledgements

This work was supported by BASF Digital Farming.

2.7 References

Arens N, Backhaus A, Döll S, Fischer S, Seiffert U, Mock H-P, 2016. Non-invasive presymptomatic detection of *Cercospora beticola* infection and identification of early metabolic responses in sugar beet. *Frontiers in Plant Science* **7**, 1377.

Ashourloo D, Mobasheri MR, Huete A, 2014. Developing two spectral indices for detection of wheat leaf rust (*Puccinia triticina*). *Remote Sensing 6*, 4723-40.

Ashourloo D, Aghighi H, Matkan A, Mobasheri M, Moeini Rad A, 2016. An investigation into machine learning regression techniques for the leaf rust disease detection using hyperspectral measurement. *IEEE Journal of Selected Topics in Applied Earth Observations and Remote Sensing* **9**, 1-8.

Behmann J, Mahlein A, Rumpf T, Römer C, Plümer L, 2014. A review of advanced machine learning methods for the detection of biotic stress in precision crop protection. *Precision Agriculture* **16**, 239-260.

Behmann J, Bohnenkamp D, Paulus S, Mahlein AK, 2018. Spatial referencing of hyperspectral images for tracing of plant disease symptoms. *Journal of Imaging* **4**(12).

Bock CH, Poole GH, Parker PE, Gottwald TR, 2010. Plant disease severity estimated visually, by digital photography and image analysis, and by hyperspectral imaging. *Critical Reviews in Plant Sciences* **29**, 59-107.

Bolton MD, Kolmer JA, Garvin DF, 2008. Wheat leaf rust caused by *Puccinia triticina*. *Molecular Plant Pathology* **9**, 563–575.

Bravo C, Moshou D, West J, McCartney A, Ramon H, 2003. Early disease detection in wheat fields using spectral reflectance. *Biosystems Engineering* **84**, 137-145.

Bravo C, Moshou D, Oberti R, West J, McCartney A, Bodria, L, Ramon H, 2004. Foliar disease detection in the field using optical sensor fusion. *Agricultural Engineering International* **6**.

Bundessortenamt, 2018. Beschreibende Sortenliste Getreide, Mais, Öl- und Faserpflanzen, Leguminosen und Zwischenfrüchte. *Bundessortenamt Hannover*.

Chapelle EW, Kim MS, McMurtrey JE III, 1992. Ratio analysis of reflectance spectra (RARS): an algorithm for the remote estimation of the concentrations of chlorophyll A, chlorophyll B, and carotenoids in soybean leaves. *Remote Sensing of Environment* **39**, 239-247.

Cao X, Luo Y, Zhou Y, Fan J, Xu X, West JS, Duan X, Cheng D, 2015. Detection of powdery mildew in two winter wheat plant densities and prediction of grain yield using canopy hyperspectral reflectance. *PLoS ONE* **10**(3).

Chen W, Wellings C, Chen X, Kang Z, Liu T, 2014. Wheat stripe (yellow) rust caused by *Puccinia striiformis* f.sp. *tritici*. *Molecular Plant Pathology* **15**, 433–46.

Dugyala S, Borowicz P, Acevedo M, 2015. Rapid protocol for visualization of rust fungi structures using fluorochrome Uvitex 2B. *Plant Methods* **11**(1).

Dushnicky LG, Balance GM, Sumner MJ, MacGregor AW, 1998. The role of lignification as a resistance mechanism in wheat to a toxin-producing isolate of *Pyrenophora tritici-repentis*. *Canadian Journal of Plant Pathology* **20**(1), 35-47.

Elvidge CD, 1990. Visible and near infrared reflectance characteristics of dry plant materials. *International Journal of Remote Sensing* **11**(10), 1775-1795,

Eyal Z, Scharen AL, Prescott JM, van Ginkel M, 1987. The Septoria diseases of wheat: Concepts and methods of disease management. *CIMMYT*.

Gates DM, Keegan HJ, Schleter JC, Weidner V, 1965. Spectral properties of pants. *Applied Optics* **4**, 11-20.

Hahn M, Mendgen K, 1997. Signal and nutrient exchange at biotrophic plant-fungus interfaces. *Current Opinion in Plant Biology* **4**, 322-27.

Hennessy CMR, Sackston WE, 1972. Inheritance of spore colour in *Puccinia helianthi*. *Canadian Journal of Genetics and Cytology* **14**(2), 271-78.

Hillnhütter C, Mahlein AK, Sikora RA, Oerke, EC, 2011. Remote sensing to detect plant stress induced by *Heterodera schachtii* and *Rhizoctonia solani* in sugar beet fields. *Field Crops Research* **122**, 70–77.

Irvine G, Golubchuk M, Anderson J, 1954. The carotenoid pigments of the uredospores of rustfungi. *Canadian Journal of Agricultural Science* **34**, 234-39.

Kruse FA, Lefkoff AB, Boardman JW, Heidebrecht KB, Shapiro AT, Barloon PJ, Goetz AFH, 1993. The spectral image processing system (SIPS)-interactive visualization and analysis of imaging spectrometer data. *Remote Sensing of the Environment* **44**(2-3), 145-63.

Kuska M, Wahabzada M, Leucker M, Dehne HW, Kersting K, Oerke EC, Steiner U, Mahlein AK, 2015. Hyperspectral phenotyping on the microscopic scale: towards automated chracterization of plant-pathogen interactions. *Plant Methods* **11**(28).

Leucker M, Mahlein AK, Steiner U, Oerke EC, 2016. Improvement of lesion phenotyping in *Cercospora beticola*-sugar beet interaction by hyperspectral imaging, *Phytopathology* **102**(2), 177-84.

Lichtenthaler HK, Buschmann Claus, 2001. Chlorophylls and Carotenoids: Measurement and

Characterization by UV-VIS Spectroscopy. *Current Protocols in Food Analytical Chemistry* **1**(1), F4.3.1-F4.3.8.

Mahlein AK, Steiner U, Hillnhütter C, Dehne HW, Oerke EC, 2012a. Hyperspectral imaging for small-scale analysis of symptoms caused by different sugar beet diseases. *Plant Methods* **8**(3).

Mahlein AK, Oerke EC, Steiner U, Dehne, HW, 2012b. Recent advances in sensing plant diseases for precision crop protection. *European Journal of Plant Pathology* **133**, 197–209.

Mahlein AK, 2016. Plant disease detection by imaging sensors - parallels and scientific demands for precision agriculture and plant phenotyping. *Plant Disease* **100**, 241–51.

Mahlein AK, Kuska MT, Behmann J, Polder G, Walter A, 2018. Hyperspectral sensors and imaging technologies in phytopathology: State of the art. *Annual Review of Phytopathology* **56**, 535-558.

McTaggart A, Geering A, Shivas R, 2014. *Uredinopsis pteridis* and Desmella aneimiae, the first rust fungi (*Pucciniales*) reported on fern (*Pteridophyta*) in Australia. *Australasasian Plant Disease Notes* **9**, 1-4.

Meier U, 2001. Growth stages of mono and dicotyledonous plants. BBCH Monograph. *Federal Biological Research Centre for Agriculture and Forestry Bonn*.

Newton M, Johnson T, 1936. Stripe rust, *Puccinia glumarum* in Canada. *Canadian Journal of Research* **14**, 89-108.

Savitzky A, Golay, MJE, 1964. Smoothing and Differentiation of Data by Simplified Least Squares Procedures. *Analytical Chemistry* **36**, 1627-39.

Steinberg G, 2015. Cell biology of *Zymoseptoria tritici*: Pathogen cell organization and wheat infection. *Fungal Genetics Biology* **79**, 17–23.

Te Beest DE, Paveley ND, Shaw MW, van den Bosch F, 2008. Disease-weather relationships for powdery mildew and yellow rust on winter wheat. *Phytopathology* **98**, 609–17.

Thomas S, Kuska MT, Bohnenkamp D, Brugger A, Alisaac E, Wahabzada M, Behmann J, Mahlein AK, 2017. Benefits of hyperspectral imaging for plant disease detection and plant protection: a technical perspective. *Journal of Plant Diseases and Protection* **125**, 5-20.

Tomas A, Bockus, WW, 1987. Cultivar-specific toxicity of culture filtrates of *Pyrenphora tritici-repentis*. *Phytopathology* **77**, 1337-40.

Wahabzada M, Mahlein AK, Bauckhage C, Steiner U, Oerke EC, Kersting K, 2015. Metro maps of plant disease dynamics—automated mining of differences using hyperspectral images. *PLoS ONE* **10**(1).

Wahabzada M, Mahlein AK, Bauckhage C, Steiner U, Oerke EC, Kersting K, 2016. Plant Phenotyping using Probabilistic Topic Models: Uncovering the Hyperspectral Language of Plants. *Scientific Reports* **6**, 22482.

West J, Bravo C, Oberti R, Lemaire D, Moshou D, McCartney A, Ramon H, 2003. The potential of optical canopy measurement for targeted control of field crop diseases. *Annual Review of Phytopathology* **41**, 593-614.

Whetton R, Waine T, Mouazen A, 2018. Hyperspectral measurements of yellow rust and fusarium head blight in cereal crops: Part 2: On-line field measurement. *Biosystems Engineering* **167**, 144-58.

Yu K, Anderegg J, Mikaberidze A, Karisto P, Mascher F, McDonald BA, Walter A, Hund A, 2018. Hyperspectral canopy sensing of wheat septoria tritici blotch disease. *Frontiers in Plant Science* **9**, 1195.

Zhang Z, Henderson C, Perfect E, Carver LW, Thomas T, Barry J, Skamnioti, P, Gurr S, 2005. Of genes and genomes, needles and haystacks: *Blumeria graminis* and functionality. *Molecular plant pathology* **6**, 561-75.

Zhao YR, Xiaoli L, Yu KQ, Cheng F, He Y, 2016. Hyperspectral imaging for determining pigment contents in cucumber leaves in response of angular leaf spot disease. *Scientific Reports* **6**, 27790

Zwetko P, Pfeifhofer, HW, 1991. Carotene analysis of rust spores - significance for physiology and taxonomy. *Nova Hedwigia* **52**, 251-66.

3 Spatial referencing of hyperspectral images for tracing of plant disease symptoms

This work has been published as:

Behmann, J., Bohnenkamp, D., Paulus, S., & Mahlein, A. K. (2018). Spatial referencing of hyperspectral images for tracing of plant disease symptoms. *Journal of Imaging*, *4*(12), 143.

David Bohnenkamp performed the experiments (100%), DB analyzed the data and wrote the paper (20%).

Text was not modified from the published version.

3.1 Abstract

The characterization of plant disease symptoms by hyperspectral imaging is often limited by the missing ability to investigate early, still invisible states. Automatically tracing the symptom position on the leaf back in time could be a promising approach to overcome this limitation. Therefore, we present a method to spatially reference time series of close range hyperspectral images. Based on reference points, a robust method is presented to derive a suitable transformation model for each observation within a time series experiment. A non-linear 2D polynomial transformation model has been selected to cope with the specific structure and growth processes of wheat leaves. The potential of the method is outlined by an improved labeling procedure for very early symptoms and by extracting spectral characteristics of single symptoms represented by Vegetation Indices over time. The characteristics are extracted for brown rust and septoria tritici blotch on wheat, based on time series observations using a VISNIR (400–1000 nm) hyperspectral camera.

3.2 Introduction

Hyperspectral images of plants are suitable to assess the health and vitality state of plants [1, 2]. Leaf diseases show characteristic symptoms, allowing a hyperspectral characterization of symptom development [1, 3]. The spectral dynamic of symptom development during pathogenesis has been described for numerous plant-pathogen systems [4]. Therefore, hyperspectral imaging has been applied on multiple scales from the leaf level via full plants up to the field and landscape scale [5–8]. Platforms, microscope stands, laboratory systems, high-throughput facilities, as well as Unmanned Aerial Vehicles (UAVs), planes, and satellites are used [5–7, 9, 10]. This publication focuses on tracking leaf diseases of wheat at the leaf scale.

Wheat (Triticum aestivum) is the second most cultivated crop worldwide which is threatened by various pathogens infecting root, stem, leaves, and ears [11]. At the leaf scale, a limiting factor is the natural variability in the spatial and temporal development of disease symptoms [12]. The exact position of symptom appearance and dynamics of development are bound to multiple parameters and, to a certain extent, unpredictable [13, 14]. Therefore, symptoms of different development steps are present at a certain point in time, hampering the clear extraction of the typical symptom development. At best, each symptom has to be traced during the different observation days on its own to have a clearer look on the different steps of pathogenesis. Performing this task is extremely labor intensive and in many situations not feasible, e.g., for the early parts of the pathogenesis before expression of a visible symptom. Few studies have focused this task [5, 6], but are restricted to the characterization of single symptoms instead of extracting a representative description of the pathogenesis.

A further advantage of spatially referenced hyperspectral time series is the generation of large amounts of training data with high quality annotation for the training of machine learning models [15]. Even very early effects of the disease could be included as positions on the leaves showing symptoms at a later point in time are known. The underlying assumption is that if disease symptoms are visible, the first changes could most probably be recorded by the hyperspectral camera a few days earlier. Prerequisite for these applications is a common measurement coordinate system for every image, but its generation on leaf scale is challenging due to leaf movements and growing. The spatial assignment of two images is a common task in computer vision and addressed by the terms image matching or image referencing [16–18]. In remote sensing a joint spatial reference system for multiple observations is often provided by the data distributor. Images are georeferenced by an automatic process to localize reflectance characteristics and perform multi-temporal analyses based on repetitive observations of a location. Space and airborne images are georeferenced either by ground control points with known coordinates or by additional sensors determining the location and orientation of the sensor platform. Usually Global Navigation Satellite System (GNSS) receiver are combined with Inertial Measurement Systems (IMS) to reach sufficient global accuracy as well as local continuity [19, 20]. Ortho-rectified images are generated by projecting the reflectance information obtained from the 3D earth surface on a 2D reference plane using the determined camera models. By this approach, spatial distortion within the images can be removed [20]. However, in close range scenarios with plants, the image

referencing relies typically on the image content instead of external sensors as the measured object cannot be assumed to be solid. Therefore, the joint coordinate system is a new concept on the leaf scale. Most of the approaches of extracting geometrical features aim at the classification of plant species based on the shape of its leaf or organs [21–23] but the generated features can be transferred to the image matching problem. Gupta et al. [24] investigated the growing characteristics of multiple species using a dense grid of ink markers on the leaves. Based on reference points on a separate reference object, camera models have been further determined for the combination of reflectance and 3D surface data of plants [25, 26]. Generally, three method groups to establish correspondence between RGB images can be identified: Point approaches [27], area/contour approaches [28, 29], and global approaches in pixel [30] or frequency space [31]. The point approaches detect relevant suitable points within the images and describe their local neighborhood by robust descriptors (e.g., Scale-invariant feature transform, SIFT [32]) allowing an assignment of points from different images. Such methods are rarely used for plant leaves (e.g., [27]) but are the standard procedure for RGB image matching for 3D reconstruction. Area and contour approaches at first extract the leaf within the image and perform an assignment based on the shape or texture characteristics of the leaf surface [29]. Yin et al. [33] used chamfer matching to perform the assignment of Arabidopsis leaves based on their shape. Bar-Sinai et al. [28] used a matching of the local graph of leaf veins to investigate the response of the leaf to mechanical stress. An approach for the multi-modal registration of RGB images and thermal images of plants based on extracted silhouettes in both image types has been developed [34]. There, a non-rigid spline model was used to match the silhouettes and generate the data for the detection of diseased plant tissue [35]. These methods for spatial image matching rely on characteristic shapes or textures. In the present case of parts of wheat leaves none of that is informative. In monocot plants the leaf veins are arranged in parallel and provide no intersections to detect. Moreover, the low spatial resolution of hyperspectral images compared to RGB images prevents the extraction of detailed surface texture information. Disease symptoms may be suitable patterns at later time points but are not present at the earlier days. The silhouette of the fixated leaf parts matches approximately a rectangle, especially for larger leaves where the leaf tip is not captured. To handle this challenge, artificial reference points of white color have been applied on the leaf surface to allow the image referencing within this study. Leaves are fixated to reduce the complexity to a 2D case

approximating the leaf surface by a horizontal 2D plane. In such a case, transformations between different image coordinate systems can be performed by 2D transformation like Affine, Similarity, or Polynomial transformation models [36]. The optimal choice depends on the required model flexibility. We introduce an approach to spatially reference multiple hyperspectral image cubes of time series experiments. These spatially referenced images form a new 4 dimensional data type with two spatial axis (x and y), one spectral axis (λ), and a fourth temporal axis (t). Within these new data type disease symptoms can easily be traced back in time, even to the point when no symptom is visible for the human eye. The referencing is performed using an algorithm robust against missing or non-stable reference points by including the RanSaC algorithms [37] and multiple 2D geometric transformations [36] in combination with a well-defined set of control points. As data, time series measurements of wheat leaves fixated in a grid frame assessed by a VISNIR hyperspectral pushbrom camera sensible in the visible (400–680 nm) and near-infrared part of the electro-magnetic spectrum (680–1000 nm) were used. Two relevant diseases of wheat with different symptom expressions were covered: Septoria tritici blotch and brown rust (Figure 1).

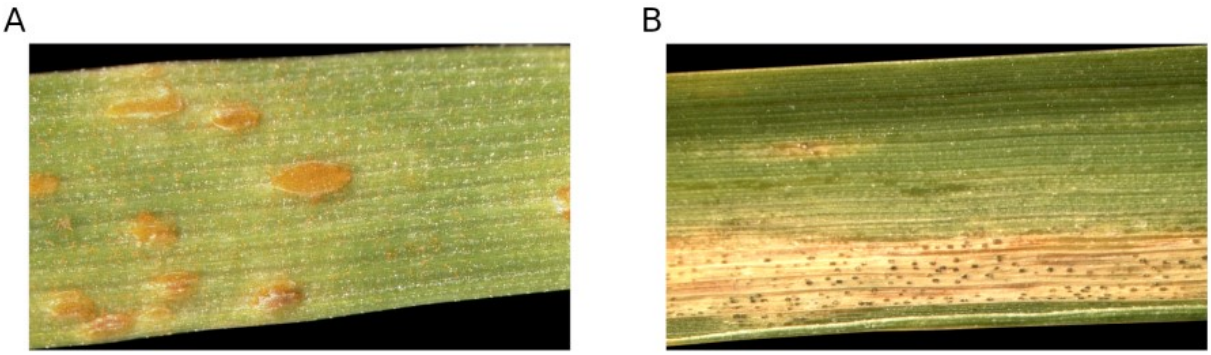

Figure 1. RGB images of the symptoms of (A) brown rust caused by *Puccinia triticina* and (B) septoria tritici blotch caused by *Zymoseptoria tritici*. Brown rust symptoms are dominated by reddish spore stocks whereas necrotic lesions are characteristic for septoria tritici blotch.

3.3 Materials and methods

Plant Material & Fungal Pathogens

Plant Material

Wheat plants (triticum aestivum), cv. Taifun and cv. Chamsin (KWS SAAT SE, Einbeck, Germany) were grown in plastic pots in substrate ED73 (Balster Erdenwerk GmbH, Sinntal-Altengronau, Germany). The plants were grown under greenhouse conditions with 22/20 ◦C day/night temperature, 60 ± 10% RH and a photoperiod of 16 h per day. Plants were inoculated after reaching BBCH growth stage 30 (sprouting) [38].

Fungal Pathogens

Inoculations of wheat plants were done with isolates of Zymoseptoria tritici and Puccinia triticina. The isolate of Z. tritici was cultured on artificial ISP2 media. As obligate biotrophic pathogen, P. triticina was maintained on living plants.

Hyperspectral Measurements

A hyperspectral line scanning spectrograph (ImSpector V10E, Spectral Imaging Ltd., Oulu, Finland), covering the VISNIR spectral range from 400–1000 nm has been used for image assessment [6]. Images had a spectral resolution of up to 2.8 nm and a spatial resolution of 0.14 mm per pixel. This results in a hyperspectral datacube with 211 bands and 1600 px per image line. A homogeneous illumination was ensured by using six ASD-Pro-Lamps (Analytical Spectral Devices Inc., Boulder, CO, USA). Camera and illumination were installed on a motorized line scanner (Spectral Imaging Ltd.). Camera settings and motor control were adapted using the SpectralCube software (Version 3.62, 2000, Spectral Imaging Ltd.). Leaves have been horizontally fixed in a tray using strings allowing imaging of around 20 cm of each leaf. Multiple leaves have been placed side by side within a single image. White color spots are applied as reference points on the leaves to allow image referencing. As shown in Figure 2, six spots in two rows are applied to each leaf section of approximately 4 cm. Observing five leaf sections limited by the fixating strings results in 30 white color spots on each leaf. As background material, blue cardboard has been selected as it supports background segmentation. For brown rust, time series measurements from 2 to 12 days after inoculation (dai) have been captured. Contrarily, for septoria tritici blotch 15 to 27 dai were covered due to the deviating process of pathogenesis. The data has been normalized, i.e., reflectance was

calculated relative to a barium sulphate white reference (Spectral Imaging Ltd.) and a dark current measurement. Normalization has been performed following [39] using ENVI 4.6 + IDL 7.0 (EXELIS Visual Information Solutions, Boulder, CO, USA).

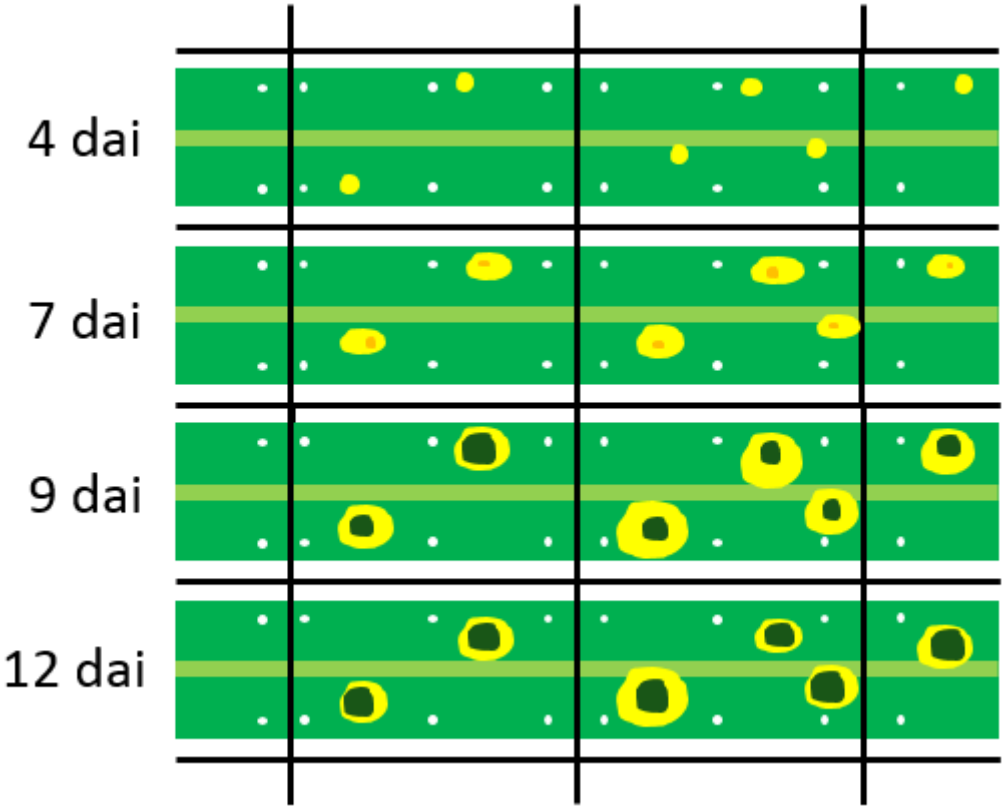

Figure 2. Scheme of the referenced hyperspectral time series of a single leaf observed at four exemplary days. Reference points (white spots), fixating strings (in black), and the developing disease symptoms are included.

Algorithm for Hyperspectral Image Referencing

The proposed algorithm is divided into four steps: 1. background segmentation, 2. reference point detection, 3. matching of reference points, and 4. the spatial transformation (Figure 3).

Background Segmentation

The background segmentation relies on the classification method Random Forest algorithm [40] to separate leaf regions and background. The model was trained by manual annotation of a single hyperspectral image. As training data 1000 pixels of the blue background, 1000 pixels of healthy leaf tissue, 1000 pixels of chlorotic leaf tissue, and 500 pixels of spore stocks were randomly sampled from the annotation in which the human expert has tried to represent the class variability. Remaining artifacts of misclassified pixels causing very small regions and

holes within large regions were corrected using connected components approach. Leaf regions were extracted and identified by corresponding leaf number based on the position within the image.

Reference Point Extraction

For the selection of the reference points, the Random Forest algorithm was applied as well. By manual annotation 100 pixels of the white reference points and 1000 pixels of plant material (balanced mixture of healthy, chlorotic, and spore stock tissue) were selected and used to train the model. Classified regions within a size range of 3 to 40 pixels were regarded and the center of gravity was extracted as the pixel position. To exclude mixed pixels, the reference point region has been extended by 3 pixels and removed from the leaf regions.

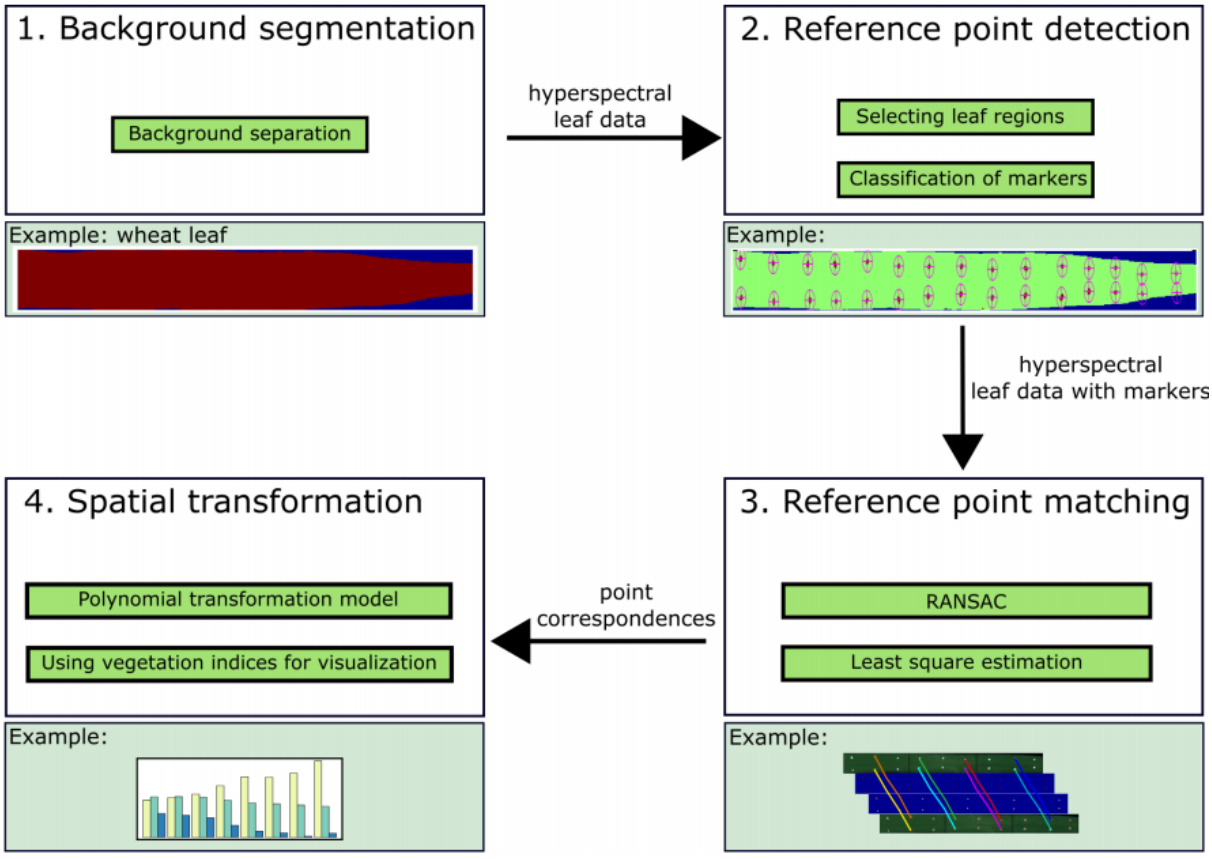

Figure 3. Dataflow of the proposed algorithm for geometric referencing of hyperspectral images.

Assignment of Reference Points

Point correspondence was used to derive the geometric transformation model between two images of a leaf recorded at different observation days. Following, the assignment of single reference points between the different observation dates is a prerequisite for image transformation. In our approach, the Random Sample Consensus (RanSaC) algorithm [37]

determines a preliminary nonreflective similarity transformation by assigning two random reference points in the base image to two random points in the image to reference. The models were evaluated by projecting each reference point of the origin image to the target image and assess the distance to the closest reference points of the target image. Reference points within a distance of 20 px are assumed to be correct and, therefore, support the model. By repeating this process and selecting the transformation model with the maximum number of supporting reference points, a preliminary referencing was performed. Using nearest neighbor assignment with a distance threshold of 20 px, reference points were assigned and reference points without counterpart were excluded from the further process.

Spatial Image Transformation Models

A transformation model was derived using the corresponding reference points. It is used to reference all images of a time series to the first observation day. The type and flexibility need to be adapted to the specific task. We compared different transformation types [36]: Nonreflective Similarity, Affine, Projective, Polynomial, and Local Weighted Mean (LWM). Nonreflective Similarity transformation is defined by rotation, translation, and scaling. Adding a shearing parameter and another scale factor results in an affine transformation. The Projective transformation represents a central-projective transformation between the two image coordinate systems and is defined by eight coefficients [36]. The Polynomial model relates the coordinates within the two images by a mathematical description based on two 2D polynomials. We selected polynomials of order 3 as they are able to represent the assumed leaf movements. The LWM model differs from the mentioned transformation due to its local character. The image is divided into regions in which a local polynomial transformation model is applied [41]. All steps of the algorithm have been performed using Matlab 2013a (The Mathworks, Natick, MA, USA) and the corresponding Image Processing Toolbox.

Evaluation of Transformation Accuracy

Evaluation of the transformation accuracy was performed by the Root Mean Square Error (RMSE) on Euclidean deviations of n reference points

$$RMSE = \sqrt{\frac{\sum_i \sqrt{(x_i - x_{ref})^2 + (y_i - y_{ref})^2}^2}{n}}. \quad (1)$$

To evaluate the transformation quality, assessing the mean accuracy of projected reference points is not sufficient. Large distortions or missing image information can occur in parts of the leaf without affecting the RMSE parameter. Therefore, two further quality parameters were introduced: Stability and Extrapolation. The first is defined as the RMSE of an inner point, if it is not included into the transformation model. This approximates the transformation quality of arbitrary points of the leaf. The extrapolation parameter approximates the transformation quality at the leaf border by the transformation accuracy of the four outer points point in the first and last point columns at the leaf base and the leaf tip (cv. Figure 2). The evaluation has been performed on the full time series (11 images) of a representative leaf showing brown rust symptoms. For the accuracy measurement 11 × 30 = 330, for the extrapolation 11 × 4 = 44, and for the stability 11 × 5 = 55 reference points have been used. The hold out reference points for stability calculation have been evenly distributed within the inner points.

Vegetation Indices

For characterization of the spectral development of symptomatic areas, Vegetation Indices based on selected spectral bands (λi) have been used. The Normalized Difference Vegetation Index (NDVI) uses a combination of a red band (670 nm) and a NIR band (800 nm) according to formula 2 to extract information about plant vitality and Chlorophyll content [10]. In addition, the Photochemical Reflectance Index (PRI) was calculated, using the difference between two bands in the green color range (531 nm and 570 nm) [42] as well as the Anthocyanin Reflectance Index (ARI) that uses a green (550 nm) and a NIR (700 nm) band which is sensitive to changes in carotenoid pigments [43].

$$NDVI = \frac{\lambda_{670} - \lambda_{800}}{\lambda_{670} + \lambda_{800}} \quad (2)$$

$$PRI = \frac{\lambda_{531} - \lambda_{570}}{\lambda_{531} + \lambda_{570}} \quad (3)$$

$$ARI = \frac{1}{\lambda_{550}} - \frac{1}{\lambda_{700}} \quad (4)$$

The selected Vegetation Indices are correlated to different plant-physiological parameters (chlorophyll content, photochemical activity, anthocyanin content) which are significantly influenced during disease development.

Presymptomatic Labeling

To demonstrate the advantages of a fully referenced data set, we used spatial referencing to move the border of symptoms that can be annotated retrospectively regarding the infection time. At first a supervised classification model (Random Forest algorithm [40]) has been derived on the full spectral information based on manual annotations of vital plant material, chlorotic regions, and spore stocks of brown rust (training data composition given in Section 2.3.1). Such models reproduce the visual annotation with good accuracy but are not able to detect invisible effect. Here, spectra of pixels that were two days later detected as diseased were include in the training data and the Random Forest model is retrained. Furthermore, only pixels were included that are observed at every observation day to guarantee continuous time series observation for every point on the leaf surface within the data set. The extended annotations are used to retrain the classification model.

3.4 Results

This section presents the obtained results of the spatial referencing algorithm for hyperspectral images and the proposed applications tracing of symptoms and advanced labeling. The referencing approach has been applied to time series observations of two different diseases: Septoria tritici blotch and brown rust, each represented by twelve leaves. Figure 4 shows the effect of referencing by the RGB visualization of hyperspectral images showing a progressing brown rust infection 2–12 dai.

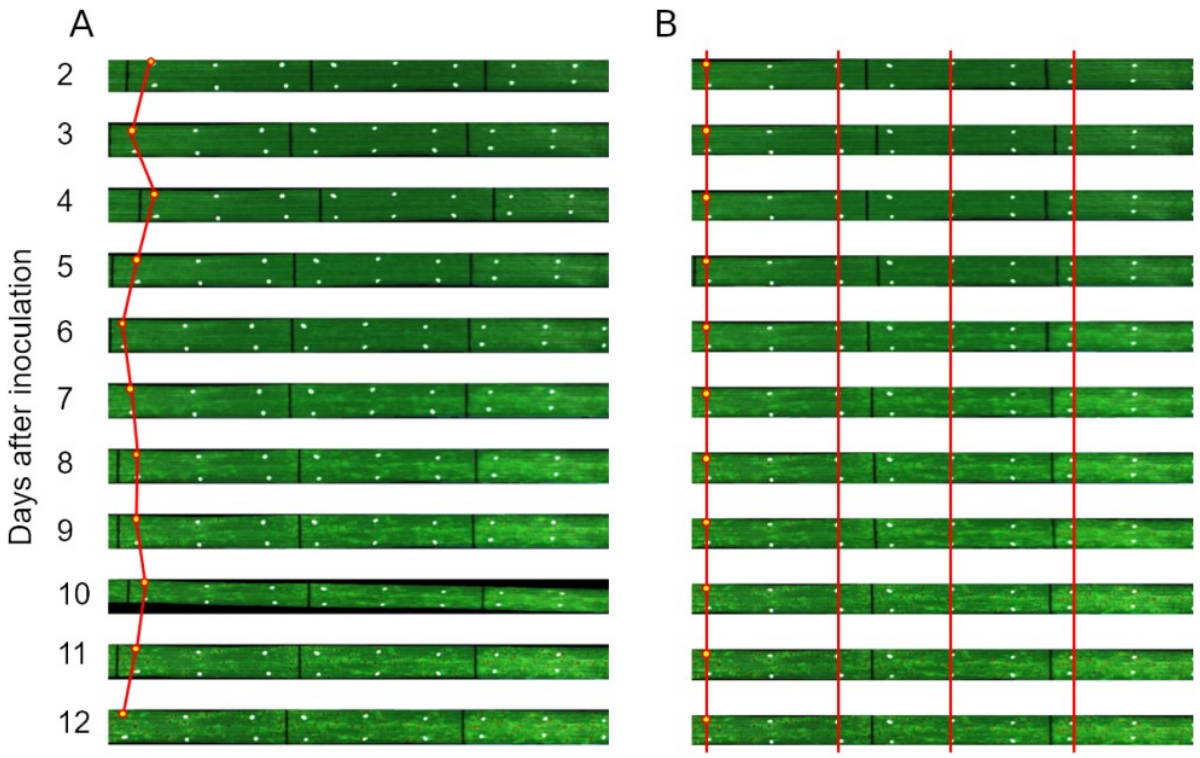

Figure 4. Effect of the spatial referencing. (A) shows the time series of unaligned hyperspectral images and (B) the same time series after the application of the proposed algorithm. To illustrate the result, identical points within the images were connected by red lines.

Figure 5 shows the results of tracing mature symptoms back in time. For brown rust and septoria tritici blotch, a continuous transition starting from healthy tissue has been extracted. The final state represents the deviating symptom appearance of the diseases (cv. Figure 1).

Background Segmentation and Reference Point Detection

Parts of the algorithm are common and well understood steps in many image analysis pipelines. 1. background segmentation and 2. reference point detection did not limit the accuracy or performance of the algorithm. The used Random Forest classifier was trained on manually annotated but representative training data and reached on this data an accuracy of more than 99%. The derived class images “background vs. leaf” and “leaf vs. reference point” showed a high level of concordance with the visual impression. In transfer regions, e.g., the unsharp transition of leaf tissue to the white color of the reference points, a true region boundary is not defined. Consequences are neglectable as the center of gravity of the reference point region showed a high level of reproducibility within the different images.

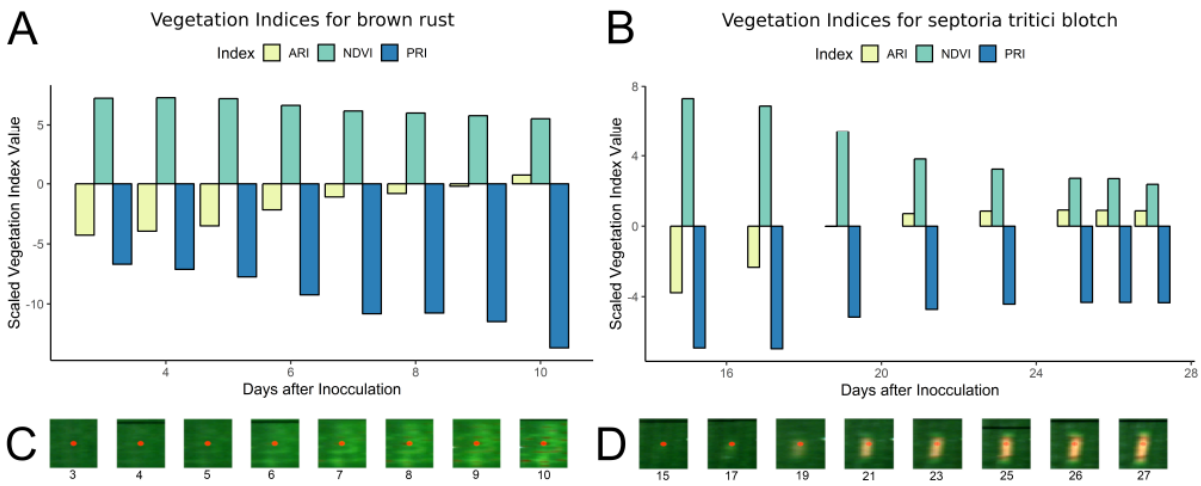

Figure 5. Visualization of the tracing results by using RGB visualizations of a symptom and the corresponding Vegetation indices anthocyanin reflectance index (ARI), normalized difference vegetation index (NDVI), and photochemical reflectance index (PRI) for brown rust (A, C) and septoria tritici blotch (B, D). For visualization purposes the NDVI was multiplied by 10 and the PRI by 40. Time series of spectral characteristics are derived to uncover the deviating spectral dynamics of the diseases.

In contrast, the matching of the reference points to the base image of day 1 is challenging if larger movement had occurred or missing points complicate the assignment process. The RanSaC algorithm determines a preliminary non-reflective similarity transformation and allows a nearest neighbor assignment. More flexible transformations tend to degenerated cases assigning multiple reference point to a single base point. Using the RanSaC with 10,000 iterations, an optimum has been found in each case, whereas using only 1000 iteration led to a suboptimal result in around 10% of the runs.

Transformation Model

The flexibility and robustness of a transformation model type determines the suitability of the model for a specific task. Average quality parameters of the different models for the full time series of a representative leaf of the brown rust data set are given in Table 1.

The extracted quality parameters indicate advantages of using transformation functions with higher flexibility and more model parameters. In each of the three performance parameters accuracy, stability, and extrapolation, the LWM transformations reached the lowest error rates whereas Similarity and Affine transformation obtained the highest error rates.

Table 1. Performance parameters (accuracy, stability, and extrapolation) of the five transformation model types assessing the suitability for the spatial referencing of wheat leaves. The accuracy is measured by the reprojection error of used reference points. The stability is measured by the reproduction error of unused control points within the leaf and the ability to extrapolate is measured by the root mean square error (RMSE) of unused control points at the base and the tip of the leaf. Displayed are the mean results during the whole time series of eleven days (standard deviation in brackets).

	Similarity	Affine	Projective	Polynomial	LWM
Accuracy (px)	1.24 (0.75)	1.23 (0.76)	1.09 (0.75)	0.26 (0.092)	0.19 (0.07)
Stability (px)	1.06 (0.62)	1.08 (0.61)	0.97 (0.60)	0.47 (0.17)	0.36 (0.15)
Extrapolation (px)	2.61 (1.57)	2.61 (1.59)	2.37 (1.59)	0.83 (0.31)	0.76 (0.30)

Presymptomatic Labeling

The effect of the extended labeling is shown in Figure 6. The manual annotation allows to detect the spore stocks with good accordance with the visual impression. The highly chlorotic tissue at the later observation data was also selected whereas the transition areas to the vital plant tissue is mostly assigned to the healthy class. The extended labelling allows to move this border between vital and chlorotic tissue. The transition areas are now separated from the vital area and regions showing no visual symptoms are detected. Non-continuously observed points of the leaf surface were excluded causing that the covered area by the fixation strings are widened as it is summed up for each day.

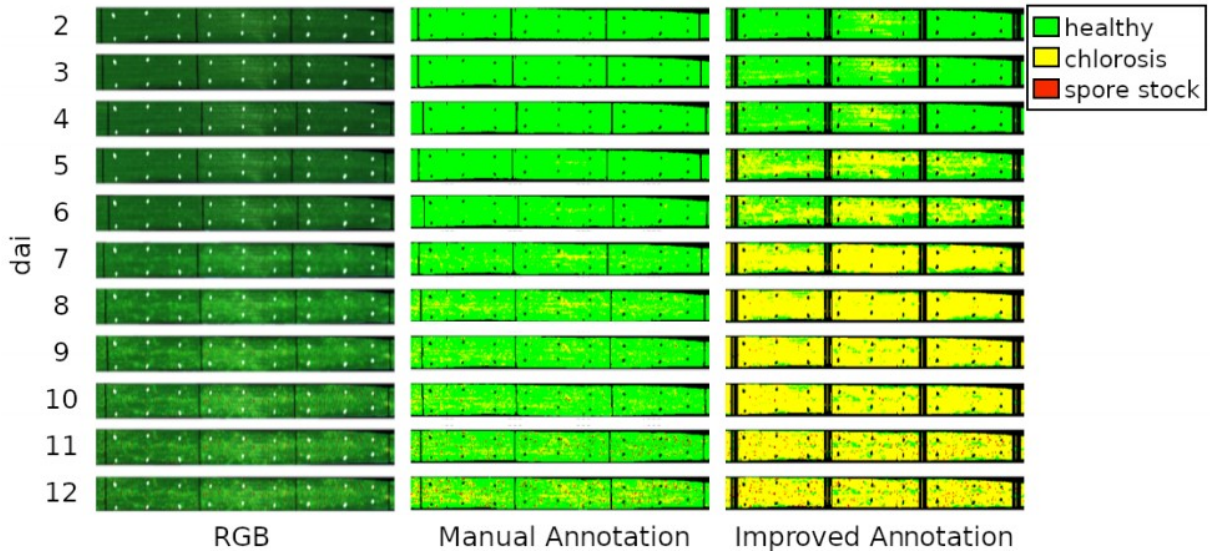

Figure 6. RGB visualization and corresponding classification results of a brown rust time series. Compared are the classification results based on a manual annotation and an improved annotation including the data two days before detection.

3.5 Discussion

The results show that automated referencing of hyperspectral images is possible. The shown approach enables the tracking of spatial symptoms regarding size and reflection in particular for the spectral area between 400–1000 nm. Furthermore, tracking of the spectral characteristics of diseases over time gives new insights for a biological interpretation and an improved detection. This has been shown for brown rust for periods between 2–10 days after inoculation and for 15–30 days for septoria tritici blotch (Figure 5). The time series uncover similarities as well as differences within the type of effect and its dynamics. For both diseases the NDVI is reduced and the ARI increased indicating the degradation of chlorophylls and the production of anthocyanins, but the change by septoria tritici blotch is much sharper. The PRI shows contrary effects if the two disease: Brown rust induces a decrease whereas septoria tritici blotch induces an increase. PRI is related to the photochemical activity meaning the productivity of photosynthesis [42]. This is surprising as the brown rust permits vital leaf tissue whereas septoria tritici blotch causes necrotic tissue. Such response may be explained by the pigments of the produced brown rust spores interfering with the used bands of PRI [44]. The extended labeling showed high potential to train machine learning models with higher sensitivity even in very early symptom stages (Figure 6). To the best of our knowledge, this is a new approach in hyperspectral close range imaging. In non-imaging setups the early symptoms have been classified [45]. In such scenario a spatial referencing is not required, however, this neglects the high sensitivity for small scale symptoms [6].

Conditions for tracing are proper measurement setup and suitable background material allowing a clear background separation. The background material has to differ significantly from the plant material, wilted leaves, reference points, and disease symptoms. The selected blue paper material fulfills these demands. Minor errors occur at reflecting metal edges of the tray but these can be filtered out by a minimal region size. Same applies for the reference points. They need to be durable enough over the experimental period and, furthermore, need to differ significantly from plant material, wilted leaves, and disease symptoms. Critical parts include the selection of the transformation model as it is always a compromise between robustness and accuracy. The LWM model provides the highest accuracy (Table 1). Nevertheless, the Polynomial transformation model was selected as it reached very similar results compared to the LWM model which tends to produce distorted image areas due to its local character. As local transformation models depend always on a small part of the

information, they are less stable but have the ability to represent also local changes due to wilting. In the present data set, the resulting distortions and twisting effects could not be represented by any of the models. Advantages of the local model were therefore very rare whereas negative effects occur much more frequent especially at the leaf borders. One disadvantage of the showed method is the use of markers on the leaf tissue. Effects of the marker material on the underlying leaf tissue cannot be completely excluded as well as a possible change of the disease development. However, differences were not observed between marked leaves and unmarked control plants. Limitations for the method are given by the size of the reference points. Using the shortwave-infrared camera (1000–2500 nm; Specim Spectral Imaging Ltd., Oulu, Finland) of the measurement platform, it was not possible to detect them with the required accuracy. The spatial resolution of the shortwave-infrared camera is by a factor of 10 lower than the spatial resolution of the VISNIR camera [25]. Upcoming hyperspectral cameras may be able to allow the spectral referencing also within different spectral regions. Further research will focus on the use of interest operators on image data as they are used for motion tracking. In particular, the use of the SIFT [32] operator for tracking within RGB Image sequences could be an applicable alternative. This could be adapted to the needs of hyperspectral image sequences using different bands and their spectral relation. Spatial tracking of markers is a key capability for transferring the findings of the shown experiments to the high throughput greenhouse scale (e.g., [46]). Tracking is needed due to leaf movement (external) and plant growth (internal) which leads to a complex transformation of the complete plant. At the moment, the method is limited to 2D leaves due to the integrated geometrical transformations. Even since the data fusion of hyperspectral images and 3D models is possible [25, 26], the referencing has many more degrees of freedom. Changes in the shape of the leaf over time has to be represented within the transformation model having the potential to result in a runaway model complexity. Furthermore, reference points within the 3D model has to be selected, described (e.g., by RIFT descriptor [47]), and assigned to image locations. However, extensive studies are required to represent leaf growing and leaf movements by a compact and applicable model. Modelling the complete development of not only geometry, but also nutrient supply and changes in reflectance is possible when using L-Systems [48] or FSP models (FSPM–functional-structural-plant-models) [49] which use substitution in a grammar structure to model the plant development. By this,

the continuous geometric referencing of hyperspectral images provides valuable input data for modelling plant growing and development.

3.6 Conclusion

This publication introduces a method for referencing of hyperspectral images. Field of application is the improved tracking of hyperspectral information of disease symptoms and their development over time. Results have been shown for symptoms and their development of septoria tritici blotch and brown rust, using a VISNIR camera measuring between 400 and 1000 nm. The potential of the method has been demonstrated by extracting the dynamic of spectral indices of a single symptom over time. Furthermore, the possibility to annotate invisible symptoms by tracing visible symptoms back in time to the invisible phase of pathogenesis. The concept of spectral tracking over time can contribute to a more dynamic research of disease development instead of focusing to mature symptoms and their appearing in the visible bands.

3.7 Acknowledgements

This work was financially supported by BASF Digital Farming. We acknowledge the detailed and constructive remarks of the reviewers.

3.8 References

1. Mahlein, A.K.; Kuska, M.; Behmann, J.; Polder, G.; Walter, A. Hyperspectral sensors and imaging technologies in phytopathology: State of the art. *Annu. Rev. Phytopathol.* **2018**, *56*, 535–558.
2. Blackburn, G.A. Hyperspectral remote sensing of plant pigments. *J. Exp. Bot.* **2006**, *58*, 855–867
3. Bock, C.; Poole, G.; Parker, P.; Gottwald, T. Plant disease severity estimated visually, by digital photography and image analysis, and by hyperspectral imaging. *Crit. Rev. Plant Sci.* **2010**, *29*, 59-107.
4. Mahlein, A.K. Plant disease detection by imaging sensors–parallels and specific demands for precision agriculture and plant phenotyping. *Plant Dis.* **2016**, *100*, 241–251.
5. Kuska, M.; Wahabzada, M.; Leucker, M.; Dehne, H.W.; Kersting, K.; Oerke, E.C.; Steiner, U.; Mahlein, A.K. Hyperspectral phenotyping on the microscopic scale: Towards automated characterization of plant-pathogen interactions. Plant Methods **2015**, 11, 28.
6. Mahlein, A.K.; Rumpf, T.; Welke, P.; Dehne, H.W.; Plümer, L.; Steiner, U.; Oerke, E.C. Development of spectral indices for detecting and identifying plant diseases. *Remote Sens. Environ.* **2013**, *128*, 21–30.
7. Aasen, H.; Burkart, A.; Bolten, A.; Bareth, G. Generating 3D hyperspectral information with lightweight UAV snapshot cameras for vegetation monitoring: From camera

calibration to quality assurance. *ISPRS J. Photogramm. Remote Sens.* **2015**, *108*, 245–259.
8. Honkavaara, E.; Rosnell, T.; Oliveira, R.; Tommaselli, A. Band registration of tuneable frame format hyperspectral UAV imagers in complex scenes. *ISPRS J. Photogramm. Remote Sens.* **2017**, *134*, 96–109.
9. Burkart, A.; Aasen, H.; Alonso, L.; Menz, G.; Bareth, G.; Rascher, U. Angular dependency of hyperspectral measurements over wheat characterized by a novel UAV based goniometer. *Remote Sens.* **2015**, *7*, 725–746.
10. Rouse, J., Jr.; Haas, R.; Schell, J.; Deering, D. Monitoring vegetation systems in the Great Plains with ERTS. *In Proceedings of the Third Earth Resources Technology Satellite-1 Symposium*, Washington, DC, USA, 10–14 December **1973**.
11. Bockus, W. W.; Bowden, R.; Hunger, R.; Murray, T.; Smiley, R. Compendium of Wheat Diseases and Pests, 3rd ed.; American Phytopathological Society (APS Press): Sao Paulo, MN, USA, 2010. Camargo, A.; Smith, J. An image-processing based algorithm to automatically identify plant disease visual symptoms. *Biosyst. Eng.* **2009**, *102*, 9–21.
13. West, J.S.; Bravo, C.; Oberti, R.; Lemaire, D.; Moshou, D.; McCartney, H.A. The potential of optical canopy measurement for targeted control of field crop diseases. *Annu. Rev. Phytopathol.* **2003**, *41*, 593–614.
14. Bravo, C.; Moshou, D.; West, J.; McCartney, A.; Ramon, H. Early Disease Detection in Wheat Fields using Spectral Reflectance. *Biosyst. Eng.* **2003**, *84*, 137–145.
15. Behmann, J.; Mahlein, A.K.; Rumpf, T.; Römer, C.; Plümer, L. A review of advanced machine learning methods for the detection of biotic stress in precision crop protection. *Precis. Agric.* **2015**, *16*, 239–260.
16. Hartley, R.; Zisserman, A. Multiple View Geometry in Computer Vision; *Cambridge University Press:* Cambridge, UK, **2003**.
17. Zitova, B.; Flusser, J. Image registration methods: A survey. *Image Vis. Comput.* **2003**, *21*, 977–1000.
18. Salvi, J.; Matabosch, C.; Fofi, D.; Forest, J. A review of recent range image registration methods with accuracy evaluation. *Image Vis. Comput*. **2007**, *25*, 578–596.
19. Eling, C.; Klingbeil, L.; Kuhlmann, H. Real-time single-frequency GPS/MEMS-IMU attitude determination of lightweight UAVs. *Sensors* **2015**, *15*, 26212–26235.
20. Toutin, T. Geometric processing of remote sensing images: Models, algorithms and methods. *Int. J. Remote Sens.* **2004**, *25*, 1893–1924.
21. Gwo, C.Y.; Wei, C.H. Plant identification through images: Using feature extraction of key points on leaf contours1. *Appl. Plant Sci.* **2013**, *1*, 1200005.
22. Mouine, S.; Yahiaoui, I.; Verroust-Blondet, A. Combining leaf salient points and leaf contour descriptions for plant species recognition. In Proceedings of the International Conference Image Analysis and Recognition, Povoa do Varzim, Portugal, 26–28 June 2013; Springer: Berlin, Germany, **2013**; pp. 205–214.
23. Kolivand, H.; Fern, B.M.; Rahim, M.S.M.; Sulong, G.; Baker, T.; Tully, D. An expert botanical feature extraction technique based on phenetic features for identifying plant species. *PLoS ONE* **2018**, *13*, e0191447.
24. Gupta, M.D.; Nath, U. Divergence in patterns of leaf growth polarity is associated with the expression divergence of miR396. *Plant Cell* **2015**.
25. Behmann, J.; Mahlein, A.K.; Paulus, S.; Kuhlmann, H.; Oerke, E.C.; Plümer, L. Calibration of hyperspectral close-range pushbroom cameras for plant phenotyping. *ISPRS J. Photogramm. Remote Sens.* **2015**, *106*, 172–182.

26. Behmann, J.; Mahlein, A.K.; Paulus, S.; Dupuis, J.; Kuhlmann, H.; Oerke, E.C.; Plümer, L. Generation and application of hyperspectral 3D plant models: Methods and challenges. *Mach. Vis. Appl.* **2016**, *27*, 611–624.
27. De Vylder, J.; Douterloigne, K.; Vandenbussche, F.; Van Der Straeten, D.; Philips, W. A non-rigid registration method for multispectral imaging of plants. In Proceedings of the 2012 SPIE Defense, Security, and Sensing, Baltimore, MD, USA, 23–27 April 2012; Volume 8369, p. 836907.
28. Bar-Sinai, Y.; Julien, J.D.; Sharon, E.; Armon, S.; Nakayama, N.; Adda-Bedia, M.; Boudaoud, A. Mechanical stress induces remodeling of vascular networks in growing leaves. *PLoS Comput. Boil.* **2016**, *12*, e1004819.
29. Balduzzi, M.; Binder, B.M.; Bucksch, A.; Chang, C.; Hong, L.; Iyer-Pascuzzi, A.S.; Pradal, C.; Sparks, E.E. Reshaping plant biology: Qualitative and quantitative descriptors for plant morphology. Front. Plant Sci. **2017**, 8, 117.
30. Wang, X.; Yang,W.;Wheaton, A.; Cooley, N.; Moran, B. Efficient registration of optical and IR images for automatic plant water stress assessment. Comput. Electron. Agric. **2010**, 74, 230–237.
31. Henke, M.; Junker, A.; Neumann, K.; Altmann, T.; Gladilin, E. Automated alignment of multi-modal plant images using integrative phase correlation approach. *Front. Plant Sci.* **2018**, *9*, 1519.
32. Lowe, D.G. Distinctive image features from scale-invariant keypoints. *Int. J. Comput. Vis.* **2004**, *60*, 91–110, doi:10.1023/b:visi.0000029664.99615.94.
33. Yin, X.; Liu, X.; Chen, J.; Kramer, D.M.; others. Multi-leaf alignment from fluorescence plant images. In Proceedings of the IEEE 2014 IEEE Winter Conference on Applications of Computer Vision (WACV), Steamboat Springs, CO, USA, 24–26 March 2014; pp. 437–444.
34. Raza, S.E.A.; Sanchez, V.; Prince, G.; Clarkson, J.P.; Rajpoot, N.M. Registration of thermal and visible light images of diseased plants using silhouette extraction in the wavelet domain. *Pattern Recognit.* **2015**, *48*, 2119–2128.
35. Raza, S.E.A.; Prince, G.; Clarkson, J.P.; Rajpoot, N.M. Automatic detection of diseased tomato plants using thermal and stereo visible light images. *PLoS ONE* **2015**, *10*, e0123262.
36. Luhmann, T.; Robson, S.; Kyle, S.; Harley, I. *Close Range Photogrammetry: Principles, Techniques and Applications;* Whittles: Dunbeath, UK, 2006.
37. Fischler, M.A.; Bolles, R.C. Random sample consensus: A paradigm for model fitting with applications to image analysis and automated cartography. Commun. ACM **1981**, 24, 381–395.
38. Meier, U. *Growth Stages of Mono-and Dicotyledonous Plants*; Blackwell, Wissenschafts-Verlag: Berlin, Germany, 1997.
39. Grahn, H.; Geladi, P. *Techniques and Applications of Hyperspectral Image Analysis*; JohnWiley Sons: Hoboken, NJ, USA, 2007.
40. Breiman, L. Random forests. *Mach. Learn.* **2001**, *45*, 5–32.
41. Goshtasby, A. Image registration by local approximation methods. *Image Vis. Comput.* **1988**, *6*, 255–261.
42. Gamon, J.; Penuelas, J.; Field, C. A narrow-waveband spectral index that tracks diurnal changes in photosynthetic efficiency. *Remote Sens. Environ.* **1992**, *41*, 35–44.
43. Gitelson, A.A.; Merzlyak,M.N.; Chivkunova, O.B. Optical properties and nondestructive estimation of anthocyanin content in plant leaves. *Photochem. Photobiol.* **2001**, *74*, 38.

44. Wang, E.; Dong, C.; Park, R.F.; Roberts, T.H. Carotenoid pigments in rust fungi: Extraction, separation, quantification and characterisation. *Fungal Boil. Rev.* **2018**, *32*, 166–180.
45. Rumpf, T.; Mahlein, A.K.; Steiner, U.; Oerke, E.C.; Dehne, H.W.; Plümer, L. Early detection and classification of plant diseases with Support Vector Machines based on hyperspectral reflectance. *Comput. Electron. Agric.* **2010**, *74*, 91–99.
46. Kuska, M.T.; Behmann, J.; Grosskinsky, D.K.; Roitsch, T.; Mahlein, A.K. Screening of barley resistance against powdery mildew by simultaneous high-throughput enzyme activity signature profiling and multispectral imaging. *Front. Plant Sci.* **2018**, *9*, 1074.
47. Lazebnik, S.; Schmid, C.; Ponce, J. A sparse texture representation using local affine regions. IEEE Trans. *Pattern Anal. Mach. Intell.* **2005**, *27*, 1265–1278.
48. Prusinkiewicz, P.; Lindenmayer, A. *The Algorithmic Beauty of Plants*; Springer: Berlin/Heidelberg, Germany, 1996.
49. Vos, J.; Evers, J.B.; Buck-Sorlin, G.H.; Andrieu, B.; Chelle, M.; de Visser, P.H.B. Functional-structural plant modelling: A new versatile tool in crop science. *J. Exp. Bot.* **2009**, *61*, 2101–2115, doi:10.1093/jxb/erp345.

4 Hyperspectral signal decomposition and symptom detection of wheat rust disease at the leaf scale using pure fungal spore spectra as reference

This work has been published as:

Bohnenkamp, D., Kuska, M. T., Mahlein, A. K., & Behmann, J. (2019). Hyperspectral signal decomposition and symptom detection of wheat rust disease at the leaf scale using pure fungal spore spectra as reference. *Plant Pathology*, *68*(6), 1188-1195.

David Bohnenkamp conceived the experiments (50%), DB performed the measurements (100%), DB preprocessed and analyzed the data (50%), DB wrote the paper (50%).

Text was not modified from the published version.

4.1 Abstract

This study establishes a method to detect and distinguish between brown rust and yellow rust on wheat leaves based on hyperspectral imaging at the leaf scale under controlled laboratory conditions. A major problem at this scale is the generation of representative and correctly labelled training data, as only mixed spectra comprising plant and fungal material are observed. For this purpose, the pure spectra of rust spores of *Puccinia triticina* and *P. striiformis*, causal agents of brown and yellow rust, respectively, were used to serve as a spectral fingerprint for the detection of a specific leaf rust disease. A least-squares factorization was used on hyperspectral images to unveil the presence of the spectral signal of rust spores in mixed spectra on wheat leaves. A quantification of yellow and brown rust, chlorosis and healthy tissue was verified in time series experiments on inoculated plants. The detection of fungal crop diseases by hyperspectral imaging was enabled without pixel-wise labelling at the leaf scale by using reference spectra from spore scale observations. For the first time, this study shows an interpretable decomposition of the spectral reflectance mixture during pathogenesis. This novel approach will support a more sophisticated and precise detection of foliar diseases of wheat by hyperspectral imaging.

4.2 Introduction

Mixed signals are a frequent issue in remote sensing applications, where each pixel within satellite imagery captures many square metres of the Earth's surface. As a result, the recorded signal is a combination of all objects weighted by their spatial proportion. This problem is

frequently addressed by 'endmember unmixing methods' (Dennison & Roberts, 2003). Similar effects occur also in close range imaging and hyperspectral microscopy, which both have a higher spatial resolution (Mahlein *et al.*, 2012; Behmann *et al.*, 2014; Kuska *et al.*, 2015, 2017). Here, the mixing is not primarily due to the large pixel area, but is significant in the vertical domain. The high level of transmittance of thin fungal tissue, and therefore lower reflection intensities, in combination with the strong reflectance of plant tissue layers, generates a combined signal with regard to the height component (Fig. 1). The reflectance of these diseased plant leaves is changed to certain spectral shifts according to the fungal development in the host tissue. As a consequence of the potential application for detecting plant diseases, hyper-/multispectral sensors have aroused the interest and expectation of the public, farmers and companies as sophisticated optical sensors in agriculture that may support deeper insights into plant physiology and sustainable plant protection measures, as well as for improvements in the phenotyping process in crop resistance breeding (Jay *et al*., 2016; Mahlein, 2016; Mishra *et al*., 2017; Asaari *et al*., 2018; Kuska *& Mahlein* 2018; Mahlein *et al*., 2018).

To contribute to sustainable management practice in agriculture, the precise detection of primary infection sites and disease dynamics is fundamental. An example of a current practical reference is the increasing global spread of rust diseases and the overcoming of effective crop resistances (Torriani *et al.*, 2015). Rust diseases are widespread and highly host-specific (Dracatos *et al.*, 2018), and rust fungi are obligate biotrophic pathogens (Mendgen & Hahn, 2002). The pigmentation of rust spores is due to the presence of carotenoids (Hennessy & Sackston, 1972). Four different types of carotenoids have been found in rust fungi, with *γ*- and β-carotenes appearing in most species (Smits & Mitchell, 1951). However, carotenoid composition between different rust species varies greatly (Zwetko & Pfeifhofer, 1991). It is assumed that carotenoids play a protective role against UV radiation and oxidative stress, and could act as virulence factors (Butler & Day, 1998; Avalos & Carmen Limón, 2015). The colour of rust spores is correlated to the content and composition of these carotenoids, which are located in the cell wall and as lipid droplets in the cytoplasm (Hennesy & Sackston, 1972; Wang *et al.*, 2018). In the case of yellow rust and brown rust, differences in the pigmentation due to carotenoids can be observed by the naked eye. However, even with the application of hyperspectral imaging, the measured signal from fully developed uredinia is still a mixture of the spore spectra and the underlying leaf spectra (Wahabzada *et al.*, 2016). The changing

weights of these components increases the complexity of identification. Often training data capturing the variability within the specific dataset are used to define the class border between healthy and diseased leaf tissue (Behmann *et al.*, 2015). However, the training data are also composed of mixed signals, which can cause an increase in complexity of annotation and may affect the quality of the data. As a result, such models are limited to a specific data set or measurement setup. This means that a model requires new training data in order to be transferred to new datasets (Thomas *et al.*, 2018).

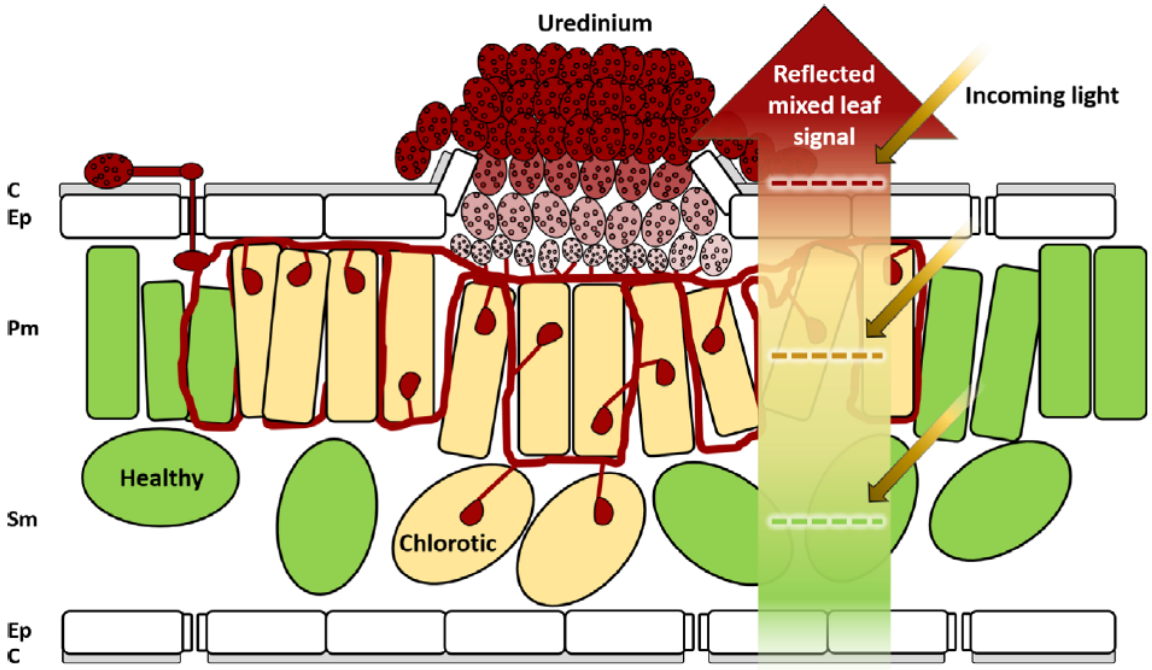

Figure 1 Schematic cross section of a wheat leaf infected with brown rust and the different leaf layers. The leaf is divided into cuticle (C), epidermis (Ep), palisade mesophyll (Pm) and spongy mesophyll (Sm). The arrows indicate the incoming light and the reflected mixed signal of the leaf, which is affected by properties of the different leaf layers and fungal activity within the tissues and on the leaf surface.

In scenarios with mixed signals of a limited number of influencing factors, different kinds of matrix decomposition or matrix factorization are widely applied (Pauca *et al*., 2006). Typically, the data matrix is factorized into the latent variables and weights/loadings, e.g. by principal component analysis (PCA; Wold, 1987), simplex volume maximization (SiVM; Thurau *et al*., 2010) or multivariate curve resolution (Tauler *et al*., 1995). All of these methods include different optimization functions, constraints and different ways of interpreting the results. PCA conserves a maximum of variance, SiMV selects extreme data points on the approximated convex hull, and multivariate curve resolution focuses on a physically plausible model by

additional constraints based on prior knowledge. The present study does not use factor spectra derived from the data for analysis, but relies on the use of pure spectra.

To improve and specify hyperspectral data and to overcome the inaccuracy of mixed signals, a method has been established that allows measurement of the pure spectra of rust spores. These reference spectra can be integrated into a non-negative least-squares factorization, unveiling the composition of the incoming signal spectra. By the summed weights of spore spectra, *Puccinia triticina* and *P. striiformis*, causal agents of brown and yellow rust of wheat, respectively, can be distinguished. Using pure fungal spectra for detection of plant diseases on plant leaves is a new approach in plant pathology and might enable development of disease detection models with a minimum of annotated training data. The spectral signal is decomposed into known factors instead of using a classifier assigning a specific disease.

4.3 Materials and methods

Preparation of fungal material and measurements on spore scale

A field isolate of *Puccinia triticina* was maintained on *Triticum aestivum* 'Taifun' (KWS) in a growth chamber at 22 °C and illuminance of 5000 cd m^{-2} with a 16 h photoperiod. *Triticum aestivum* 'Catargo' was used to maintain an isolate of *Puccinia striiformis* in a growth chamber at 17/13 °C day/night and illuminance of 5000 cd m^{-2} with a 16 h photoperiod. Urediniospores of both fungal pathogens were harvested and stored at 20 °C in the dark, 14 days after inoculation (dai). To acquire hyperspectral reflectance properties, urediniospores were transferred to a crafted cylindrical well inside the edge of a low reflectance dish (Brightic Black Dish), 4 mm in diameter and with a volume of 13.5 µL (Fig. 2). Thus, the theoretical total amount of spores was *c.* 1.6 million for *P. triticina* and *c.* 2.3 million for *P. striiformis*, assuming spore dimensions as given by Anikster *et al.* (2005) and Chen *et al.* (2014). To gain pure spore spectra, at least *c.* 50 spores of *P. triticina* and *c.* 44 spores of *P. striiformis* were stacked above each other in the crafted cylindrical well.

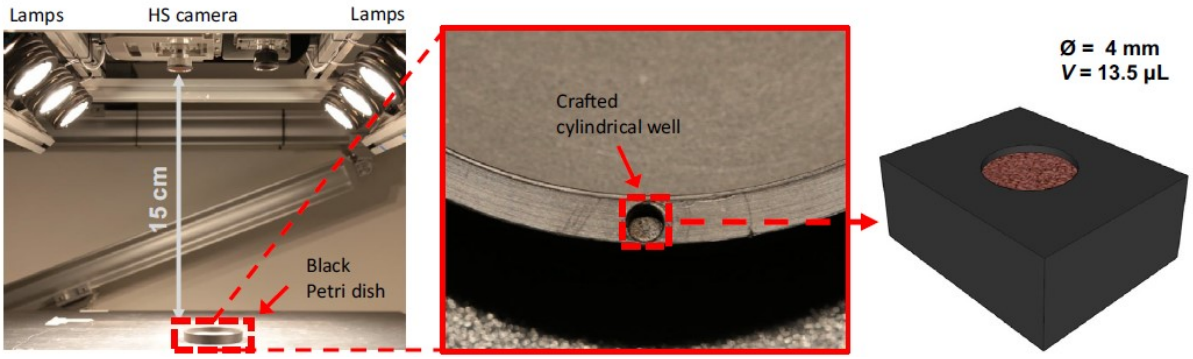

Figure 2 Hyperspectral measurement installation to record fungal spectral reflectance. Samples were placed directly underneath the hyperspectral camera using a Black Dish (Brightic). A crafted cylindrical well with a volume of 13.5 µL ensures consistent amounts and predefined distribution of the fungal spores.

Preparation of plant material and time series measurements at the leaf scale

The time series of both pathogens were performed on spring wheat *T. aestivum* 'Taifun'. Plants were spray inoculated with a spore suspension in light mineral oil (yellow rust) and in tween water (brown rust). Spore suspension was set to 8 x 10^4 urediniospores/ml. Inoculated plants were stored under conditions as for spore proliferation. Hyperspectral time series at the leaf scale were obtained by daily hyperspectral measurements during pathogenesis from infection to mature symptoms. For each disease, the same leaves were measured over time (brown rust 2–12 dai, yellow rust 2–31 dai). In each of the two experiments, four plants with four leaves were analysed, with a mock inoculated plant as the healthy control. To minimize other stress factors except the plant disease, the leaves were not cut off from the plants. The leaves of all plants were fixed in a wire mesh frame to allow the measurement of all leaves of all plants in one image with the line scanner (Fig. 3). Plant leaves were fixed in a horizontal position with the adaxial leaf side to the camera system. This design guaranteed that the leaves were measured under the same conditions every day, with regard to leaf angle, illumination and leaf position in the fixation tray. During hyperspectral time series measurements, the incidence of abiotic stresses such as water or nutrient deficiency was avoided. After each measurement, the tray with plants was brought back to the greenhouse.

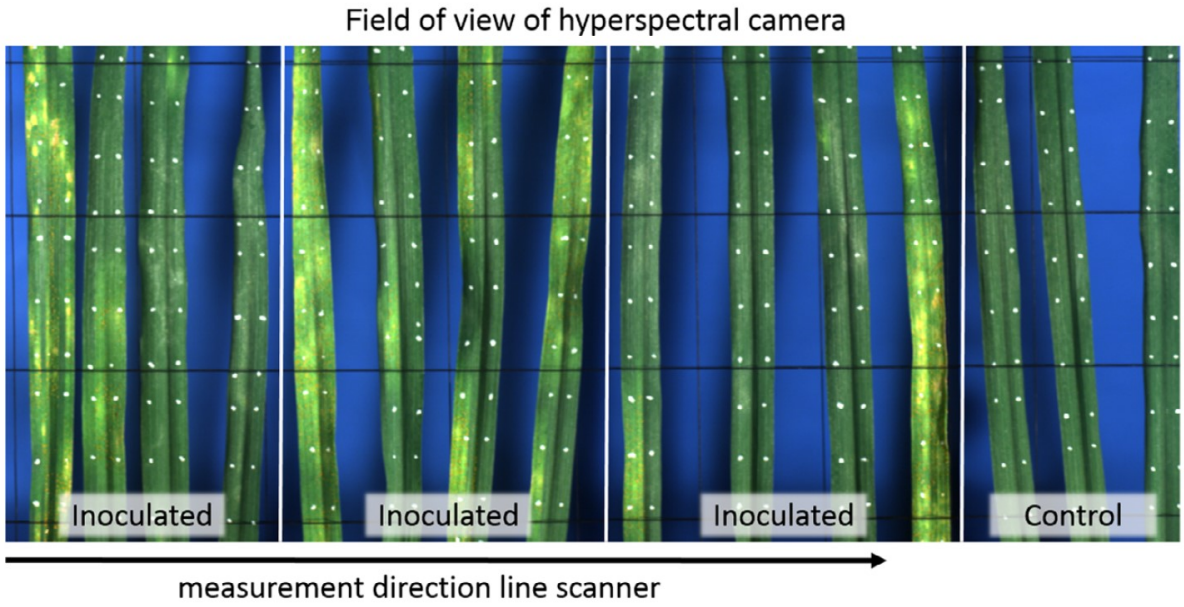

Figure 3 RGB visualization of the wire mesh from the field of view of the hyperspectral camera. Inoculated leaves show yellow rust 21 days after inoculation and homogeneous illumination of the leaf surface.

Hyperspectral imaging, data preprocessing and analysis

An ImSpector PFD V10E (Spectral Imaging Ltd) with a spectral range of 400–1000 nm and a spectral resolution of 2.73 nm was used to determine the VIS-NIR range of fungal spores. The determined and assessed pure spectra of rust spores were applied on a hyperspectral time series of brown rust (2–12 dai) and yellow rust (2–31 dai) pathogenesis using the same system and method. The hyperspectral camera was mounted on a linear stage. For image recording, the samples were placed directly underneath the camera system and were illuminated homogeneously by six halogen tungsten lamps with 10 000 lx (Analytical Spectral Devices Inc.) with a vertical orientation of 45° and a distance of 18.5 cm from the samples to the fore-optic of the camera (Fig. 2). Hyperspectral measurements were performed under controlled conditions with the exclusion of sunlight. Spectral binning was set to 4 and spatial binning was set to 1, resulting in 211 bands and 1600 pixels per line. The frame rate was set to 10 frames per second and exposure time was adjusted to the object. For a detailed description of the measuring setup, refer to Mahlein *et al.* (2012).

Hyperspectral data cubes of pure rust spores were acquired 0, 14, 28 and 67 days after harvest of spores to capture the temporal variability. To receive the relative reflectance, a white reference bar (SphereOptics GmbH) was recorded (W), followed by a dark current image (B_1). Subsequently, the spore samples (I_0) and a corresponding dark current image (B_2) was

recorded. Calculation of relative reflectance was performed according to the formula $R = (I_0 - B_2)/(W - B_1)$, using the software ENVI v. 4.6 (Exelis Visual Information Solutions). Spectral signals were smoothed by employing the Savitzky–Golay filter (Savitzky & Golay, 1964). Parameters for the smoothing process were five supporting points to the left and right and a third degree polynomial. Spectral signatures were extracted manually using a polygon region of interest of 724 pixels.

Hyperspectral image factorization

Observations on the spore scale and the representative spectra of healthy and chlorotic leaf tissue were used to factorize hyperspectral images at the leaf scale. The different spectra were combined into a library of factor spectra (Fig. 4a), composed of four brown rust spectra, four yellow rust spectra, five chlorotic spectra and six healthy spectra. For the diseases, one spectrum per measurement day (time points after harvest) was used. Signals with higher variability, such as chlorotic and healthy leaf tissue, were represented by five and six spectra, respectively. The chlorotic spectra were generated by the difference between healthy spectra and observations of different proportions of chlorotic/necrotic leaf tissue.

For factorization, a non-negative least-square fitting was performed (Lawson & Hanson, 1974). The iterative optimization algorithm was based on the active-set approach and solved the following optimization problem:

$$\min_x \|C * x - d\|_2^2 \text{ where } x \geq 0.$$

The algorithm determined for each spectrum d the linear combination of factor spectra C with minimal quadratic deviation and non-negative weights (Fig. 4b). As a result of repetitive application, a weight for each factor spectrum was determined for each pixel within a hyperspectral image. It was essential that negative weights were excluded, because a biological interpretation of a negative reflectance image was not given.

To draw conclusions, the weights of the different factor types, brown rust, yellow rust, chlorotic and healthy, were summed up to reveal the share at the specific hyperspectral signal. To extract information of larger image parts, the signal composition could be spatially averaged.

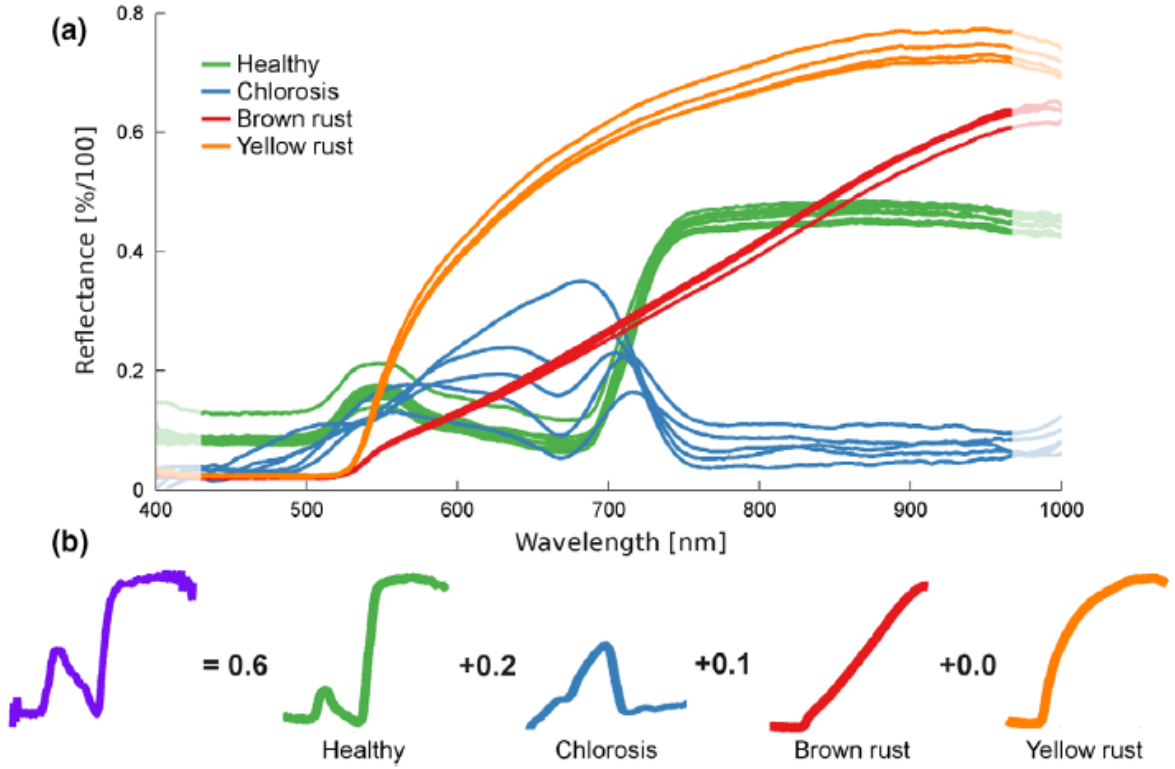

Figure 4 Composition of the hyperspectral library using spectra of healthy leaves, brown rust spores, yellow rust spores and the effect of chlorosis (a). The principle of non-negative least-squares fit of a spectrum is visualized (b). The transparent spectral border regions are disregarded in the analysis due to noise effects.

4.4 Results

The reflectance intensities of observed spore spectra differed slightly between 700 and 1000 nm according to the storage time points 0–67 days after harvest (dah, data not shown). All spectra have been included in the spectral library to represent the temporal variability of reflectance characteristics.

Detection and visualization of fungal infections at the leaf scale

The detection of brown rust and yellow rust symptoms on wheat leaves using hyperspectral images is shown in Figures 5 & 6. The observation of brown rust symptoms was performed at 12 dai, whilst yellow rust symptoms were observed at 17 dai because of slower symptom development. These measurement days were selected from a larger time series dataset to verify the method at the point of clear disease symptoms without advanced senescence. The reflectance intensities of diseased leaves differed slightly between 700 and 1000 nm. All

spectra were included in the spectral library to represent the temporal variability of reflectance characteristics.

Figures 5 and 6 show a RGB visualization derived from the hyperspectral image, the summed weights of brown and yellow rust, and the chlorotic and healthy spectra. The colour maps were linearly stretched between 0 (blue) and 0.6 (red) whereas for healthy leaf tissue they were stretched between 0 (blue) and 1.2 (red) due to the different value range.

Brown rust-infected plants

The brown rust uredinia on the leaf surface were clearly detected within the healthy leaf and, accordingly, the healthy component was reduced at these locations (Fig. 5). Some uredinia had already ruptured through the epidermal layer, whilst most were still covered. The yellow rust and chlorotic component showed almost no response, revealing that the brown rust infection had not resulted in significant chlorotic tissue. In contrast, the results suggested that the uredinia below the epidermal layer were detected as brown rust, but at a lower proportion compared to the healthy factor spectrum. This supports the idea of vertical unmixing of the different layers within the leaf as here, the semitransparent characteristics of the epidermis were used to identify the underlying brown rust uredinia.

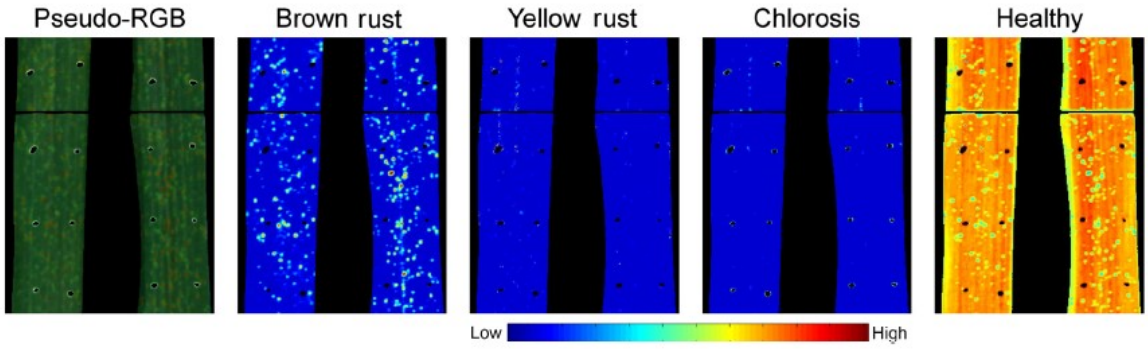

Figure 5 Factorization of wheat leaves infected with brown rust 12 days after inoculation when symptoms are already visible. Summed weights of the factor spectra of healthy leaves, brown rust spores, yellow rust spores and the effect of chlorosis are visualized.

Yellow rust-infected plants

Leaves infected by yellow rust showed different characteristics to the brown rust-infected leaves (Fig. 6). Inoculated leaves showed the highest sum weight, but other factors were also affected. Whilst the brown rust factor provided little response, the chlorotic component gave a severe response. Interestingly, it showed a different spatial pattern to the yellow rust

sporulation, indicating that the factorization method was able to separate the two different processes of (i) spore production, and (ii) chlorotic lesions below some of the uredinia. The healthy factor showed strong differences related to the geometry of the leaf. The central leaf vein appeared much darker in RGB due to shadow effects, and in consequence the sum of weights of tissue classified as healthy was reduced. This corresponded to a downscaling factor applied to the affected spectra. The healthy factor was correspondingly reduced in areas of yellow rust sporulation and chlorosis.

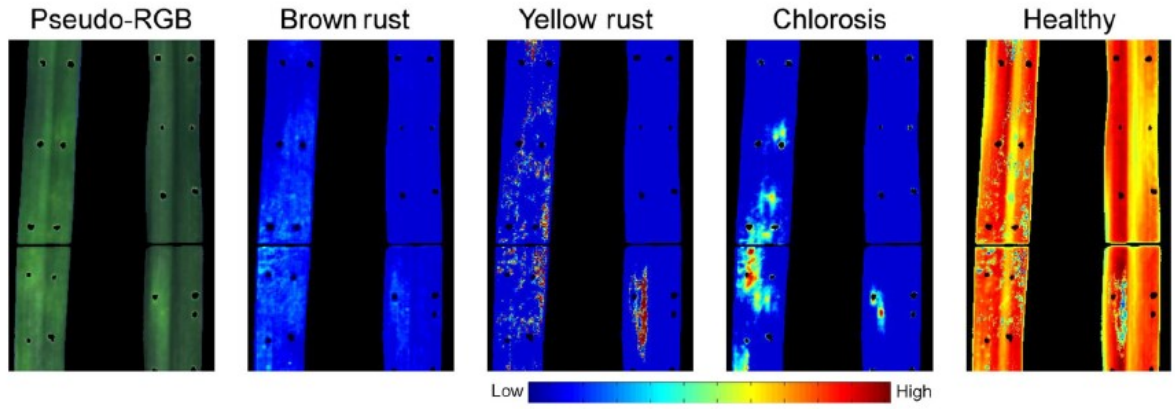

Figure 6 Factorization of wheat leaves infected with yellow rust 17 days after inoculation when symptoms are already visible. Summed weights of the factor spectra of healthy leaves, brown rust spores, yellow rust spores and the effect of chlorosis are visualized.

Temporal dynamic of factor weights of a progressing infection

The algorithm was applied to two time series experiments with brown and yellow rust on 12 wheat leaves. The background was masked and the average factor weights of all leaf pixels were calculated. Table 1 shows the percentage deviation of the factor weights from the mean factor weights of healthy leaves observed 2, 3 and 4 dai.

In the brown rust experiment, the increase in brown rust factor weights started 7 dai. After an approximately exponential increase, it reached a maximum of 1024.5 % at 12 dai. In the same period, the yellow rust component also increased but only reached a value of 308 % 12 dai. These miss assignments occurred mainly in highly necrotic regions of severely affected leaves.

In the yellow rust experiment, the increase of the yellow rust component started 12 dai and reached a maximum of 7762 % at 31 dai. In this experiment, the algorithm also showed a response for the other pathogen component. Here, a classification of brown rust increased,

but reached a much lower value of 1482 % 31 dai. Furthermore, the healthy component decreased starting from 12 dai, with a final value of −21.7 %.

4.5 Discussion and conclusion

Spores of *P. triticina* exhibited a spectral ramp pattern in the visible infrared (VIS) range with low reflectance from 400 to 500 nm. Every 100 nm, from 500 to 900 nm, the spectral reflectance was increased approximately 0.15 [%⁄100]. The strong absorption in the blue range and high reflectance in the red range is in accordance with the availability of carotenoids in the urediniospores. Spores of *P. triticina* contain a total of 1710 µg per g fresh weight carotenoids, consisting of 66.1 % γ-carotene, 21.1 % β-carotene and 12.9 % lycopene (Irvine *et al.*, 1954). Although β-carotene is non-photoactive, the molecular structure of carotenoids of long and conjugated CC-double bounds is responsible for light absorption between 380 and 550 nm (Lichtenthaler, 1987). The maximum absorption depends mainly on the oxygen-containing derivatives, which are described and grouped as xanthophylls. These develop by cyclization of the chain ends, e.g. the β-cyclization of lycopene to γ-carotene and then to β-carotene (Candau *et al.*, 1991). During different storage time points from 0 to 67 days after harvest of spores, these pigment compositions did not change and spectral differences were not significant in the VIS range (Fig. 4). Slight differences in the spectral signature could be explained due to the loss of water during storage or the natural variability between spores.

In contrast, spores of *P. striiformis* showed different reflectance signatures in the VIS range (Fig. 4). The blue range showed strong absorptions, and the spectral intensity increased at 522 nm. This spectral pattern is also in accordance with the availability of carotenoids in the urediniospores of *P. striiformis*, but with a different composition. Spores of *P. striiformis* contain >150 µg per g fresh weight, with 72% β-carotene and 28% γ-carotene (Zwetko & Pfeifhofer, 1991). In comparison to *P. triticina*, the lower amount and the different composition of carotenoids in *P. striiformis* could be responsible for the different spectral pattern starting at 550 nm. A similar result was obtained by Wahabzada *et al*. (2015), who showed differences from 550 nm in diseased barley leaves. These differences were mainly found between rust and net blotch-infested barley, even though the changes to leaf colour caused by the diseases look similar to the human eye.

The results of the factorization method based on the spectra in Figures 5 and 6 show that a separation of signal components originating from different layers within the plant leaf is

possible. In particular, the yellow rust dataset verifies the hypothesis that different fungal structures and plant cells from different layers contribute to the signal (Wahabzada *et al*., 2016). This signal can be decomposed into distinct spatial distribution maps of the investigated components, allowing the in-depth analysis of pathogenesis, e.g. the interaction of different rust species with differing amounts of chlorosis.

The spectral separation and the distinct spatial patterns derive from the underlying physiological processes. The pigment composition is a predominant characteristic of different rust populations and allows a spectral separability of spores. Spectra of spores are dominated by pigment composition, presumably acting as protection against UV light, whereas the chlorotic tissue is characterized by reduced chlorophyll content and reduced rate of photosynthesis (Brugger *et al*., 2017). Various studies have focused on the detection of rust diseases, even under field conditions (Bravo *et al*., 2003; Ashourloo *et al*., 2014; Whetton *et al*., 2018). Most of these used vegetation indices in classification scenarios where one spectrum is classified as either healthy or diseased. In the present work, it is assumed that a spectrum reflected from a leaf is composed of pixels, each representing mixed reflectance from different biological materials, including disease-specific features. These features are separated by using a spectral unmixing approach.

In yellow rust, the change of colour during symptom development can be caused by different biological processes, even if the colours look similar. Here, the different spectral signatures of developing *P. striiformis* spores and yellow chlorotic leaf tissue are distinguishable from each other, even though both signals overlap in the spatial domain.

As the reflectance signals are the result of a physical mixing, transmission measurements can provide a different perspective on the plant–pathogen interaction, complementing the reflectance signal (Thomas *et al*., 2017). The upper layers and surface structures of the leaves account for the major part of the reflectance signal, whereas the lower levels contribute more to the transmission signal (Thomas *et al*., 2018). Combining these spatially referenced measurements would allow the signal to be decomposed with greater accuracy and, furthermore, may allow a vertical localization of the signal source.

The results of this study provide an approach for analysis of a larger dataset including millions of spectra which could also include necrotic, chlorotic and senescent leaf parts, and where

decomposition could allow a plausible quantification and reliable identification of the fungal pathogen. Further work is required to test the methods on outdoor plants or in a wider range of conditions, including the presence of other diseases, nutrient effects, wetness and senescence. In contrast to a non-probabilistic identification approach (Behmann *et al.*, 2014; Thomas *et al.*, 2018), the proposed method allows a more sensible quantification, because minor factors within single pixels can also be evaluated, with the potential to exploit the data to a higher extent.

The results of the time series experiments here follow the development of the disease, with a constant increase in the disease-related components and a reduced percentage of the healthy component associated with an increase in the amount of infection. However, in both datasets the area of disease misclassification also increases, but at a lower level. The effect of leaf inclination as a result of senescent or necrotic wilting causes these miss assignments and is a limitation of this method, as it cannot be represented in the model. Nonlinear effects are represented by unrelated factors, e.g. yellow rust on the plants that were exclusively inoculated with brown rust or vice versa. Alternatively, they cannot be represented by the defined model and lead to increased residual values of the fitting process. Such increased residual values have been observed particularly in non-plant parts of the image, and at a much lower level in healthy leaf parts with strong geometry (middle vein or rolled up sections). The corresponding summed weights show an increase in the misclassification of diseases starting at 7 and 10 dai The summed weights of factor spectra of the present disease are at least tripled compared to the non-present disease. This enables a clear classification, e.g. by calculating the ratio of the two factor sums.

The spectral properties of pigmented rust spores can be unveiled from the leaf spectra. Biotrophic fungi like rusts often produce a tremendous amount of spores that affect leaf reflectance in a characteristic way. The model used here could also be promising for the detection of other rust diseases or powdery mildews, and possibly also for the differentiation of necrotrophic fungi. However, the differentiation of necrotrophic fungi has yet to be proven, and this method might not be applicable for spectra extracted from pure fungal structures of necrotrophic fungi, because of the development of necrotic areas and the presence of few macroscopically visible fungal structures on the leaf surface. The level of natural variability of spore pigmentation for most rust species is not yet known, therefore further studies are

required to evaluate this approach. Nevertheless, the proposed method can give new insights as it solves the problem of limited and uncertain training data by transferring the spectra obtained from the spore scale to the leaf scale.

The present results show and verify the potential of multiscale observations (spore and leaf scale) for quantitative and qualitative assessment of fungal and plant components within the hyperspectral signal. The method is capable of separating different spectral fungal spore signals out of the mixed signals of a diseased plant leaf. Both rust diseases were detectable and distinguishable from each other when full symptoms were exhibited. One interesting observation was the separation of yellow rust sporulation and chlorosis in the yellow rust experiment. Even though the yellow rust spores covered the chlorotic tissue, the extracted spatial distribution pattern of chlorotic tissue did not seem to be affected by the yellow rust.

The limitation of the model is the inability to represent nonlinear effects or no separable components within the signal. In the datasets investigated here, miss assignments occurred if severely necrotic leaves started to crinkle resulting in a strong relief and self-shadowing. The application of pure rust spectra in combination with a least square factorization offers the possibility of detecting and identifying brown rust and yellow rust on wheat leaves. The model is very compact and efficiently applied on the pixel scale, and an implementation of this 'spectral source' in handheld hyperspectral cameras including on-board processing capabilities (Behmann *et al.*, 2018) could allow a mobile integration of hyperspectral imaging and analysis with instant feedback.

4.6 Acknowledgements

This work was made possible by the financial support of the German Federal Ministry of Education and Research (BMBF) within the competitive grants program 'Networks of excellence in agricultural and nutrition research – CROP.SENSe.net' (funding code 0315529, junior research group 'Hyperspectral phenotyping of resistance reactions of barley') and by BASF Digital Farming. The authors would like to thank Sabine von Tiedemann for internal editing and proofreading of the manuscript.

4.7 References

Anikster Y, Eilam T, Bushnell WR, Kosman E, 2005. Spore dimensions of *Puccinia* species of cereal hosts as determined by image analysis. *Mycologia* **97**, 474–84.

Asaari M, Mishra P, Mertens S *et al.*, 2018. Close-range hyperspectral image analysis for the early detection of stress responses in individual plants in a high-throughput phenotyping platform. ISPRS *Journal of Photogrammetry and Remote Sensing* **138**, 121–38.

Ashourloo D, Mobasheri MR, Huete A, 2014. Developing two spectral indices for detection of wheat leaf rust (*Puccinia triticina*). *Remote Sensing* **6**, 4723–40.

Avalos J, Carmen Limón M, 2015. Biological roles of fungal carotenoids. *Current Genetics* **61**, 309–24.

Behmann J, Steinrücken J, Plümer L, 2014. Detection of early plant stress responses in hyperspectral imaging. *ISPRS Journal of Photogrammetry and Remote Sensing* **93**, 98–111.

Behmann J, Mahlein AK, Rumpf T, Römer C, Plümer L, 2015. A review of advanced machine learning methods for the detection of biotic stress in precision crop protection. *Precision Agriculture* **16**, 239–60.

Behmann J, Acebron K, Emin D *et al.*, 2018. Specim IQ: evaluation of a new, miniaturized handheld hyperspectral camera and its application for plant phenotyping and disease detection. *Sensors* **18**, 441.

Bravo C, Moshou D, West J, McCartney A, Ramon H, 2003. Early disease detection in wheat fields using spectral reflectance. *Biosystems Engineering* **84**, 137–45.

Brugger A, Kuska MT, Mahlein AK, 2017. Impact of compatible and incompatible barley-*Blumeria graminis* f.sp. *hordei* interactions on chlorophyll fluorescence parameters. *Journal of Plant Diseases and Protection* **125**, 177–86.

Butler M, Day A, 1998. Fungal melanins: a review. *Canadian Journal of Microbiology* **44**, 1115–36.

Candau R, Bejarano ER, Cerdá-Olmedo E, 1991. *In vivo* channelling of substrates in an enzyme aggregate for *ß*-carotene biosynthesis. *Proceedings of the National Academy of Sciences of the United States of America* **88**, 4936–40.

Chen W, Wellings C, Kang Z, Liu T, 2014. Wheat stripe (yellow) rust caused by *Puccinia striiformis* f. sp. *tritici*. *Molecular Plant Pathology* **15**, 433–46.

Dennison PE, Roberts DA, 2003. Endmember selection for multiple endmember spectral mixture analysis using endmember average RMSE. *Remote Sensing of Environment* **87**, 123–35.

Dracatos PM, Haghdoust R, Singh D, Park RF, 2018. Exploring and exploiting the boundaries of host specificity using cereal rust and mildew models. *New Phytologist* **2**, 453–62.

Hennessy CMR, Sackston WE, 1972. Inheritance of spore colour in *Puccinia helianthi*. *Canadian Journal of Genetics and Cytology* **14**, 271–8.

Jay S, Bendoula R, Hadoux X, Feret J-B, Gorretta N, 2016. A physically-based model for retrieving foliar biochemistry and leaf orientation using close-range imaging spectroscopy. *Remote Sensing of Environment* **177**, 220–36.

Kuska MT, Mahlein AK, 2018. Aiming at decision making in plant disease protection and phenotyping by the use of optical sensors. *European Journal of Plant Pathology* **152**, 987–92.

Kuska M, Wahabzada M, Leucker M *et al.*, 2015. Hyperspectral phenotyping on the microscopic scale: towards automated characterization of plant–pathogen interactions. *Plant Methods* **11**, 28.

Kuska MT, Brugger A, Thomas S *et al.*, 2017. Spectral patterns reveal early resistance reactions of barley against *Blumeria graminis* f. sp. *hordei*. *Phytopathology* **107**, 1388–98.

Lawson CL, Hanson RJ, 1974. *Solving Least-Squares Problems*. Upper Saddle River, NJ, USA: Prentice Hall.

Lichtenthaler HK, 1987. Chlorophylls and carotenoids: pigments of photosynthetic biomembranes. *Methods in Enzymology* **148**, 350–82.

Mahlein AK, 2016. Plant disease detection by imaging sensors – parallels and scientific demands for precision agriculture and plant phenotyping. *Plant Disease* **100**, 241–51.

Mahlein AK, Steiner U, Hillnhütter C, Dehne HW, Oerke EC, 2012. Hyperspectral imaging for small-scale analysis of symptoms caused by different sugar beet diseases. *Plant Methods* **8**, 3.

Mahlein AK, Kuska MT, Behmann J, Polder G, Walter A, 2018. Hyperspectral sensors and imaging technologies in phytopathology: state of the art. *Annual Review of Phytopathology* **56**, 535–58.

Mendgen K, Hahn M, 2002. Plant infection and the establishment of fungal biotrophy. *Trends in Plant Science* **7**, 352–6.

Mishra P, Asaari M, Herrero-Langreo A, Lohumi S, Diezma B, Scheunders P, 2017. Close range hyperspectral imaging of plants: a review. *Biosystems Engineering* **164**, 49–67.

Pauca VP, Piper J, Plemmons RJ, 2006. Nonnegative matrix factorization for spectral data analysis. *Linear Algebra and its Applications* **416**, 29–47.

Savitzky A, Golay JMW, 1964. Smoothing and differentiation of data by simplified least squares procedure. *Analytical Chemistry* **36**, 1627–39.

Smits BL, Mitchell HL, 1951. A rich source of y-carotene. *Science* **113**, 296–7.

Tauler, R, 1995. Multivariate curve resolution applied to second order data. *Chemometrics and Intelligent Laboratory Systems* **30**, 133–46.

Thomas S, Wahabzada M, Kuska MT, Rascher U, Mahlein AK, 2017. Observation of plant–pathogen interaction by simultaneous hyperspectral imaging reflection and transmission measurements. *Functional Plant Biology* **44**, 23–34.

Thomas S, Kuska MT, Bohnenkamp D *et al.*, 2018a. Benefits of hyperspectral imaging for plant disease detection and plant protection: a technical perspective. *Journal of Plant Diseases and Protection* **125**, 5–20.

Thomas S, Behmann J, Steier A *et al.*, 2018b. Quantitative assessment of disease severity and rating of barley cultivars based on hyperspectral imaging in a non-invasive, automated phenotyping platform. *Plant Methods* **14**, 45.

Thurau C, Kersting K, Bauckhage C, 2010. Yes we can: simplex volume maximization for descriptive web-scale matrix factorization. In: *Proceedings of the 19th ACM International Conference on Information and Knowledge Management*. New York, NY, USA: Association for Computing Machinery, 1785–8.

Torriani SFF, Melichar JPE, Mills C, Pain N, Sierotzki H, Courbot M, 2015. *Zymoseptoria tritici*: A major threat to wheat production, integrated approaches to control. *Fungal Genetics and Biology* **79**, 8–12.

Wahabzada M, Mahlein AK, Bauckhage C, Steiner U, Oerke EC, Kersting K, 2015. Metro Maps of plant diseases dynamics – automated mining of differences using hyperspectral images. *PLoS ONE* **10**, e0116902.

Wahabzada M, Mahlein AK, Bauckhage C, Steiner U, Oerke EC, Kersting K, 2016. Plant phenotyping using probabilistic topic models: uncovering the hyperspectral language of plants. *Scientific Reports* **6**, 22482.

Wang E, Dong C, Park RF, Roberts TH, 2018. Carotenoid pigments in rust fungi: extraction, separation, quantification and characterisation. *Fungal Biology Reviews* **32**, 166–80.

Whetton R, Waine T, Mouazen A, 2018. Hyperspectral measurements of yellow rust and fusarium head blight in cereal crops: Part 2: On-line field measurement. *Biosystems Engineering* **167**, 144–58.

Wold S, Esbensen K, Geladi P, 1987. Principal component analysis. *Chemometrics and Intelligent Laboratory Systems* **2**, 37–52.

Zwetko P, Pfeifhofer HW, 1991. Carotene analysis of rust spores – significance for physiology and taxonomy. *Nova Hedwigia* **52**, 251–66.

5 Detection of plant diseases in hyperspectral images by 3D-CNN

This work has been submitted to the Journal “MDPI Sensors” to the special issue “Sensors and Systems for Smart Agriculture”. Submission date: 12-Sep-2019. The current status is “Minor Revision”. Involved authors: Jan Behmann, David Bohnenkamp, Anne-Katrin Mahlein.

David Bohnenkamp conceived the experiments (50%), DB performed the experiments (100%), DB analyzed the data and wrote the paper (20%).

5.1 Abstract

Hyperspectral images provide manifold information on the plant status and potential disease symptoms, but the interpretation of such data is challenging. The most relevant patterns of plant diseases within the spectral and spatial dimensions are unknown. Deep learning models are known for the adaptation to multidimensional input as features representations are optimized during the learning phase. The use of 3D Convolutional Neural Networks allows to interpret hyperspectral data cubes directly without any preprocessing. Within this study, such a model is trained for the classification of healthy plant tissue and relevant foliar wheat diseases, i.e. Yellow Rust, Brown Rust and Septoria Tritici Blotch. On a test data set an overall accuracy of 88.1% withF1-scores between 0.79 and 0.91 are reached. Its plausibility is checked by class activation maps. They reveal that leaf parts showing obvious disease symptoms are much more relevant for disease detection than healthy or background regions. This study introduces 3D-CNNs for the detection of plant diseases based on close-up hyperspectral images to provide a basic receipt for proceeding models.

5.2 Introduction

Information on the health status of crop plants is essential for sustainable crop production. Within this context precision agriculture and phenotyping technologies are defined as promising and supportive approaches. Sensors and especially hyperspectral imaging can provide useful insights in plant state and disease symptoms, but the link to plant-physiological parameters has to be defined in many cases [1, 2].

In recent years, deep learning draws considerable attention as it allows to extract valuable information without predefined features by learning optimal feature representation during the training process [3]. A deep learning model consists of multiple layers containing data representations with different level of abstraction. In a classification model, the highest level of abstraction is typically the class probability.

As features representations are optimized during the learning phase, deep learning models can be more flexible regarding feature dimensionality. Traditional machine learning approaches mostly rely on sample representations by 1D feature vectors. In contrast, convolutional neural networks (CNNs) make use of 2D input matrices by applying convolutional filters shared between all parts of the input matrix. This reduces the number of model parameters significantly and allows the analysis of images with millions of pixels with regard to the local context [3]. The use of 3D-CNNs extends this concept to 3D convolutional filters that allow to interpret data cubes directly without neglecting the spatio-spectral context of each single entry [4]. The adapted network architecture still supports relevance measures like class activation maps (CAM) that allow to locate the relevant information within the data volume [5].

Deep learning for plant disease detection is mostly applied on RGB images [6, 7]. As a sufficient amount of RGB images is available online, the models cover multiple crops, each with its individual diseases. Plant disease detection based on hyperspectral images is a new application field for deep learning. Dijkstra et al. [8] showed that a Multi-Layer Perceptron with ReLu activation outperforms Support Vector Machines and other approaches at the detection of a disease and abiotic damage. They performed a patch-wise classification of hyperspectral images of affected potato leaves. Recently, Polder et al. [9] showed the feasibility of an infield detection of potato virus Y using hyperspectral images and a CNN.

The training of deep learning models can be time consuming but the inference step is fast, especially on dedicated hardware [10]. Deep learning models are suited for the direct integration within a hyperspectral camera if it provides sufficient computing capabilities [11]. Such a prompt data analysis would reduce some of the drawbacks of hyperspectral imaging like the large amount of recorded data and high effort for data transfer and in-house analysis.

In this study, wheat and three plant diseases, Yellow Rust (YR), Brown Rust (BR) and Septoria Tritici Blotch (STB) have been selected as biological model system. Pathogens causing rust diseases like the investigated YR and BR are biotrophic fungi and colonize the intracellular space and deduce nutrient to build spore clusters with characteristic color. Necrotrophic diseases like STB cause chlorotic and necrotic leaf tissue by the release of phytotoxic compounds. All three diseases are of high relevance for wheat production and an early identification could improve the efficiency of plant protection measures.

This study outlines the visual appearance and the biological background of the investigated disease symptoms, provides an expedient introduction in 3D-CNNs and evaluates the optimized model. Details on the selected model architecture and training parameters are stated. It is evaluated on a hold-out test data set and its plausibility is verified by class activation maps.

5.3 Materials and methods

2.1. Plant diseases on wheat

Wheat is affected by numerous plant diseases reducing the yield, limiting the yield quality or inducing mycotoxins. The used data set included three highly relevant plant diseases of wheat caused by fungal pathogens and showing symptoms on the wheat leaves. Inoculation was performed at plant state BBCH 30 [12]. Hyperspectral images are obtained when mature symptoms of each disease have been expressed resulting in a different measurement time for each disease. Details on the preparation of the biological material are provided in Bohnenkamp et al. [13].

YR on wheat is caused by the fungal pathogen Puccinia striiformis. P. striiformis is an obligate biotrophic rust fungus. It shows a massive mycelial spread between the leaf veins and leads to chlorotic leaf tissue in stripes. First symptoms are tiny chlorotic spots that can already occur 6-8 days after infection. The massive production of urediniospores appears about two weeks after infection on susceptible cultivars. Observations were performed 18 days after inoculation.

Puccinia triticina is the fungal pathogen of BR. As an obligate biotrophic rust fungus P. triticina aims to keep the hosts tissue alive as long as possible. P. triticina diverts the transport of assimilates to its own structures. As first symptoms chlorotic spots get visible five days after inoculation. During disease development chlorotic spots increase and develop stocks of urediniospores in their center. Observations were performed ten days after inoculation.

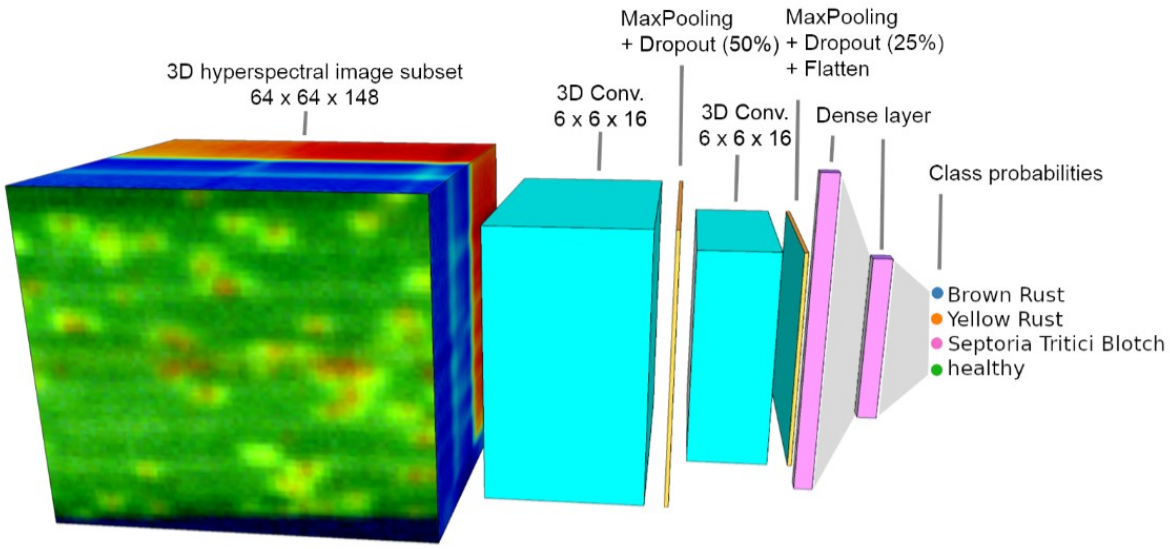

Figure 1. Structure of the used 3D-CNN with two convolutional layers and two fully connected layers with around 500,000 parameters. Three diseases and the healthy control group were used as target classes of the model.

STB is caused by Zymoseptoria tritici. STB is one of the most important foliar diseases of wheat and currently the most important in Europe [14]. The ascomycete has a biotrophic and a necrotrophic phase. The biotrophic phase proceeds asymptomatic. The necrotrophic phase leads to the collapse of cells of the leaf tissue and initial small chlorotic spots resulting in necrotic lesions that can spread over the whole plant leave. Mature necrotic lesions form pycnidia in the substomatal cavities. Observations were performed 22 days after inoculation.

2.2. Hyperspectral imaging

The leaves were horizontally fixated in a wire frame to capture hyperspectral images. Hyperspectral camera ImSpector PFD V10E (Spectral Imaging Ltd., Oulu, Finland) with a spectral range of 400-1000 nm was used in nadir orientation to observe the fixated leaf samples at a distance of 42.5 cm. The images reach a pixel size of 0.15 mm. Further details on the measuring setup are provided in [13]. Spectral signals were smoothed by employing the Savitzky-Golay filter with 11centered supporting points and a third degree polynomial. To reduce the effect of noise in the spectral border regions bands 1-20 and 181-211 are removed from the data set. Overall, a test set of 500 image samples per disease and 1500 image samples for the healthy control group as well as the hold-out test data set were generated (data dimensions 64 x 64 x 148 px). Training and test data were obtained from different leaves to increase the reliability of model evaluation.

2.3. 3D-CNNs for classification

CNNs using 2D convolutional filters are well established for image analysis [3, 15]. Due to the 3D data characteristics of hyperspectral images, 3D-CNNs are applied (Fig. 1). They use the same methodological frameworks as CNNs but use 3D filters for convolution. As a result, the spatial-spectral characteristics are not separated but used in a joint fashion as feature for the following layers. 3D-CNNshave been introduced by Tran et al. [16] for action recognition based on video data. Nagasubramanian et al. [4] used 3D-CNNs for the classification of the disease stem rot and utilized saliency maps for the interpretation and evaluation of the model characteristics. The use of 3D-CNNs is an adaptation of CNNs with two-dimensional convolutional filters. For 2D-CNNs, each filter *K* is a 2D matrix which is convoluted with the 2D input image to provide the 2D output *S* image for the next layer.

$$S(i,j) = (K*I)(i,j) = \sum m \sum n I(i-m,j-n)K(m,n) \quad (1)$$

The entries of the kernel matrix are optimized during the training phase and shared for the whole image. To deal with RGB images with three channels, the kernels are frequently applied and optimized channel-wise. For 3D convolutional layers the kernel is extended to a 3D matrix and the channels or bands are analyzed in a joint approach.

$$S(i,j,k) = (K*I)(i,j,k) = \sum m \sum n \sum o I(i-m,j-n,k-o)K(m,n,o) \quad (2)$$

The associated layers for pooling are extended in the same way. In image analysis, the combination of convolutional layers with dense layers has proved to be successful [3]. Using this approach, the relevant information is compressed in a decreasing number of nodes resulting in more abstract features. Following the proposed model consists of two 3Dconvolutional layers (kernel dimensions 6 x 6 x 16 in both cases) and two fully-connected dense layers (50 and 4 neurons). Max pooling (2 x 2 x 2) on the convolutional output has been applied as usual. Dropout has been applied in two layers to prevent overfitting. Due to the high number of kernel parameters, dropout has been applied also between the convolutional layers. The last two layers can be interpreted as non-linear classification. These layers use vector valued input layers to generate vector valued output layers. The last dense layer has as many output nodes as classes to predict. Using softmax, class probabilities are assigned to these output nodes. For the transition of the 3D convolution part of the model to the 1D dense

part, a flattening operation is applied that reshapes a 3D input layer to a 1D output layer by simply lining up all entry of the 3D matrix.

2.3.1. Training and model validation

The risk of overfitting was reduced by 3-fold data augmentation, in which the spatial dimensions of the samples were transposed and mirrored resulting in 12,000 image samples for training. Due to the direct relationship to the classification accuracy, categorical cross-entropy has been used as loss measurement for the model during the training by Adam optimizer. The training was performed in multiple steps in which the learning rate was adapted from 0.01 to 0.001 to 0.0001. Each of the stages has a duration of 100 epochs consisting with a mini batch size of 64 (Fig. 2). All operations have been performed with Keras 2.1.3 and Tensorflow 1.5.0 backend. The training and validation phase has been conducted on a Xeon E5-1620 using two Nvidia TITAN GPUs, each with 6GB memory.

2.3.2. Relevance indicators

Deep learning models are hard to interpret as a single model parameter is generally not related to a specific meaning. Nevertheless, approaches for the visualization of filters and ways of interpretation arein focus of current research [5]. Class activation maps (CAM) localizes the relevance for a classificationwithin the data. Averaging the spectral or spatial dimensions across a large data set allows to extractrelevant positions in spectral or spatial domain. The CAM visualization has been conducted using keras-vis library 0.4.1 [17] on Intel Core i7-3930Ksystem with a Nvidia GTX 1050 with 4GB memory.

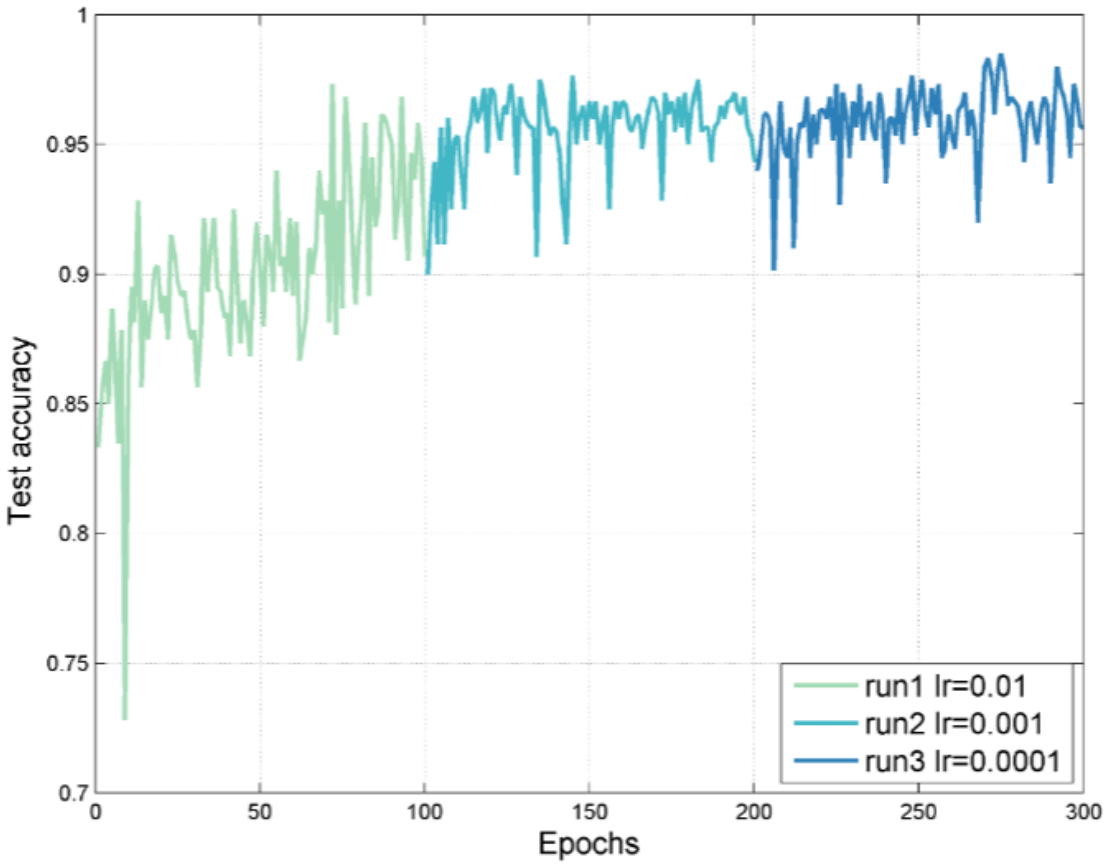

Figure 2. Test accuracy of the three consecutive training phases with Adam optimizer (lr = 0.01, 0.001, 0.0001).

5.4 Results and discussion

3.1. Optimization phase

The overall training was performed in approximately 23 hours. Extending the number of epochs before changing the learning rate to more than 100 did not improve the model accuracy. In accordance with [15], the model accuracy during the presented learning structure stagnated after approximately100 epochs in each phase but improved if the learning rate has been changed (Fig. 2). However, increasing the model accuracy by further learning rate changes was not possible. Presumably, the composition of the training data as well as the capacity of the model architecture has to be adapted fora significant increase in model performance.

3.2. Improved interpretation by feature relevance

The visualization of relevant regions by CAM within the images allows a plausibility verification of the model obtained during the training process [4]. Disease detection models should mostly

rely on the specific disease symptoms and their direct neighborhood to represent their shape. In contrast, unrelated leaf tissue or background material should be less relevant. Using CAM, the relevant regions are located for each of the disease (Fig. 3). For YR the elongated uredinia, for BR the smaller round uredinia and for STB the locations of the larger areas of necrotic leaf tissue are highlighted. In summary, the trained model has the striven property. Furthermore, the CAM approach may provide support if multiple diseases are present within one image (not tested). Different target classes could be differentiated and their symptoms could be located.

3.3. Classification accuracy

The application of the optimized model to the hold-out test data set reveals a usable accuracy of 88.1% (cv. Tab. 1). Thereby, the accuracy of the individual classes measured by theF1-score is not homogeneous. The highestF1is reached by the healthy class with 0.91, followed by BR with 0.89, STB with 0.86 and YR with 0.79. The performance differences can be related to the data set composition and symptom characteristics. The healthy class reached the highest accuracy as it is represented by50% of the training data and is characterized by a low spatial heterogeneity. The BR showed very characteristic and evenly distributed symptoms on the whole leaf. Image samples showing only few BR symptoms are very rare. In contrast, YR showed a lower number but larger uredinia of bright yellow color similar to chlorotic tissue. Furthermore, YR uredinia are accompanied by larger and more pronounced chlorosis, the characteristic symptom of STB, impeding the separation of YR and STB. The complexity of separating YR and STB in comparison to BR is reflected also in the confusion matrix (Tab. 1).

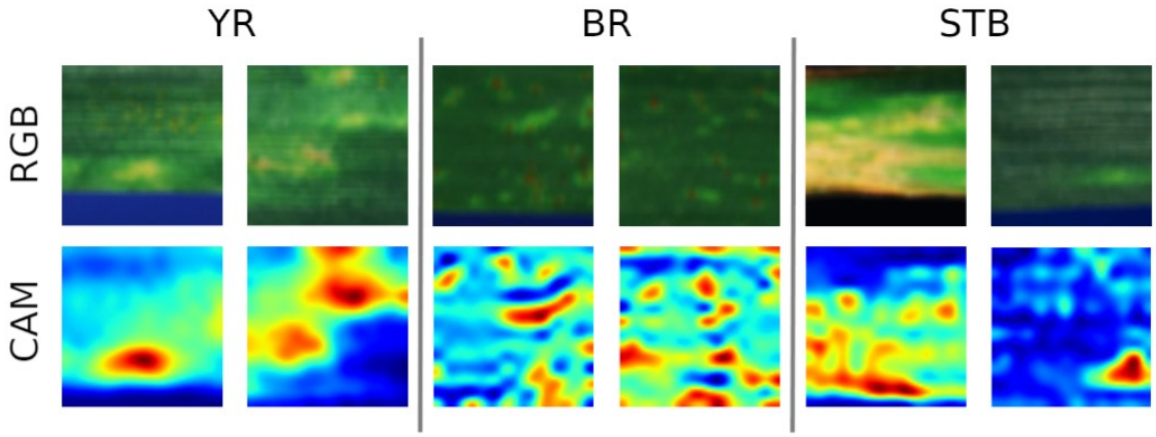

Figure 3. Class activation maps (CAM) averaged in the spectral dimension for Yellow Rust (YR, left), Brown Rust (BR, center) and Septoria Tritici Blotch (STB, right).

Table 1. Confusion matrix of the model performance on a holdout test data set including healthy leaf tissue, Yellow Rust (YR), Brown Rust (BR) and Septoria Tritici Blotch (STB) samples.

	healthy	YR	BR	STB	Precision
healthy	1392	17	58	33	92.8%
YR	87	368	1	44	73.6%
BR	50	0	450	0	90.0%
STB	15	51	0	434	86.8%
Recall	90.1%	84.4%	88.4%	84.9%	Acc. = 88.1%

One aspect that has not been regarded but may has impact on the obtained accuracy is the optimization of the spatial scale of the input samples. The spatial scale of the image samples is the result of the interplay of pixel dimensions, aperture angle and observation distance. Depending on the data set a specific size is optimal to represent the characteristics of a disease. This number will differ between data sets and also classes [10]. Applied to plant diseases, the 64 x 64 px may represent the Symptoms much better than the large scale symptoms of STB and YR.

There are two closely related challenges for the training of a disease detection model, the heterogeneity of disease severity in hyperspectral data and the limited amount of training data. Even highly controlled inoculation experiments produce image samples with very low or even invisible disease symptoms which tend to be misclassified to the healthy class. The natural variability of the classes has to be represented within the training data but wrong labels have the potential to reduce the overall accuracy significantly [18]. If the class variability in the training data varies strongly, an implicit class weighting is performed favoring the less variable classes. Rigorous checks on label quality as well as a compensation of deviating class variabilities may be of high relevance for future models.

The ratio of training sample size and required model complexity is decisive for the optimization process [19]. Therefore, many prediction models in plant context face the problem of limited training data. To compensate they are based on available models pre-trained on millions of images [20]. Training only the last layers and adopting the parameters of the convolutional layer are in many cases sufficient to adapt the model to a new task. In the context of hyperspectral imaging such pre-trained models are not available [20]. Consequently, it is required to learn from scratch with randomized initialization. The

availability of suitable data or pre-trained models may change in the future, but currently descriptions of successful configurations provide an added value.

The interpretation of highly controlled close-up images is an intermediate research step. Disease detection in the laboratory may be relevant in special cases but with low impact on agriculture.

Especially for wheat, the relevant scales are large fields. Hyperspectral observations in the field are challenging as typically illumination is less stable and a leaf fixation is impossible. The variable leaf angles and observation distances strongly impair the hyperspectral signal [1]. Moreover, a sufficient label quality in the field is hard to obtain as the covered area is typically too large to be assessed by a human rater. The presented model is not able to handle field data as the expected variability is not included in the used training data. However, it can be used as base model and extended by new data with a broader focus. Training a field model from scratch is even more challenging than in the laboratory due to the enumerated problems. Due to the release of data interpretation from assumptions and prior knowledge, CNNs are especially suited for in-field applications. In such scenarios the prior knowledge and the relevance of application are in imbalance.

We believe there are two approaches to proceed with hyperspectral disease detection. In the first approach, all available data will be composed into a large data set. The enormous biological variability will be handled by the huge amount of hyperspectral data provided by multiple research groups. The second approach will rely on a unified sensor setup that is able to reduce drastically the variability caused by environmental conditions. If such a platform will be accepted in the research community, the focus of the obtained data can be broadened, yet preserving the interchangeability of models and datasets. We believe that the second approach is more expedient as the number of research groups working on hyperspectral disease detection is low and affordable and user-friendly sensors are not available for hyperspectral imaging data. Furthermore, deep learning is well suited for the interpretation of hyperspectral images and will advance the plant disease detection as it has been shown also in other fields.

5.5 Conclusion

This study presents the application of 3D-CNNs in the novel context of differentiating multiple foliar plant diseases based on close-up hyperspectral images. The model allows to classify hyperspectral images in their raw 3D representation without neglecting the spatial or spectral context of individual measurements. The straight-forward model definition and training process reached an overall accuracy of 88.1%. The plausibility was furthermore verified using CAM analysis. This study provides a working configuration regarding data set characteristics, model architecture, training strategy and evaluation methods. This sets a starting point for extended applications. Thereby the potential of 3D-CNNs for greenhouse or even the field scenarios will be assessed by further studies.

5.6 References

1. Mahlein, A.K.; Kuska, M.T.; Behmann, J.; Polder, G.; Walter, A. Hyperspectral sensors and imaging technologies in phytopathology: State of the art. Annual Review of Phytopathology 2018, 56, 535–558.
2. Lowe, A.; Harrison, N.; French, A.P. Hyperspectral image analysis techniques for the detection and classification of the early onset of plant disease and stress. Plant Methods 2017, 13, 80.
3. LeCun, Y.; Bengio, Y.; Hinton, G. Deep learning. Nature 2015, 521, 436.
4. Nagasubramanian, K.; Jones, S.; Singh, A.K.; Singh, A.; Ganapathysubramanian, B.; Sarkar, S. Explaining hyperspectral imaging based plant disease identification: 3D CNN and saliency maps 2018.
5. Zhou, B.; Khosla, A.; Lapedriza, A.; Oliva, A.; Torralba, A. Learning deep features for discriminative localization. Proceedings of the IEEE Conference on Computer Vision and Pattern Recognition 2016, 2921–2929.
6. Wallelign, S.; Polceanu, M.; Buche, C. Soybean Plant Disease Identification Using Convolutional Neural Network. The Thirty-First International Flairs Conference 2018, 146–151.
7. Ferentinos, K.P. Deep learning models for plant disease detection and diagnosis. Computers and Electronics in Agriculture 2018, 145, 311–318.
8. Dijkstra, K.; van de Loosdrecht, J.; Schomaker, L.; Wiering, M. Hyper-spectral frequency selection for the classification of vegetation diseases. European Symposium on

Artificial Neural Networks, Computational Intelligence and Machine Learning 2017, 483–488.

9. Polder, G.; Blok, P.M.; de Villiers, H.; van der Wolf, J.M.; Kamp, J. Potato Virus Y detection in seed potatoes using deep learning on hyperspectral images. Frontiers in plant science 2019, 10, 209.
10. Chen, Y.; Jiang, H.; Li, C.; Jia, X.; Ghamisi, P. Deep feature extraction and classification of hyperspectral images based on convolutional neural networks. IEEE Transactions on Geoscience and Remote Sensing 2016, 54, 6232–6251.
11. Behmann, J.; Acebron, K.; Emin, D.; Bennertz, S.; Matsubara, S.; Thomas, S.; Bohnenkamp, D.; Kuska, M.T.; Jussila, J.; Salo, H.; Mahlein, A.K.; Rascher, U. Specim IQ: evaluation of a new, miniaturized handheld hyperspectral camera and its application for plant phenotyping and disease detection. Sensors 2018, 18, 441.
12. Meier, U. Growth stages of mono-and dicotyledonous plants, 2. ed.; Blackwell Wissenschafts-Verlag, 2001.
13. Bohnenkamp, D.; Kuska, M.; Mahlein, A.K.; Hyperspectral signal decomposition and symptom detection of wheat rust disease at the leaf scale using pure fungal spore spectra as reference. Plant Pathology 2019, 68(6): 1188–1195.
14. Fones, H.; Gurr, S. The impact of Septoria tritici Blotch disease on wheat: an EU perspective. Fungal Genetics and Biology 2015, 79, 3–7.
15. Goodfellow, I.; Bengio, Y.; Courville, A.; Bengio, Y. Deep Learning; Vol. 1, MIT Press Cambridge 2016.
16. Tran, D.; Bourdev, L.; Fergus, R.; Torresani, L.; Paluri, M. Learning spatiotemporal features with 3dconvolutional networks. Proceedings of the IEEE International Conference on Computer Vision 2015, 4489–4497.
17. Kotikalapudi, R.; contributors. keras-vis. https://github.com/raghakot/keras-vis, 2017.
18. Frénay, B.; Verleysen, M. Classification in the presence of label noise: a survey. IEEE Transactions on Neural Networks and Learning Systems 2014, 25, 845–869.
19. Foody, G.; McCulloch, M.; Yates, W. The effect of training set size and composition on artificial neural network classification. International Journal of Remote Sensing 1995, 16, 1707–1723.

20. Singh, A.K.; Ganapathysubramanian, B.; Sarkar, S.; Singh, A. Deep learning for plant stress phenotyping: trends and future perspectives. Trends in Plant Science 2018, 23, 883–898.

6 In-field detection of yellow rust in wheat on the ground canopy and UAV scale

This work has been published as:

Bohnenkamp, D., Behmann, J., & Mahlein, A. K. (2019). In-Field Detection of Yellow Rust in Wheat on the Ground Canopy and UAV Scale. *Remote Sensing*, *11*(21), 2495.

David Bohnenkamp conceived the experiments (50%), DB performed the experiments (50%), DB analyzed the data and wrote the paper (50%).

Text was not modified from the published version.

6.1 Abstract

The application of hyperspectral imaging technology for plant disease detection in the field is still challenging. Existing equipment and analysis algorithms are adapted to highly controlled environmental conditions in the laboratory. However, only real time information from the field scale allows to guide plant protection measures and to optimize the use of resources. At the field scale, many parameters like the optimal measurement distance, informative feature sets and suitable algorithms have not been investigated. In this study, the hyperspectral detection and quantification of yellow rust in wheat is evaluated using two measurement platforms: a ground-based vehicle and an unmanned aerial vehicle (UAV). Different disease developing stages and disease severities have been provided in a plot-based field experiment. Measurements were performed weekly during vegetation period. Data analysis was performed by three prediction algorithms with a focus on the selection of optimal feature sets. In this context also the across-scale application of optimized feature sets, an approach of information transfer between scales, is evaluated. Relevant aspects for an on-line disease assessment in the field integrating affordable sensor technology, sensor spatial resolution, compact analysis models and fast evaluation are outlined and reflected. For the first time, hyperspectral imaging observation of a plant disease experiment have been comparatively performed at two scales, ground canopy and UAV.

6.2 Introduction

Today's demands to agricultural cropping systems are high. Agroecosystems have to be highly productive while the undesirable impact on the environment has to be as low as possible. Resource conserving methods with a minimum of chemical input are in favor. One vision to approximate this goal are site-specific cropping measures. A site-specific management has the potential to lead to a higher or constant productivity with a constant or reduced input of resources [1]. One segment for site-specific-applications are plant protection measures [2].

The spatial occurrence of plant diseases in the field, especially in the early season, is often heterogeneous while in most cases plant protection compounds are applied homogeneously onto the crop. This spatial heterogeneity of disease occurrences might lead to diverse fungicide demands that are often not considered. Many diseases firstly occur in patches before they start spreading in the field. One approach for a site-specific application of plant protection measures might be the application of fungicides in patches of disease occurrence [3-5]. This could prevent or stop disease spreading without applying a fungicide to the whole field [1].

Spectral sensors might be tools to accomplish the perceptions of a site-specific disease management [6, 7]. Spectral sensors measure the light reflected from the crop canopy [1]. During pathogen attack and disease development on the crop leaf, diseases establish a spectral fingerprint in the reflected leaf signature [8-10]. These shifts of the signature can be detected using spectral sensors particularly in the electromagnetic spectrum from 400 – 2500 nm [11]. Spectral sensors can be divided into hyperspectral and multispectral sensors, depending on their spectral resolution. The number and width of measured wavebands mainly characterize the spectral resolution [11].

Non-imaging hyperspectral sensors average the spectral information over a certain area while imaging sensors contain the spectral information for each pixel [7]. Hyperspectral imaging sensors (HIS) provide spectral information in a spatial resolution. Multispectral sensors typically cover i.e. the RGB-range with an additional NIR band. These sensors are less cost intensive and generated data is less complex but does not cover the broad spectral range like a hyperspectral sensor.

Spectral sensors have been applied on different scales [12]. For field approach, a hyperspectral camera can be mounted to a ground-based vehicle or to a UAV [3, 1, 13, 11]. Depending on the interrogation and measuring setup, each scale can have advantages and disadvantages.

On ground scale it is possible to detect small features of a few millimeters through high resolution on close range while the throughput on the UAV scale is much higher with still higher resolution compared to satellite imagery [14, 5, 15, 16]. For field applications of spectral sensors, depending on the scale, the resolution or the measurement time can become a limiting factor. Most field applications for disease detection focused on the calculation of vegetation indices (VIs) [17-19] using multispectral sensors. VIs are developed by accounting certain band ratios to highlight one factor and reduce the impact of another factor [20]. Depending on the wavelength, these indices can be either indicators for crop vitality, general crop stress, pigment content or a specific plant disease [21, 18]. Few works showed an approach for disease detection using imaging hyperspectral sensors under field conditions [10]. This might be due to the reason that spectral measurements under field conditions are challenging and the complexity of hyperspectral data is higher than multispectral data [1]. The features of multispectral sensors might result in lower image acquisition durations and lower susceptibility to environmental factors during measurements. The image quality of field data in general is influenced by various factors. Beside suitable weather conditions, the field crop species and also the disease symptom type are of high relevance for successful measurements. The leaf architecture and disease occurrence on the plant mainly determines the detectability of the disease. Disease presence on lower plant and leaf levels result in a decreased reflected signal. Disturbing weather conditions such as wind and rain can easily impair spectral images obtained in the field. One elusive and eminently important factor is the illumination. Changing illumination conditions over time, caused by clouds or solar altitude, can lead to uninterpretable data, because spectra of different images cannot be compared with each other anymore [3, 1, 22]. The detection of diseases on different leaf levels is also challenging because of inhomogeneous illumination conditions through the leaf altitude in the crop stand and upper leaves that cast shadow. Also these leaves might be in different developmental stages and a senescent leaf has to be differentiated from a healthy green or a diseased leaf. The leaf angle to the camera influences the spectral signal. Not least the image quality is essentially determined by the spatial resolution of the used sensor system. Small symptoms of a disease can only be visualized when the spatial resolution in combination with the measurement distance is appropriate for the desired data quality.

So far various field measurements on the ground canopy scale of cereal crops focused on the detection of biotrophic diseases such as yellow rust [3, 13, 23, 10, 24, 25], brown rust [18, 26]

and powdery mildew of wheat [19]. This might be due to the fact that biotrophic diseases appear more likely on the upper leaf layers because of wind distribution and a preference for fresh and healthy leaf tissue [27]. Necrotrophic diseases are most severe on lower leaf levels and therefore more difficult to detect by remote sensors. A detection and quantification of septoria tritici blotch with a hyperspectral radiometer was shown in the field [28].

The analysis and interpretation of sensor data is crucial for future implementation. Promising techniques are algorithms from machine and deep learning, in combination with suitable sensors and measurement platforms. These methods are particularly suitable to cope with the amount of wavebands provided in hyperspectral data and can be used for the detection of plant diseases [29-32, 7].

This work presents a new approach for field trial studies using innovative HIS and machine learning for a pixel wise detection of crop diseases. A winter wheat trial was conducted in the vegetation period of 2018. The crop was infected with *Puccinia striiformis,* the causal agent of yellow rust (YR). Weekly hyperspectral measurements were performed on the ground canopy and the UAV scale to monitor the spectral dynamic of crop stands during the vegetation period. Measurements were performed on a mobile field platform in a distance of 50 cm to the crop canopy and with a UAV drone in 20 m height over the plots to work on and compare different scales. Hyperspectral images were captured using a line scanner attached to a linear stage in a measurement booth and a frame based hyperspectral camera for UAV applications. Field data were preprocessed and normalized and then analyzed using the supervised classification methods Spectral Angle Mapper (SAM) and Support Vector Machine (SVM) to detect yellow rust of wheat. Additionally, a feature selection was performed on hyperspectral data to verify the potential for a waveband reduction from hyperspectral to multispectral data for disease detection.

6.3 Materials and methods

Field trial layout

In the vegetation period 2017/2018 a field trial with winter wheat was conducted at trial station Campus Klein-Altendorf 50°37’31.00’’N, 6°59’20.54’’E (Rheinbach, Germany). In 2016/2017 a first field trial was performed for specifying the measuring setup and routine (data are not shown). The cultivars JB Asano (Limagrain GmbH, Edemissen, Germany) and Bussard (KWS SAAT SE, Einbeck, Germany) were sown on 26.10.2017 with 320 kernels/m².

Field emergence was on 14th November 2017 while harvest took place on 24.07.2018. JB Asano was chosen because of a susceptibility to YR. The field trial was designed in 10 treatments per cultivar with two repetitions resulting in 40 plots (plot size: 3x7m). The plot design was randomized within each cultivar. With a change of the cultivar after each plot the direct proximity of plots with the same cultivar was avoided. This was designed to arrange the field trial into two long rows of plots with cultivars alternating after each other in 20 plots per repetition (Fig. 1). The treatments within one cultivar were randomized. Two fertilizer intensities (160kg N/ha and 30kg N/ha) were applied per cultivar. For cultivar Asano, two treatments were used for additional inoculation with YR. The whole field trial was aligned from North-West to South-East direction.

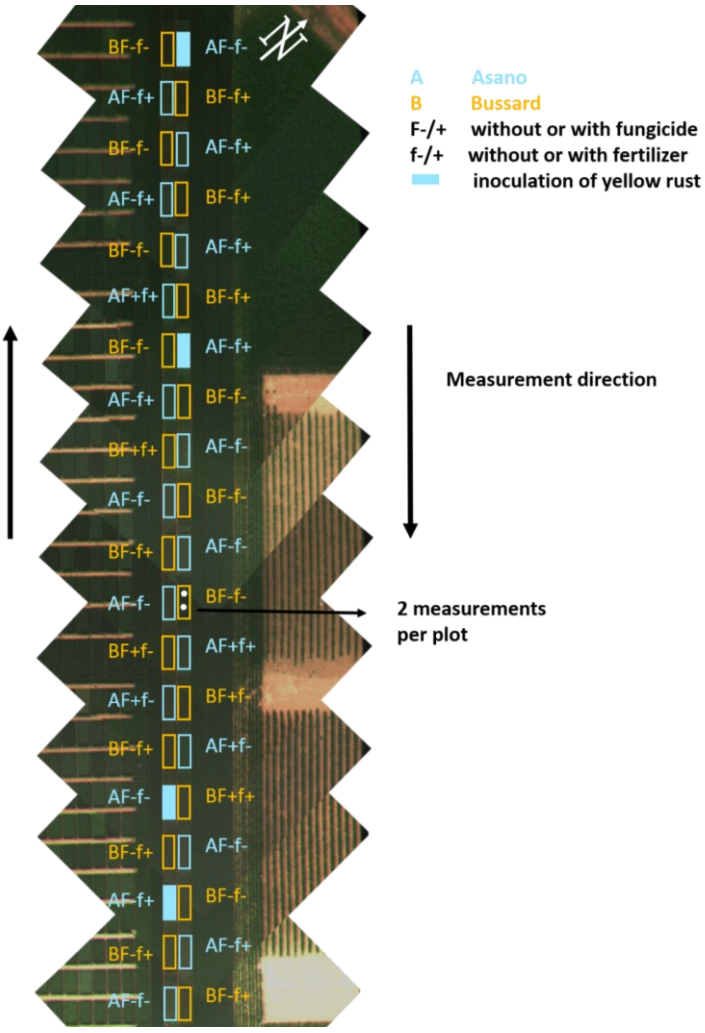

Figure 1. Field trial layout (RGB-stitch from UAV-images) at the research station Campus Klein-Altendorf (Rheinbach, Germany) of winter wheat varieties Bussard and Asano in 2018 with treatment declaration, and measurement strategy. The trial was designed in two long rows of plots to reduce the amount of turns and keep continuous measurements.

Inoculations

Additional inoculations of *Puccinia striiformis* were performed in April and May (25.04.2019; 12.05.2019). To establish high disease infections, the inoculations were repeatedly performed by applying a spore suspension on the plants immediately after rainfall incidences. Inoculations were timed to forecasted infection risks after the xarvio field manager (BASF Digital Farming GmbH, Münster, Germany). The spore suspension was applied with a garden pump sprayer and contained $8x10^4$ spores/ml. Two liters of spore suspension were homogeneously applied over one plot.

Visual disease ratings

Visual disease ratings were performed weekly from calendar week 17-23. One plot was rated two times at the same locations where hyperspectral measurements took place. Disease incidence was assessed by the eye of a human rater. The diseased leaf area (%) was rated on 15 leaves per leaf level. Additionally, the growing stage and the amount of visible leaf area of each leaf level in the hyperspectral image (from top view) was ascertained.

Crop stand and disease development

The vegetation in 2018 started late in March and was denoted by a drought that especially affected the length of the growing season and lead to an early harvest in July (Fig. 2). Septoria tritici blotch, tan spot and powdery mildew were insignificant during the complete growing season. YR could establish a significant infection on cultivar Asano and measurements were not aggravated due to mixed infections. First YR symptoms were found in mid of April and were based on natural infection incidences. Until beginning of May (BBCH 31) a serious increase of YR was rated. Warm days and cold nights seemed to favor infection incidences through dew formation. Until mid of May (BBCH 37-39) YR was the dominating disease.

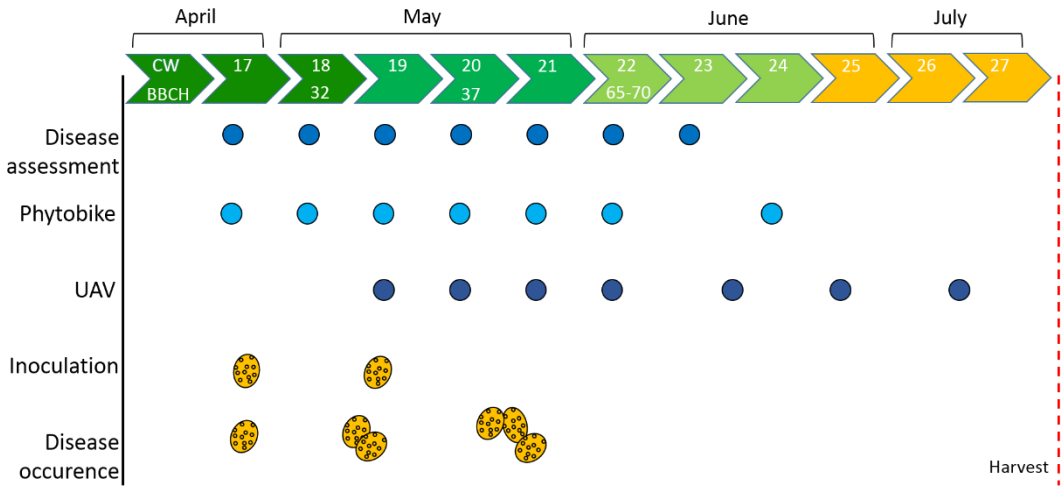

Figure 2. Schematic overview of the course of vegetation period 2018. For each calendar week, the actions are presented and disease occurrence of yellow rust is shown. Weekly assessments and measurements were performed during the vegetation period (CW = calendar week).

Measurement platforms

Field platform Phytobike

The measurement platform based on a square steel construction with four wheels, provided by Forschungszentrum Jülich (Jülich, Germany), covers 3-meter-wide experimental plots (Figure 3). Sensors for reflectance characteristics as well as localization systems, power supply and control of the sensors from a control laptop were mounted to the steel frame. All sensors were variable in height by a moveable aluminum profile construction. By this, the sensor platform can be adapted to the growth stages of the plants and a constant distance between sensors and crop canopy is enabled. With a weight of around 150 kg, the construction approaches the limit of platforms without steering, which can still be moved by the physical strength of two people.

As a hyperspectral sensor, the Specim V10E line camera (Specim Oy, Oulu, Finland) was used. The motion required for the Specim V10E camera was realized by a linear stage (Velmex, Bloomfield, USA). Measurements were triggered via the control computer allowing a flexible reaction to changing light situations by an adapted integration time. The Specim V10E camera measured the electromagnetic spectrum in a range from 400 to 1000 nm with a spectral resolution of 2.73 nm. Sunlight was used as natural light source. A canvas measuring cabin was constructed to avoid shadow cast by sensors and equipment of the Phytobike.

UAV measurements

The UAV allows to perform overview images of whole experiments or at least of parts of the experiment. Recent technologies enable hyperspectral imaging at UAV scale. We combined a UAV DJI Matrice 600 (Da-Jiang Innovations Science and Technology Co., Shenzen, China) with a Rikola hyperspectral camera (Senop Oy, Oulu, Finland) (Fig. 3). The Rikola camera measures the reflected light in a range from 500 to 900 nm. The measured wavebands were selectable and spectral resolution was set to 7 nm using 55 wavebands. With flight times of around 20 minutes, the whole experiment was captured within one battery capacity. For plot observations, 20 m flight height has been selected and the UAV hoovered over each plot center for a duration of 10s. Sunlight was used as natural light source.

Figure 3. Construction plan of the Phytobike (top left) and the final appearance in the field including the cotton diffusor (top right). The used UAV system consisting of a DJI Matrice 600 and a Rikola hyperspectral camera (bottom left). Normalization was performed using a 50 % grey reference panel (bottom right).

Data preprocessing

This study focused on the information about relevant wavebands as the central outcome. We used a dataflow to assess the capability to transfer this information between observation scales (Fig. 4). There, we built two datasets for yellow rust prediction, a classification dataset on field scale and a regression data set on UAV scale. Multiple prediction models and feature selection results were derived. In the final step, models were optimized using the selected features, whereas feature section information were also exchanged. The resulting four classification models with selected features, two on field scale (features selected on field scale and on UAV scale) and two on UAV scale (features selected on field scale and on UAV scale), were evaluated. This allowed to evaluate the value of feature selection and, more specifically, the value of feature information obtained at a different observation scale.

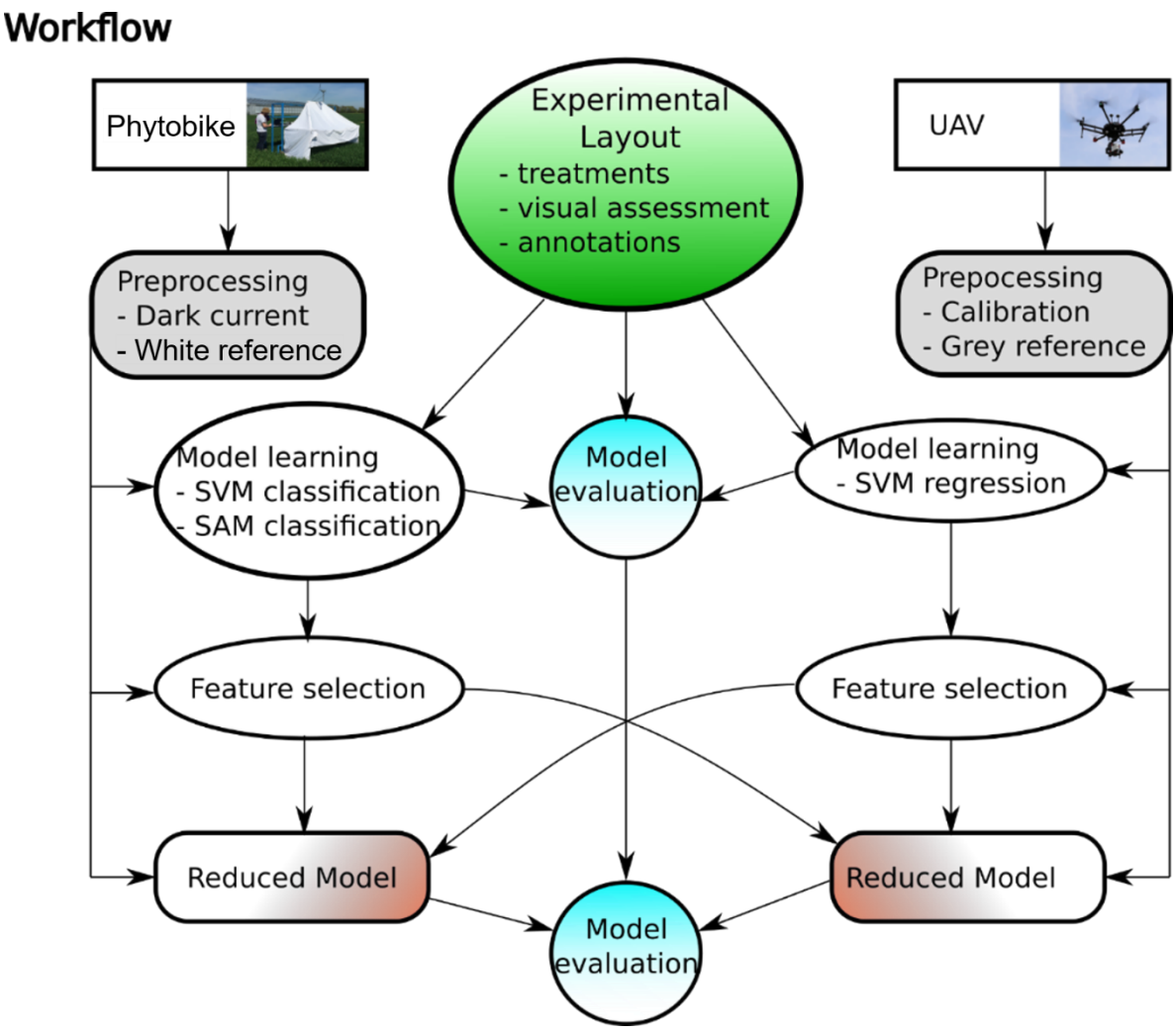

Figure 4. Underlying workflow of data assessment to compare different prediction algorithms and evaluating the value of information about selected features at different scales.

Spectral preprocessing

The derivation of the physical surface property reflectance from observed intensity observations is an essential part of hyperspectral image processing. The normalization procedure has to be adapted to the measurement platform and is based on a spectral reference panel with a known homogeneous reflectance in the observed wavelengths. At all scales, the following equation was applied to calculate the Reflectance *R* from the observation *Im,* reference Im_{ref} and the corresponding dark currents DC_{Im} and DC_{ref}. In the field, the additional DC_{ref} has been omitted due to practical reasons.

$$R = \frac{\Im - DC_{\Im}}{\Im_{ref} - DC_{ref}}$$

On the ground canopy scale, a 50 % spectral reference panel has been measured within each image of the line scanner. A separate dark current has been observed for the Specim V10E camera before every image. Due to practical reasons, UAV flight sequences were started with the acquisition of a single Dark Current and one image of the reference panel immediately before and after flying the frame based Rikola camera over the wheat plots. Image quality always suffers from motion of the object to be measured or motion of the sensor. To avoid this images were taken in conditions as calm as possible on the ground canopy scale. The Rikola camera was hoovered for at least 10 images over the reference panel to ensure that image quality is sufficient for data normalization. The use of cross sensor normalization, e.g. by using a separate spectrometer that is continuously logging the incoming light intensity has been tested but was not successful due to a deviating response characteristic between the different sensors.

To remove high frequency noise at the spectral border regions of the Specim V10e, the bands 1-20 (400-450 nm) and 181-211 (910-1000 nm) have been excluded from further analysis resulting in 161 used spectral bands. In addition, a Savitzky-Golay filter using 15 centered points and polynomial of degree 3 has smoothed the data of the Specim V10e.

Data normalization

The plant geometry can perform severe distortion due to varying leaf angles, leaf distances to the camera and specular reflections on particular parts of the leaves. To compare the reflectance characteristics omitting the additive and multiplicative factors, the Standard Normal Variate (SNV) has been developed [33]. It is able to remove scaling factors due to

varying distance or leaf angle as well as additional factors like specular reflection, e.g. on leaf tips. The normalization was performed both on ground canopy and field data. The *SNV* representation was calculated per spectrum *S* and focuses the shape of the spectral curve:

$$SNV = \frac{S - mean(S)}{std(S)}$$

Prediction algorithms

Multiple algorithms can perform predicting a class or continuous value based on features of a sample. In general, they use a vector representation as input. In this study, the classifiers Spectral Angle Mapper and Support Vector Machine as well as the regression algorithm Support Vector Regression are applied on ground canopy data (taken with the phytobike). To train and evaluate the models, four images of one measuring day were annotated to be used as training data and four images were annotated to be used as test data. The amount of annotated pixels differed in the different images due to natural heterogeneity in the crop stand. Pixel numbers were at least several thousand for each class up to several hundred thousand pixels for all classes in one image. Based on the huge amount of annotated pixels, a model was trained on a subsampled data set, to make it trainable and to rebalance the classes. With the exception of the water class, all classes are trained with 1,000 samples per class after subsampling of training data. The spectral angle mapper (SAM) was used because in literature it is described to work resiliently under inhomogeneous light conditions [34]. The development of the classification model is easy and fast. The support vector machine (SVM) was used because of the fact, that in theory it is trained on the whole dataset and considers the spectrum of each pixel as training data. Vegetation indices (VI's) were used because various published works focused on VI's as tool for disease detection. VI's can be seen as established representatives for optical measurements of plant parameters. The models were trained using three data representations: full spectra, SNV normalization and 20 spectral VI's. The results can be compared to a SAM that represents the base line accuracy. The comparison is performed on the YR test data from 23rd May 2018. The evaluation of different feature representations shows a small advantage of SNV normalizations, whereas it is treated as standard representation in the following. As performance measures, we applied the overall accuracy using six classes for the model, combining the background and the old leaves/straw class. Furthermore, we evaluated the F1 score (Table 1) for the class disease providing a

homogenized combination of precision and recall. The F1 score declares the amount of pixels of one class that is correctly classified into this class after the formula 2*((precision*recall)/(precision+recall)). The two performance measures correspond in the tendency, however the F1 score decreases faster as the large amount of background pixels stabilizes the overall accuracy.

Spectral angle mapper

The SAM is a prediction algorithm, developed for an efficient classification of high dimensional spectral data. The assignment is based on the angle between the spectra to classify and reference spectra, treating a spectrum as high-dimensional vector [34]. The spectrum to be classified was assigned to the reference spectrum/class with smallest angular distance. In addition, a threshold prohibits an assignment of spectra with a large angular distance.

Support vector algorithms

Support Vector Machine classification (SVM) as well as Support Vector Regression (SVR) are established machine learning methods that have proven to deal well in situations with many features but a very limited number of samples [35]. This is a common situation in hyperspectral data analysis and following it is a suitable approach for hyperspectral remote sensing as well as close range imaging. A critical point for the application SVM and SVR is the selection of the hyper parameters Cost *C*, kernel parameter *γ* (SVM) or *C* and complexity control *v* (*v*-SVR). They were selected by grid search combined with a cross validation. Grid points were $10^{-5} \dots 10^{10}$for *C*, $10^{-8} \dots 10^{2}$ for *v* and $0.05 \dots 0.50$ for n. Optimization algorithm was SMO and as implementation LIBSVM 3.18 has been used with Matlab [36].

Vegetation indices

On hyperspectral images on ground canopy data 20 VI's were tested to visualize crop heterogeneity and to detect yellow rust in the field. The composition was used because it was successfully tested as indicator for crop vitality [37]. The composition of VI's was chosen according to [37]. Due to the limitation of available bands of the Rikola camera, for UAV data only 16 VI's were used and the ARVI, mRESR, mRENDVI and SIPI were excluded.

Model evaluation

To compare the performance of the different models on the respective data sets different measures have been applied depending on the model type. All measures have been calculated

on test set that has not been used in training. For classification models, that determine the discrete classes y as a function f(X) of the data X, the accuracy is defined as the percentage of correctly classified data points. The f1-score in contrast, is based on the precision and recall of each class. In Regression tasks with continuous target variables, the coefficient of determination R^2, Correlation and Root Mean Square Error (RMSE) is applied. Due to the limited amount of data we applied the Leave-one-out cross validation to generate the test predictions. This procedure learns a model on the whole data set except one sample. This is repeated for all samples in the data set.

Feature selection

There are multiple approaches for feature selection, feature subset selection and feature weighting. Filter approaches like Relief are very fast and provide a weight for each feature. In contrast, wrapper approaches have the big advantage to deal well with high levels of redundancy and to select the best subset with minimal size [38]. Major drawback is the high computational load. Feature selection at all scales (on ground canopy and UAV images) has been performed by a Wrapper approach comprising a SVM or SVR, respectively. A sequential forward feature selection (Statistics Toolbox, Matlab2013a) has been used whereas the called criterion function minimizing the prediction error has been implemented based on LIBSVM 3.18. For the SVM the accuracy has been maximized and for the SVR the RMSE has been minimized. Due to the limited number of samples in the UAV dataset a leave one out cross validation has been performed to generate the test predictions to calculate the criterion.

Spatial resolution as key parameter for disease detection

Beside relevant wavelengths, the required spatial resolution or ground sampling distance (GSD) is highly important for the definition of a sensor capable to detect different wheat diseases in the field. Based on the Test and Training data sets, simulations have been performed where the test data has been extracted from subsampled spectra by a factor of 2, 10, 20 and 100. A knn and an aggressive subsampling approach were compared to visualize the effect of different annotation strategies on the F1-score for the detection of YR.

6.4 Results and discussion

Supervised classification of hyperspectral pixels at the ground canopy scale

One approach to analyze the hyperspectral data on the field scale is the pixel-wise classification into usual pixel (background, straw, healthy leaf tissue) and in disease specific symptoms. In the field experiment 2018, YR had a significant disease severity and classifiers for this disease were derived.

The use of 16 VI's reached a reasonable but not competitive performance. However, it has to be noted that we compare 161 features to 16 features meaning a significant reduction in dimensionality. The results can be integrated in a later discussion of the various feature sets obtained by feature selection.

Based on these results, SVM SNV (Table 1) has been selected as most appropriate approach. A visual comparison of the SAM results and the SVM SNV result is shown in Figure 5. Significant differences are apparent. The SVM detects much more senescent leaves, e.g. all leaves from the lower leaf levels whereas the SAM assigns these to the background or the healthy leaves. The SVM is more sensitive for ear detection that cause major problems in the SAM image, where they are partly assigned to YR. Overall, both approaches are sensitive to YR but the SVM is much more accurate in the very bright image parts as well as the darker background part while in the SAM classification the class YR is overrepresented. The visually most significant aspect is the large number of blue pixels in the visualization of the SVM result. YR disease was present at all leaf levels and led to an early senescence in lower leaf levels.

Table 1. Comparison of evaluation parameters obtained on test data for different data representations and prediction algorithms on ground scale for Support Vector Machine (SVM) and the Spectral Angle Mapper (SAM).

	SVM Raw	SVM SNV	SVM Indices	SAM
Accuracy	91.9%	92.9%	90.2%	81.4%
F1 score disease	83.2%	84.0%	76.4%	48.3%

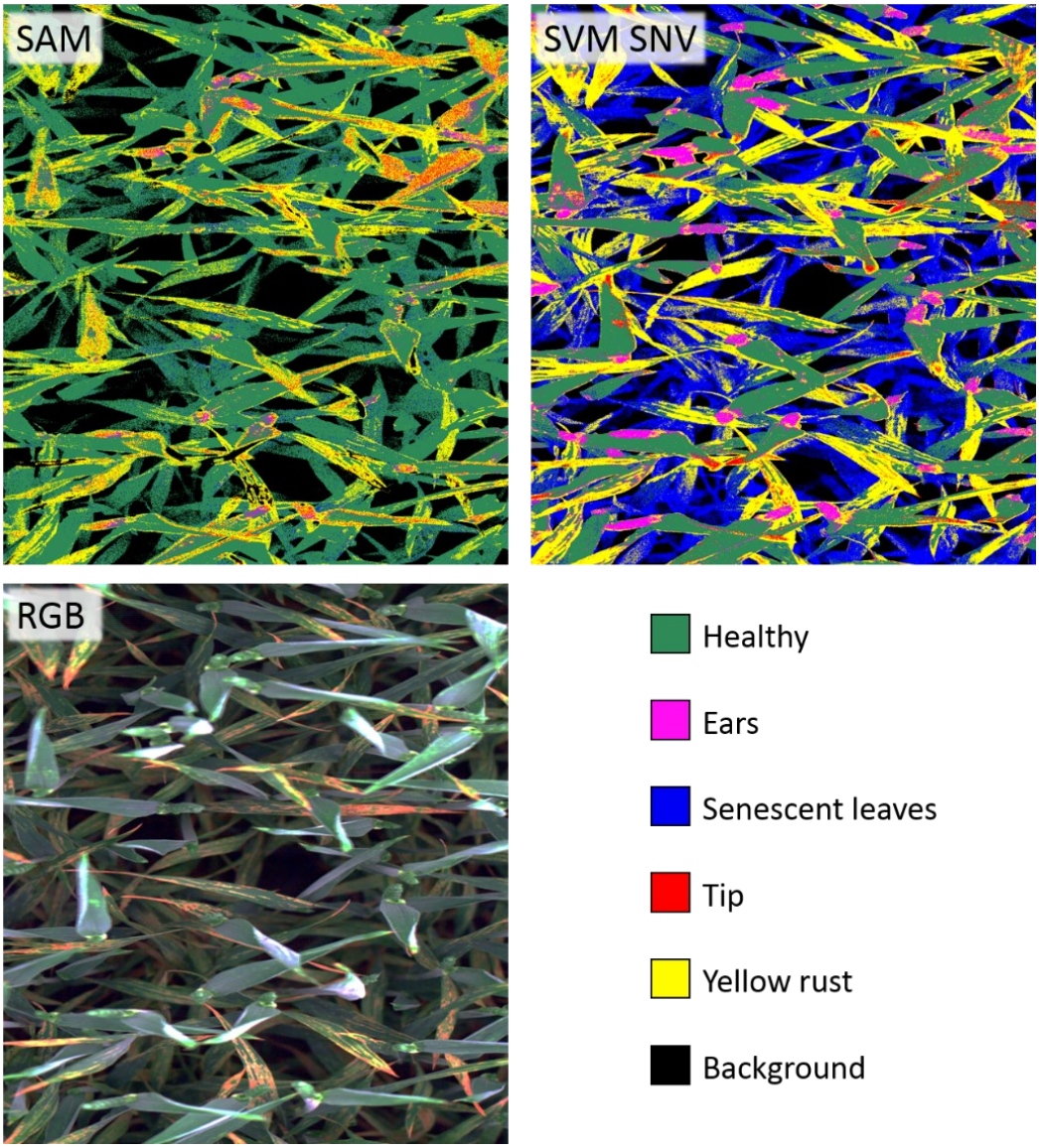

Figure 5. Visual comparison of representative Spectral Angle Mapper (SAM) and Support Vector Machine Standard Normal Variate (SVM SNV) results for the same ground-based image of one representative measurement location of a plot inoculated with YR and the RGB visualization of the hyperspectral camera. Classes were generated from manual annotation of train and test data.

The classification models have been validated following two approaches: (1) Pixel-wise classification of the hold-out test data set consisting of manually annotated pixels of new images of separate plots and (2) prediction of pixel-classes of all images obtained at a respective day and comparing the total % disease class from all plant pixels to the visual assessment done by the expert (Fig. 6). (1) results in a confusion matrix allowing to calculate multiple performance measures such as the overall accuracy, the sensitivity and the recall, whereas (2) provides R^2-value, correlation coefficient and a regression plot. Table 1 shows the overall accuracy and the F1-score for the different classification methods.

Presumably, due to light reflections and transmission or a deviating weighting of the different canopy levels, the SVM prediction overestimates the ratio of diseased pixels. To compensate this, a linear regression model has been applied. However, deviations between the predicted disease severity and the visual assessment can have various reasons, e.g. the section of the plot observed by the sensor does not represent the true status that is evaluated by the visual assessment. The viewing angle produces a variable composition of different leafs and leaf layers in the field of view of the human and the sensors. Furthermore, the visibility of lower leaf levels is low for imaging system from the top and more accurate if the human rater can go deep into the crop stand for individual leaf disease rating. Further points are that the visual assessment produces a single value averaging the affected leaf area. At repeated disease assessments with multiple experts, different deviations have been observed depending on the literature [39, 40]. The method of disease detection is subjective to the individuals performing the assessment. Another prime factor for deviations and classification inaccuracies is the biological heterogeneity. This has to be considered as highly dynamic within one field, one plot, and one location and even on different leaf layers and single leaves. The biological heterogeneity can be affected by many factors e. g. the leaf color and status, stem elongation (distance of leaf layers), the density of the canopy and other biological growth processes.

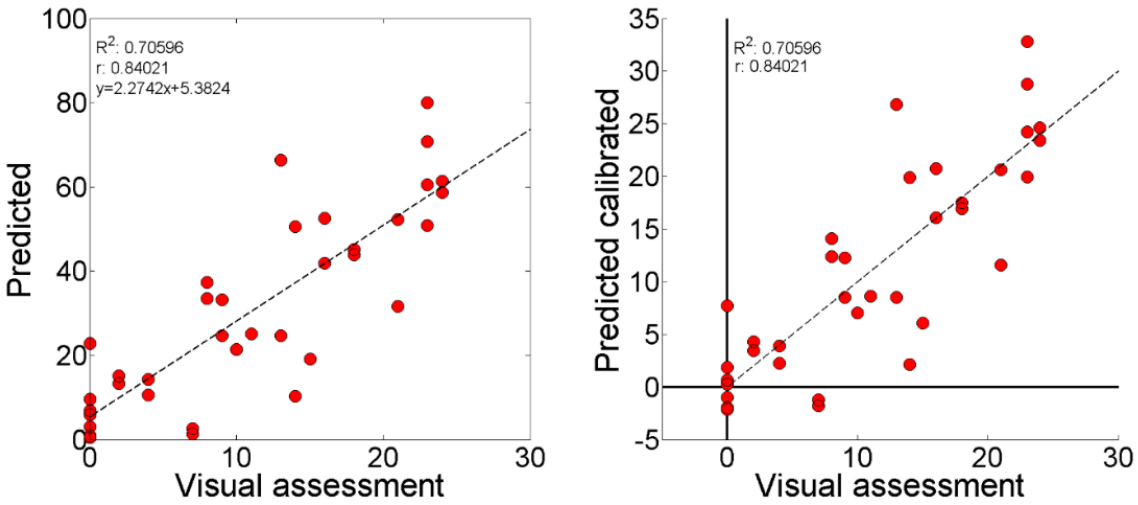

Figure 6. Scatter plot of the relation between visual assessment and predicted disease ratios for Yellow rust on 23rd of May 2018 before and after application of a linear calibration model. The calibration model has the purpose to compensate scale differences in the prediction values.

Evaluation of hyperspectral UAV observations using a filter-system hyperspectral camera

To characterize the reflectance characteristics of field plots, spectra of the central 4 x 2 m of each plot have been averaged. Intra-plot variations were neglected. Multiple traits have been predicted with reasonable accuracy based on SVM and SVR analysis of the 55 recorded bands from 500-900 nm. Tab. 2 shows the obtained performance parameters based on a SNV representation and the integration of all 55 bands.

Using the SVR approach, a prediction of the disease severity in percent was possible with reasonable accuracy (Fig. 7). The interpretation of this result has to take into account that a value from the visual assessment might not represent the average plot value because diseases may occur at zoned locations in the plot and assessment locations may be in these spots or not.

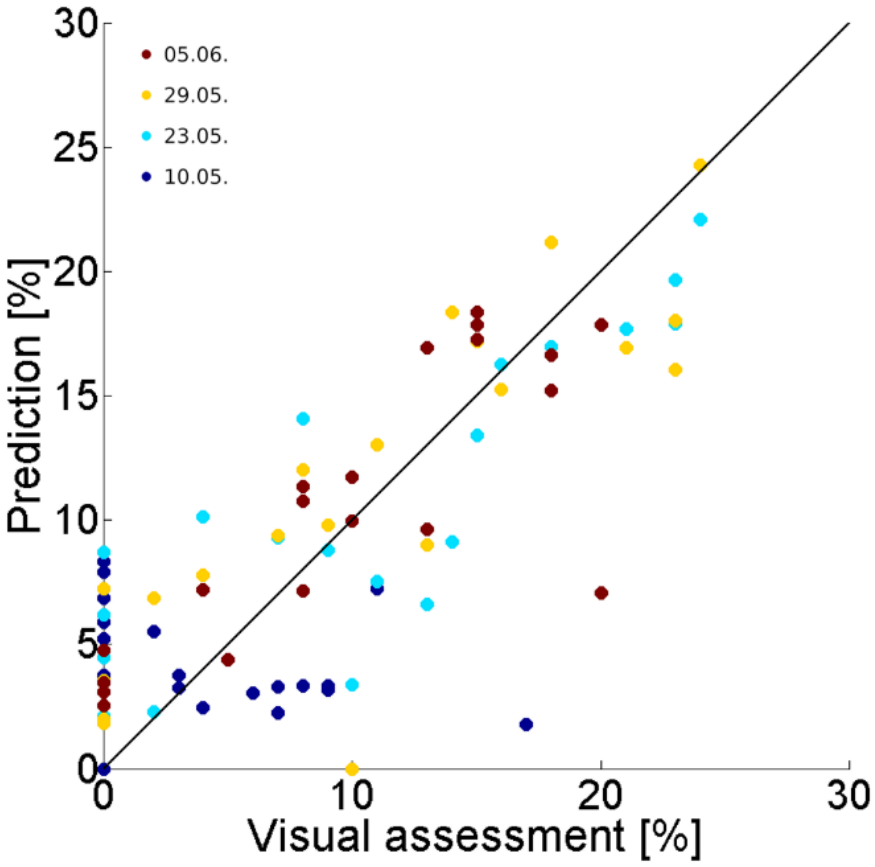

Figure 7. Prediction results of a YR infestation obtained by a leave-one-out procedure of the Support Vector Regression (SVR) on the UAV scale. Each point represents a plot observation and its color the observation date (DD-MM).

Table 2. Performance values for different SVM and SVR models predicting the treatments of the wheat field experiment based on UAV observations.

TRAIT/TREATMENT	PERFORMANCE
Fertilizer level	Accuracy = 82.3%
Fungicide	Accuracy = 91.5%
Fungicide + Fertilizer level (4 classes)	Accuracy = 71.4%
Disease Detection (severity > 0)	Accuracy = 90.0%
Disease severity estimation	Correlation = 70.6%

Selection of relevant features at different scales

One of the main motivations for the application of hyperspectral imaging technology is the potential to find the most relevant wavelength for a specific task and to subsequently design a specific sensor. [41] showed that specific wavelengths might be useful to identify certain leaf diseases in sugar beet. In wheat, VI's are described that are capable in detecting brown rust [18]. This shows that a selection of specific wavelengths can be specific for one disease. We applied the introduced technique to data sets on ground canopy and UAV scale and derived important wavelength for the detection of disease symptoms as well as the prediction of disease severity.

Ground scale

Feature selection on field scale has been performed for the detection of YR. The models were trained on a homogenized sample of training data and validated by a five-fold cross validation. The final accuracy has been determined on the hold-out test set. To reduce the computational complexity, the feature has been regularly subsampled by a factor of 5. The resulting 33 bands have been ranked and an optimal band number has been selected (Fig. 8).

For YR an optimal number of 16 features reached 91% accuracy. However, to allow a comparison with the UAV scale selection, we selected the best 10 features providing an accuracy of 88%. The waveband of 780 nm in the NIR is the most important for YR detection.

The next two bands are also in in the NIR, followed by a band in the blue/green spectral region. Less important is the NIR >800 nm and the red part of the spectrum. Various works showed that VIs using wavelength out of these spectral regions can be successfully used to detect rust diseases of wheat [17, 18, 25] or even for necrotrophic diseases of other crop plants such as groundnuts [42]. In literature it is described that pigments and water influence the absorbance and reflectance of light with plant interaction [43-45]. The measured reflectance signal is always a mixed signal and the result out of complex biochemical interactions [43, 46, 47]. The visible region is mainly influenced by the light absorption of leaf pigments [48]. Healthy wheat canopies appear dark green because of high amounts of chlorophyll in the leaves [10]. With YR infection in the leaf tissue a degradation of chlorophyll happens while the urediniospores of rust fungi are pigmented through the formation of carotenoids [49]. This could explain the importance of certain absorption or reflection bands of pigments for YR detection in the visible range. The effect of chlorophyll degradation and formation of chlorosis and a thereof resulting detectability for the disease is also described for septoria tritici blotch [28]. The NIR region is strongly influenced by the leaf and cell structures, the architecture of the canopy and water absorption bands [43, 50]. High YR incidence leads to an early senescence of leaves in the upper but particularly in the lower leaf levels. This changes the appearance of the crop architecture, reduces the vitality of leaves and water content and could result in the importance of specific wavebands for YR detection.

UAV scale

For the feature selection on UAV scale the detection and quantification of YR infections has been investigated. Using the UAV and the filter-system Rikola hyperspectral camera, the mean spectrum of the central part of each plot has been measured at multiple days. The first four dates have been used as later a suitable disease estimation has not been possible due to the starting senescence.

The optimal number of features was 11 features, reaching an RMSE of 17.9 (i.e. to the visual assessment at the ground of around 70 %) (Fig. 8). Here the most important bands were 830 nm and 510 nm followed by NIR bands. Without significance are the red region 630-700 nm and the beginning of the NIR 700-800 nm. The selection of the spectral border band would be a sign of fitting to noise if the Specim V10E line scanner has been used, but here the Rikola camera has been used without an increased noise at the spectral border regions.

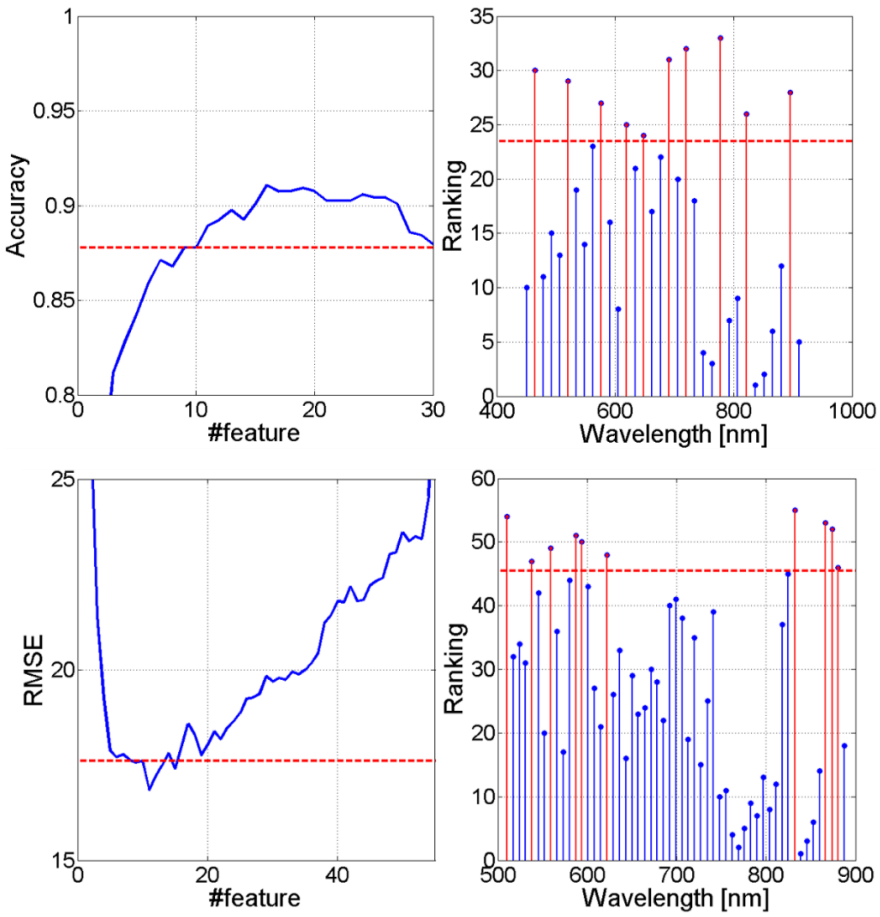

Figure 8. Result of the feature selection for the classification of YR in the field on ground (top) and UAV (bottom) scale. The reached accuracy for the different amounts of features (left) and the ranking of the inclusion within the feature subset (right).

Feature selection results for further traits are shown in Table 3. Also here, important bands are in the green and NIR region which might be triggered by the same biochemical reactions as on the ground scale. However, for the fertilizer, fungicide and the combined treatment the spectral region 600-750 nm had a higher relevance.

Table 3. The six most important bands for selected plot traits at the UAV scale and ranking of the wavebands (in nm) for importance of feature selection beginning with the highest. Selected traits: Fertilizer (Fert), fungicide (Fung), fungicide + fertilizer, yellow rust (YR) detection, yellow rust regression.

Ranking	Fert	Fung	Fert+Fung	YR Detection	YR Regression
1	767	727	734	797	832
2	725	804	887	881	510
3	648	762	545	601	867
4	557	648	559	706	874
5	627	594	517	874	587
6	704	767	748	594	594

Cross-scale interpretation

The cross-scale interpretation reveals significant inconsistencies but also parallels. The inconsistencies are related to sensor characteristics as not always the same sensor has been applied. Furthermore, additional factors at the different scales (leaf geometry, mixed pixels with background) are included at the higher scales that may rely on further bands to be regarded properly by the prediction model.

The number of required features varies at the different scales. In a separate experiment (data not shown) with fixated leaves in the laboratory, a perfect differentiation was possible using two bands. Geometry is also not relevant as the leaves are fixated in horizontal position. The highest number is required on field scale by 18 on average as here the complex geometry and complex scattering effects in the canopy affect the recorded signal. At the UAV scale the geometry is the same but due to the physical smoothing by blur and high pixel size, the signal has been simplified again. There an optimum is reached at 11 omitting the spectral region 620-820 nm.

The red region had a low relevance for the classification of YR on the field and UAV scale. This might be due to the fact that urediniospores *P. striiformis* appear more yellow than red (due to carotenoid composition) and do not show strong reflection in the red region. The NIR region

had an increased relevance on the UAV scale. Presumably this is related to the simple separability based on pigments on the lower scale whereas in the field the leaf geometry distorts this signal and the NIR region is required to compensate this effect.

The differences and parallels of the different feature sets motivated the cross-scale application of feature sets. It is assumed that information about optimal feature sets can be an advantage also at a different scale. Therefore, the feature sets for the assessment of YR are exchanged between the ground scale with the Specim V10 and the UAV scale with the Rikola hyperspectral camera. To allow a comparison of the different feature sets, the number of included features is fixated to 10 based on the previous feature selection runs (Fig. 8). Evaluation at ground and UAV scale are performed following the same principle as in the feature selection. Table 4 shows the performance of multiple feature sets. The highest accuracy is reached by the full data set, followed by the 16 VI's. The feature sets with 10 features reached a slightly lower but in direct comparison very similar accuracy. The results indicate that the complex situation in the wheat canopy request for more than 10 features. The good performance of the equidistant feature set can be explained by the resemblance to the 10 selected features that are nearly equidistant distributed over the spectral range. Both feature sets apply wavebands out of the same spectral regions. Furthermore, the performance of the field selected feature set points to the heterogeneity of reflectance characteristics, even in the same treatment group. The test and training data have been extracted from separate image sets. Following, this feature set has been optimized on the training data but has no advantages compared to the equidistant feature set on the test data.

The comparison of different feature sets shows the potential positive results of a feature selection to a higher degree. The highest accuracy was obtained by the feature set optimized at UAV scale whereas the feature set from the ground scale obtained an even lower performance than the equidistant feature set (Table 5). For the UAV data set a separation in test and training data was not possible due to the much smaller data base. Here, a leave-one-out cross validation has been applied to obtain R^2 and correlation coefficients. The obtained feature set may be more adapted to the evaluation procedure at the UAV scale compared to the ground scale. The UAV evaluation shows that it is possible to slightly increase the accuracy by feature selection compared to the full data set and also that uninformed subsampling does not lead to optimal results.

Table 4. Performance of the different feature sets for the YR detection based on ground observations.

Ground class.	All	*UAV select*	*Field select*	*Equidistant*	*VI*
# feature	210	10	10	10	16
Acc.	92.9%	87.4%	88.9%	89.2%	90.2%
F1 disease	0.84	0.694	0.751	0.732	0.764

Table 5. Performance of the different feature sets for the YR regression based on UAV observations.

UAV regression	All	UAV select	Field select	Equidistant
# feature	55	10	10	10
R^2	0.63	0.69	0.57	0.61
Corr.	79.4%	83.0%	75.5%	78.1%

However, the data characteristics at the ground canopy and the UAV scale are so disparate that an advantage of feature set transfer is doubtful. The transferred feature set reached a lower performance even compared to the uninformed equidistant sampling. There are multiple factors contributing to the deviating data characteristics expressed by different demands to the feature sets. One of the main points will be the use of different sensors with different measurement principles, each adapted to its measurement scale. The noise characteristics of the ground camera shows an increased noise level at the spectral border regions and a noise optimum in the red range. The UAV camera shows a homogenous measurement quality for the whole range, despite some artifact bands around 630 nm, where optical refractions seem to occur at a beam splitter. The suitability of a spectral region can be significantly reduced by such sensor characteristics but if the effect occurs only at one sensor, the optimal feature set changes. Further points regard the implicit spatial smoothing if a larger area is captured by a single pixel. At the ground scale, the feature set will directly point to the reflectance characteristics of the spores, whereas at the UAV scale the reduced vitality and even morphological changes have to be taken into account. In contrast, the close-range

observations at ground scale are dominated by the leaf geometry, more specific by leaf angle and position within the crop stand. Therefore, the analysis model has to integrate these factors to enable predictions as robust as possible against the plant geometry. At the UAV scale, most of the pixels provide a mixed signal of multiple leaves and in addition, the analysis is performed on the mean spectra of each plot. Most of the geometric effects average out as the characteristics of hundreds of leaves are averaged.

In general, there is no single waveband for individual diseases, respectively, but broad regions (blue, green, red, NIR I (700-800 nm), NIR II 800-1000 nm) with a varying relevance for the different diseases. This is tightly coupled with the sensor characteristics. The Rikola camera is not able to measure the blue and NIR (900-1000 nm) but provides stable noise conditions over the whole measurement region. The Specim V10E camera has a larger measurement region (400-1000 nm) but the spectral border regions have a much higher noise level.

Spatial resolution as key parameter for disease detection

The un-sampled data have a GSD of approximately 0.4 mm (for Specim as well as Rikola). The UAV observation (20 m flight height) have a GSD of approximately 8 mm (Fig. 9).

This approach does not regard the adaptation of the model to the new classification scale. By retraining the prediction, the accuracy may be improved as also here the smoothing affects the data characteristics. However, even then the disease specific information will vanish at a certain level. We omitted this evaluation as the performance measures of the retrained models are not comparable anymore as the amount of training data declines drastically, e.g. to around 100 samples for YR at higher subsampling scales.

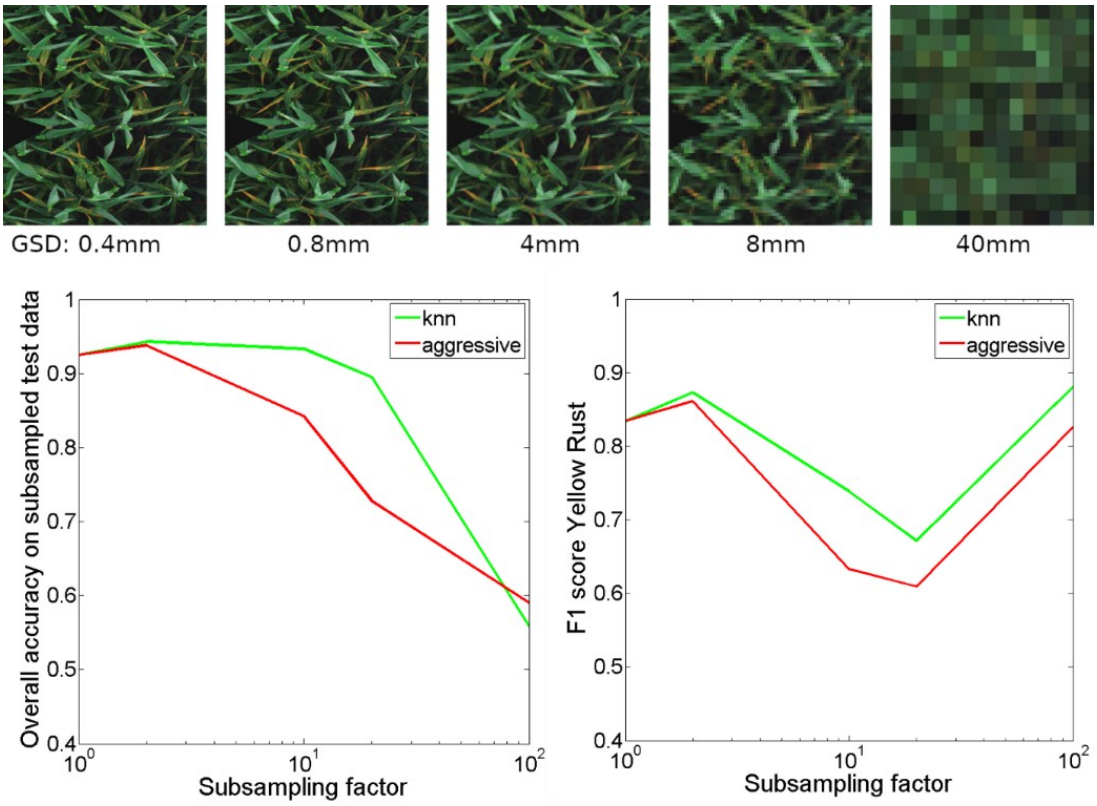

Figure 9. Visualization of spatial subsampling effects for the four investigated subsampling levels (images) and the effect of scale on accuracy and F1-score for the two different approaches knn (nearest neighbor) and an aggressive for subsampling the annotation.

The investigations allow to define a minimal sampling distance at which the mixed information does not allow to predict plant diseases any more. Without retraining the model, the accuracy decreases at subsampling factors of 10 and 20, respectively. A low subsampling of 2 seems to have no negative effects. Presumably, the included smoothing removes border cases and outliers which are hard to classify correctly. At higher subsampling levels, more and more mixed pixels occur where the aggressive label subsampling tends to extend the image regions assigned to a class. Following the effect is here more severe. The accuracy of more than 50% at the final state is related to the dominant background which provided a significant majority of test data at the high subsampling levels. It is not related to the ability to predict the presence of YR. This is performed by the F1-score, a measure to quantify the performance of a multi-class prediction model on class level.

Also in this performance measure, the quality decreases at subsampling factor of 10. Surprisingly, the F1-score increases to near to optimal numbers at a subsampling factor of 100. Discussing this fact, it has to be noted that at the highest subsampling factor only 119 YR

samples are included in the data set, which are all correctly classified. Maybe this is related to the accuracy on UAV scale where the majority of geometric effects is averaged out. This point has to be evaluated in further investigations but it seems that subsampling by a factor of 100 removes the leaf structure completely, whereas at a lower subsampling factor the leaf structure is still apparent but more and more effects of mixture become present. Without any leaf structure the classification problem is simplified to the presence of YR within this part or even within the image. At low level disease severities this will cause major problems but here, the test data has been selected to show clear disease symptoms.

Optimal sensor system for plant disease detection

Two sensor systems have been evaluated, both showing strengths and weaknesses. In direct comparison, the flying sensor system has strong advantages in usability, throughput and commercial viability. The ground sensing system is much more sensitive as a single symptom with a diameter of a few mm can be recorded. Such a spatial resolution can be obtained by the flying system only at a flight altitude of around 1 m above the canopy. However, with the used system it is not possible, as the downstream from the rotors would strongly move the canopy. Alternatively, an optical zoom has to be applied presumably reducing the light flux as well as the throughput of the overall system. This could be compensated by an increased spatial resolution of the sensing array.

Summarizing, based on the experiences made during the presented study, we propose to focus on a UAV flying in low height in combination with a frame-based spectral camera sensing in around 15 equally distributed bands. A tunable band configuration would be an alternative that uses bands optimized for every single disease scenario, i.e. crop species, crop developmental stage, assumed disease setting, assumed symptom maturity. The spatial resolution should be at around 1 mm GSD, a value that allows to detect small symptoms but neglects high-frequency noise caused by the complex surface structure of plants [51, 29].

6.5 Conclusion

This study investigated the detection of plant diseases using hyperspectral cameras at ground and UAV scale. In this context, the appropriate data analysis is decisive to reach suitable results. Supervised classification has the advantage to separate disease related signals from a huge amount of natural biological, geometrical and sensor-related variability within a hyperspectral image of a crop canopy in the field. We proved that hyperspectral imaging in

combination with supervised classification and regression showed good accordance to visual assessment at the ground. This allows to address questions regarding the transfer of information between different scales and sensors. We showed that a feature selection is able to increase the prediction accuracy if it is performed on the analyzed data set. In contrast, scale or sensor transfer of selected feature sets was not successful and even less predictive than an uninformed regularly sampled feature set. This highlights the importance of a precise specification of a prediction task by representative data samples. Deviations in data characteristics can significantly impair the performance of a data analysis pipeline or a tailored sensor in real-life applications.

This study sets the basis for ongoing research. New, upcoming sensors fulfilling the demands defined in this study may cope also with the current disadvantages. Consequently, there is a high probability to realize the defined flying sensor system with high resolution spectral camera, computing capabilities and self-localization. Adapted legal conditions would allow an integrated system of field managing software, remote sensing based predictions and current observations from the field using an automatized UAV.

6.6 Acknowledgements

The authors would like to thank Onno Muller (Research Center Jülich, Germany) for providing the basic Phytobike frame, Dr. Thorsten Kraska for general support at Campus Klein-Altendorf and Winfried Bungert (Campus Klein-Altendorf, Germany) for implementation of cultivation measures during the vegetation period.

6.7 References

1 West, J.; Bravo, C.; Oberti, R.; Lemaire, D.; Moshou, D.; McCartney, A. The potential of optical canopy measurement for targeted control of field crop diseases. *Annual Review of Phytopathology* **2003**, *41*(1), 593-614.
2 Hillnhütter, C.; Mahlein, A.K.; Sikora, R.A.; Oerke, E.C. Remote sensing to detect plant stress induced by *Heterodera schachtii* and *Rhizoctonia solani* in sugar beet fields. *Field Crops Research* **2011**, *122*, 70–77.
3 Bravo, C.; Moshou, D.; West, J.; McCartney, A.; Ramon, H. Early disease detection in wheat fields using spectral reflectance. *Biosystems Engineering* **2003**, *84*, 137-45.
4 Mewes, T.; Franke, J.; Menz, G. Spectral requirements on airborne hyperspectral remote sensing data for wheat disease detection. *Precision Agriculture* **2011**, *12*, 795-812.
5 Mirik, M.; Jones, D.C.; Price, J.A.; Workneh, F.; Ansley, R.J.; Rush, C.M. Satellite remote sensing of wheat infected by Wheat streak mosaic virus. *Plant Disease* **2011**, *95*, 4–12.

6 Gebbers, R.; Adamchuk, V.I. Precision agriculture and food security. *Science* **2010**, *327*, 828-831.
7 Mahlein, A.K.; Kuska, M.T.; Behmann, J.; Polder, G.; Walter, A. Hyperspectral sensors and imaging technologies in phytopathology: State of the art. *Annual Review of Phytopathology* **2018**, *56*, 535-58.
8 Wahabzada, M.; Mahlein, A.K.; Bauckhage, C.; Steiner, U.; Oerke, E.C.; Kersting, K. Plant phenotyping using probabilistic topic models: Uncovering the hyperspectral language of plants. *Scientific Reports* **2016**, *6*, 22482.
9 Whetton, R.; Hassall, K.; Waine, T.W.; Mouazen, A. Hyperspectral measurements of yellow rust and fusarium head blight in cereal crops: Part 1: Laboratory study. *Biosystems Engineering* **2017**, *166*, 101-15.
10 Whetton, R.; Waine, T.; Mouazen, A. Hyperspectral measurements of yellow rust and fusarium head blight in cereal crops: Part 2: On-line field measurement. *Biosystems Engineering* **2018**, *167*, 144-58.
11 Mahlein, A.K. Plant disease detection by imaging sensors - parallels and scientific demands for precision agriculture and plant phenotyping. *Plant Disease* **2016**, *100*, 241–51.
12 Thomas, S.; Kuska, M.T.; Bohnenkamp D.; Brugger A.; Alisaac, E.; Wahabzada, M.; Behmann, J.; Mahlein, A.K. Benefits of hyperspectral imaging for plant disease detection and plant protection: a technical perspective. *Journal of Plant Diseases and Protection* **2018**, *125*, 5-20.
13 Bravo, C.; Moshou, D.; Oberti, R.; West, J.; McCartney, A.; Bodria, L.; Ramon, H. Foliar disease detection in the field using optical sensor fusion. *Agricultural Engineering International* **2004**, *6*.
14 Franke, J.; Menz, G. Multi-temporal wheat disease detection by multi-spectral remote sensing. *Precision Agriculture* **2007**, *8*, 161–72.
15 Huang, W.; Lamb, D.W.; Niu, Z.; Zhang, Y.; Liu, L.; Wang, J. Identification of yellow rust in wheat using in-situ spectral reflectance measurements and airborne hyperspectral imaging. *Precision Agriculture* **2007**, *8*, 187–97.
16 Lan, Y.B.; Chen, S.D.; Fritz, B.K. Current status and future trends of precision agricultural aviation technologies. *International Journal of Agricultural and Biological Engineering* **2017**, *10*, 1–17.
17 Devadas, R.; Lamb, D.W.; Simpfendorfer, S.; Backhouse, D. Evaluating ten spectral vegetation indices for indentifying rust infection in individual wheat leaves. *Precision Agriculture* **2009**, *10*(6), 459-470.
18 Ashourloo, D.; Mobasheri, M.R.; Huete, A. Developing two spectral indices for detection of wheat leaf rust (*Puccinia triticina*). *Remote Sensing* **2014,** *6*, 4723-40.
19 Cao, X.; Luo, Y.; Zhou, Y.; Fan, J.; Xu, X.; West, J.S.; Duan, X.; Cheng, D. Detection of powdery mildew in two winter wheat plant densities and prediction of grain yield using canopy hyperspectral reflectance. *PLoS ONE* **2015**, *10*(3).
20 Blackburn, G.A. Hyperspectral remote sensing of plant pigments. *Journal of Experimental Botany* **2007**, *58*, 855–867.
21 Gitelson, A.A.; Keydan, G.P.; Merzlyak, M.N. Three-band model for noninvasive estimation of chlorophyll, carotenoids, and anthocyanin contents in higher plant leaves. *Geophysical Research Letters* **2006**, *33*(11), L11402.
22 Roosjen, P.P.J.; Suomalainen, J.M.; Bartholomeus, H.M.; Clevers, J.G.P.W. Hyperspectral reflectance anisotropy measurements using a pushbroom spectrometer

on an unmanned aerial vehicle - results for barley, winter wheat and potato. *Remote Sensing* **2016***, 8*, 909.

23 Moshou, D.; Bravo, C.; West, J.; Wahlen, T.; McCartney, A.; Ramon, H. Automatic detection of 'yellow rust' in wheat using reflectance measurements and neural networks. *Computers and Electronics in Agriculture* **2004**, *44*, 173-88.

24 Zhang, J.; Pu, R.; Huang, W.J.; Yuan, L.; Luo, J.; Wang, J. Using in-situ hyperspectral data for detecting and discriminating yellow rust disease from nutrient stresses. *Field Crop Research* **2012**, *134*, 165-174.

25 Zheng, Q.; Huang, W.; Cui, X.; Dong, Y.; Shi, Y.; Ma, H.; Liu, L. Identification of wheat yellow rust using optimal three-band spectral indices in different growth stages. *Sensors* **2019**, *19*, 35.

26 Azadbakht, M.; Ashourloo, D.; Aghighi, H.; Radiom, S.; Alimohammadi, A. Wheat leaf rust detection at canopy scale under different LAI levels using machine learning techniques. *Computers and Electronics in Agriculture* **2019**, *156*, 119-128.

27 Chen, W.; Wellings, C.; Chen, X.; Kang, Z.; Liu, T. Wheat stripe (yellow) rust caused by *Puccinia striiformis* f.sp. *tritici*. *Molecular Plant Pathology* **2014**, *15*, 433–46.

28 Yu, K.; Anderegg, J.; Mikaberidze, A.; Petteri, K.; Mascher, F.; McDonald, B. A.; Walter A.; Hund, A. Hyperspectral canopy sensing of wheat Septoria tritici blotch disease. *Frontiers in Plant Science* **2018**, *9*, 1195.

29 Behmann, J.; Mahlein, A.K.; Rumpf, T.; Romer, C.; Plümer, L. A review of advanced machine learning methods for the detection of biotic stress in precision crop protection. *Precision Agriculture* **2015,** *16*, 239–60.

30 Camps-Valls, G.; Tuia, D.; Bruzzone, L.; Benediktsson, J.A. Advances in hyperspectral image classification: Earth monitoring with statistical learning methods. *IEEE Signal Processing Magazine* **2014**, *31*(1), 45–54.

31 Lowe, A.; Harrison, N.; French, A.P. Hyperspectral image analysis techniques for the detection and classification of the early onset of plant disease and stress. *Plant Methods* **2017**, *13*(1),80.

32 Singh, A.; Ganapathysubramanian, B.; Singh, A.K.; Sarkar, S. Machine learning for high-throughput stress phenotyping in plants. *Trends in Plant Science* **2016**, *21*(2),110–24.

33 Barnes, R.J.; Dhanoa, M.S.; Lister, S.J. Standard normal variate transformation and de-trending of near-infrared diffuse reflectance spectra. *Applied Spectroscopy* **1989,** *43*(5), 772-777.

34 Kruse, F.A.; Lefkoff, A.B.; Boardman, J.W.; Heidebrecht, K.B.; Shapiro, A.T.; Barloon, P.J.; Goetz, A.F.H. The spectral image processing system (SIPS)—interactive visualization and analysis of imaging spectrometer data. *Remote sensing of environment* **1993**, *44*(2-3), 145-63.

35 Cortes, C.; Vapnik, V. Support-vector networks. *Machine learning* **1995**, *20*(3), 273-97.

36 Chang, C.C.; Lin, C.J. LIBSVM: A library for support vector machines. *ACM transactions on intelligent systems and technology (TIST)* **2011**, *2*(3), 27.

37 Behmann, J.; Steinrücken, J.; Plümer, L. Detection of early plant stress responses in hyperspectral images. *ISPRS Journal of Photogrammetry and Remote Sensing* **2014,** *93*, 98-111.

38 Guyon, I.; Elisseeff, A. An introduction to variable and feature selection. *Journal of machine learning research* **2003**, *3*, 1157-82.

39 Parker, S.R.; Shaw, M.W.; Royle, D.J. The reliability of visual estimates of disease severity on cereal leaves. *Plant Pathology **1995***, *44*(5), 856-64.

40 Nutter, F.W.; Gleason, M.L.; Jenco, J.H.; Christians, N.C. Assessing the accuracy, intra-rater repeatability, and inter-rater reliability of disease assessment systems. *Phytopathology* **1993**, *83*(8), 806-12.
41 Mahlein, A.K.; Rumpf, T.; Welke, P.; Dehne, H.W.; Plümer, L.; Steiner, U.; Oerke, E.C. Development of spectral indices for detectiong and identifying plant diseases. *Remote Sensing of Environment* **2013**, *128*, 21-30.
42 Chen, T.; Zhang, J.; Chen, Y.; Wan, S.; Zhang, L. Detection of peanut leaf spots disease using canopy hyperspectral reflectance. *Computers and electronics in agriculture* **2019**, *156*, 677-683.
43 Gates, D.M.; Keegan, H.J.; Schelter, J.C.; Weidner, V.R. Spectral properties of plants. *Applied Optics* **1965**, *4*, 11– 20.
44 Curran P.J. Remote sensing of foliar chemistry. *Remote Sensing of Environment* **1989**, *30*, 271–78.
45 Heim, R.H.J.; Jurgens, N.; Große-Stoltenberg A.; Oldeland, J.; The effect of epidermal structures on leaf spectral signatures of ice plants (*Aizoaceae*). *Remote Sensing* **2015**, *7*, 16901-14.
46 Carter, G.A.; Knapp, A.K. Leaf optical properties in higher plants: linking spectral characteristics to stress and chlorophyll concentrations. *American Journal of Botany* **2001**, *88*, 677–84.
47 Pandey, P.; Ge, Y.; Stoerger, V.; Schnable, J.C. High throughput in vivo analysis of plant leaf chemical properties using hyperspectral imaging. *Frontiers in Plant Science* **2017**, *8*, 1348.
48 Gay, A.; Thomas, H.; James, C.; Taylor, J.; Rowland J.; Ougham H. Nondestructive analysis of senescence in mesophyll cells by spectral resolution of protein synthesis-dependent pigment metabolism. *New Phytologist* **2008**, *179*, 663-674.
49 Bohnenkamp, D.; Kuska, M.T.; Mahlein, A.K.; Behmann, J. Hyperspectral signal decomposition and symptom detection of wheat rust disease at the leaf scale using pure fungal spore spectra as reference. *Plant Pathology* **2019**, *68*(6), 1188-1195.
50 Elvidge, C.D. Visible and near infrared reflectance characteristics of dry plant materials. *International Journal of Remote Sensing* **1990**, *11*(10), 1775-1795.
51 Kuska, M.; Wahabzada, M.; Leucker, M.; Dehne, H.W.; Kersting, K.; Oerke, E.C.; Steiner, U.; Mahlein, A.K. Hyperspectral phenotyping on the microscopic scale: towards automated characterization of plant-pathogen interactions. *Plant methods* **2015**, *11*(1), 28.

7 Discussion and conclusion

The first main objective of this study (I) was to design measuring setups for hyperspectral sensors to monitor the spectral dynamic of five foliar wheat diseases. **Chapter 2** showed the detailed investigation of the spectral dynamic of the diseases during pathogenesis in time series. The hyperspectral observation of symptom development of five different foliar diseases in one specific crop during disease pathogenesis is a novelty and so far, unique. Few works describe the full spectral characterization of one certain or more diseases during pathogenesis (Mahlein et al. 2012; Kuska et al. 2015; Wahabzada et al. 2015). Mahlein et al. (2012) enabled a link of the histological development of fungal diseases in the leaf tissue, assessed with invasive microscopical methods, with spectral signatures observed using non-invasive hyperspectral measurements. In chapter 2 of the present study, hyperspectral measurements were accompanied by fluorescence microscopic methods to link spectral signatures with biological processes to define disease specific turning points of each pathogenesis. Each turning point represented a certain pathogenesis stage as a spectral fingerprint that is independent from the point in time of infection (because in the field we do not know this point in time) but characteristic for a certain biochemical process of the host-pathogen interaction. These turning points were combined in a spectral library for foliar diseases of wheat.

In the field, the point in time of infection is in general unknown and difficult to consider because the length of the latency phase (time period until first symptoms become visible) depends, among others, on the present weather conditions and the microclimate in the field. With disease forecasting systems, the suitable infection conditions and the theoretical length of the latency phase can be modeled, but a model cannot describe or calculate the absolute inoculum presence and successful infection rates of fungal spores. This is especially true for STB, as a high variability effect of the temperature on the length of the biotrophic latency phase has been described (Lovell et al. 2004). Dugyala et al. (2015) published a rapid protocol for the staining of fungal structures of *Puccinia triticina* in the leaf tissue using fluorescence microscopy. This protocol was adapted individually regarding concentrations of chemical substances for foliar wheat diseases to unveil their presence in the host (Dugyala et al. 2015). Fluorescence microscopy was suitable for monitoring fungal development in the host tissue and to link a spectral shift to a biochemical process in the host tissue. Especially the rust

diseases and powdery mildew (biotrophic diseases) were easily dyed in the tissue. To stain the necrotrophic diseases in the host tissue, higher concentrations (10x) of the dye were necessary. This might be due to the fact that tan spot and STB cause collapse of the plant cells and lead to necrosis (Dushnicky et al. 1998a; Dugyala et al. 2015). The florescence dye binds to chitin (Harrington and Hageage 2003; Harrington 2009; Dugyala et al. 2015) and fungal structures in dead plant cells can hardly be stained due to the lack of water and dye transportation. Another reason could be the role of lignification processes that are part of the host defense (Dushnicky et al. 1998a, Dushnicky et al. 1998b). Fungal structures are capsuled and might not be stained anymore. Chapter 2 favored a better understanding of the development of a spectral signature of a plant leaf under disease pressure and how fungi influence the spectral properties of diseased leaves.

The next objective (II) was to analyze and classify foliar diseases of wheat in hyperspectral images under controlled conditions based on the combined spectral library for the diseases. Hyperspectral measurements are either performed with non-imaging or imaging sensors. Yuan et al. (2014) showed an approach to distinguish between several diseases and insects on winter wheat leaves in the laboratory. The scientists published a non-imaging field spectrometer to distinguish between yellow rust, powdery mildew and cereal aphids. Leaves were collected from wheat fields and analyzed using Fischer's linear discriminant analysis (FLDA) and partial least square regression (PLSR). The overall accuracy (0.75) was not superior but this work presented an interesting approach combining spectral features of different wheat diseases in their analysis (Yuan et al. 2014). Wahabzada et al. (2015) implemented a Simplex Volume Maximization to automatically discover spectral features that are characteristic for a certain barley disease. The scientists detected and distinguished between net blotch, brown rust, and powdery mildew. The SAM results in chapter 2 present especially for the biotrophic pathogens the potential of hyperspectral images for delivering more profound results in disease detection, differentiation and quantification. In this study different approaches from machine learning were used to detect, identify and quantify the different foliar diseases under controlled conditions. Beside the spectral library for wheat diseases, **chapter 2** also shows a disease detection and quantification approach using the spectral angle mapper algorithm in combination with the different disease specific turning points as input training data. Here, it was demonstrated that a spectral library has the potential to serve as basic training data in different algorithms. The diseases were detectable and early and late

symptoms of the pathogenesis could be distinguished from each other. The disease incidence on the leaves was quantified. Non-imaging sensors do not provide the possibility to annotate images as input or training data. To train models for reliable disease differentiation, it might be useful to use imaging sensors that provide pixel-wise spectral and spatial information. Disease detection models learned out of these algorithms might enable an autonomous detection of specific developmental stages of a disease in the field.

In the future, sensors that contain the spectral information for all important diseases of a certain crop should be developed. In European wheat cropping systems STB and YR are the most devastating diseases (Torriani et al. 2015). In other regions of the world different diseases might play a more important role depending on the cropping system and the climate (Oerke 2006). The rust diseases (*Puccinia spp*.) in general are relevant in cropping regions around the world as they are widespread biotrophic diseases. Especially black and yellow rust have a high destructive potential (Dean et al. 2012). In the warmer regions of South Asia the helminthosporium leaf blight, a complex of *Cochliobolus sativus* and *Pyrenophora tritici-repentis*, occurs and might lead to losses up to 30 % and more (Duveiller et al. 2005). If the spectral properties of the relevant diseases could be collected in a detection sensor based on a spectral library for wheat diseases, this sensor could be used ubiquitously in all wheat cropping systems.

Time series measurements with hyperspectral sensors often result in complex data because the data must be comparable over different measurement days to unveil hidden features in the data. **Chapter 3** demonstrates one approach to perform a spatial tracing of disease symptoms back in time series (retrospective analysis) using a non-linear 2D polynomial transformation model. The pixels that are located in a disease symptom at later pathogenesis could be traced back over different measurement days to detect early spectral changes during pathogenesis (by comparing the spectral signatures) using certain reference points and the automatic calculation of different VI's. This approach presents the potential for a hyperspectral disease detection at early time points where the disease is not yet visible for the human eye. This method could be used on images and the automated analysis of big data sets. The spectral signal of the hyperspectral image is still confounded through factors like the leaf geometry and plant architecture (Jay et al. 2016; Bohnenkamp et al. 2019a). Transformation models could be used to recognize marker points in high throughput devices

to gain more information about the spectral changes caused by varying leaf geometry in the canopy or on single leaves during time series. High throughput devices offer the possibility to gather huge data sets with hundreds of individual plants that are measured up to several times a day during long time periods (weeks) under homogeneous conditions. Additionally, this approach is promising for early detection tests under controlled conditions in low throughput tests but also in high throughput facilities.

Chapter 4 showed a decomposition of the spectral signatures of wheat leaves infected with the rust diseases YR and BR based on the spectral information of pure spore spectra of *P. striiformis* and *P. triticina*. The main idea was to use the specific spore spectra to unveil the spectral fingerprint of the disease in the signal of a diseased plant leaf. A plant leaf always represents a mixed signal due to the combination of different biochemical compounds in different leaf layers. The decomposition was performed using a least-squares factorization. The study indicates that a least-squares factorization can be used to decompose hyperspectral mixed signals of plants for unveiling the spectral fingerprint of a plant disease. The spectral signal of a diseased leaf is always a mixed signal (Bohnenkamp et al. 2019b). Different components, such as water and cellulose, have a different spectral absorption and reflectance areas (Elvidge 1990). Future studies should therefore fragment the mixed spectral signal into its pure components and properties of the host-pathogen-interaction to achieve a deeper understanding of the plant physiology itself.

But not only plant disease can be distinguished from the healthy plant. Even different symptom types of the same disease can be distinguished from each other based on the pathogen or plant genotype (Mahlein 2016). Leucker et al. (2016) showed that different genotypes of sugar beets can be differentiated from each other by the individual peculiarity of Cercospora leaf spots. Depending on the scale, the scientists were able to fragment a leaf spot into three different zones depending on the sporulation intensity of the fungus (Leucker et al. 2016). These deep insights into the submillimeter scale indicate future approaches for the effort of using pure spectra of the leaf and fungal compounds combined in spectral libraries. The signal could be decomposed and used to precisely interpret biochemical processes due to slight changes of the pure spectra composition.

Chapter 5 showed a deep learning approach serving as a detection algorithm for plant diseases on close-range hyperspectral images. A 3D convolutional neural network (3D-CNN)

was used to detect STB, YR and BR on different measurement days. An overall accuracy of 88.1 % with *F*1-scores between 0.79 and 0.91 was reached. The highest *F*1-score for the diseases was reached for BR (0.89) followed by STB (0.86) and YR (0.79). The highest accuracy for all classes was reached for the class healthy (0.91). Accuracy differences can be related to the different symptom types of the diseases and the data set composition. YR uredinia are surrounded by large chlorotic halos. Chlorotic spots are also the initial parts of the STB symptom development which might lead to misclassifications during disease detection. BR symptoms also formed chlorotic halos around the uredinia. The halos remained smaller and were more evenly distributed over the whole lamina which might explain the overall good accuracy for BR detection compared to STB and YR where specific symptom stages during pathogenesis, such as chlorosis in early and bleaching of the leaf in late pathogenesis, could appear in a similar way and lead to misclassifications. The results illustrated that the symptom always impacts the detection accuracy of a disease. In chapter 2 the biotrophic diseases were detected with a higher accuracy than the necrotrophic diseases. But with this 3D-CNN approach STB, a necrotrophic disease, was detected with a higher precision than YR, a biotrophic disease. The main difference is that we used supervised classification methods (with labeled training data) in chapter 2 and self-learning and improving deep learning approaches in chapter 5. Mahlein et al. (2018) indicated the high detection potentials for deep learning approaches. These approaches are not depending on the quality of labeled training data and CNNs frequently reach new accuracy records in disease recognition (He et al. 2015; Mahlein et al. 2018). The findings indicate the high potentials of deep learning approaches for the detection of plant diseases to unveil the (hidden) spectral fingerprint of diseases in the hyperspectral data of plant leaves.

The third objective (III) was the transduction of HI to the field scale to ensure an in-field disease detection and a knowledge transfer on hyperspectral data. Therefore, the ground-based vehicle (Phytobike) for canopy field measurements of winter wheat in combination with a suitable data analysis pipeline was developed.

As next objective (IV) the measurement platforms were extended to a UAV drone in combination with a hyperspectral camera. The UAV system enhanced the field measurements by an additional scale. With these measurement platforms hyperspectral measurements were

performed on the ground canopy scale at 50 cm and the UAV scale on 20 and 100 m over the crop canopy.

Chapter 6 displayed the centerpiece of this work (combining objectives (III)-(IV)). The two measurement platforms are capable in generating reproducible hyperspectral data that is comparable over different measurement dates. The Phytobike (ground canopy scale) was equipped with two hyperspectral cameras and an additional RGB camera, combined in a measurement cabin. The measurement cabin was covered by white canvas to avoid direct sun irradiation that causes shadow casting in the wheat canopy. The canvas procured that the light conditions in the cabin were diffuse and homogeneous. By using this construction, measurements could be performed in homogeneous cloudless and sunny conditions without the negative effect of shadow casting in the crop stand. If the issue of casting shadows can be reduced or is insignificant, sunny weather is preferable for ground measurements due to irradiation heterogeneities that might occur during measurements on a cloudy day. Various researchers performed their wheat canopy measurements during clear and sunny weather (Cao et al. 2013; Zheng et al. 2018a; Zheng et al. 2018b; Azadbakht et al. 2019) while others preferred overcast weather conditions to prevent issues from shadow casting (West et al. 2003; Whetton et al. 2018b).

Field data has to be processed and normalized to bring it into a form that allows to compare variabilities in the field trials on different measurement days. Varying illumination conditions during the day and on different measurement dates often lead to uninterpretable data (Bohnenkamp et al. 2019a). In this work, protocols were developed to keep the data generation process constant during vegetation period and also data normalization protocols were defined to consistently preprocess the data for later analysis. With these protocols it was possible to reduce the negative environmental field effects on the data such as changing illumination through cloud movement and solar altitude. The normalization procedure is based on a spectral reference panel with a known reflectance in the observed wavebands (Bohnenkamp et al. 2019a). A 50 % grey reference panel was preferred compared to panels with higher reflectance values to avoid an overexposure of images due to strong illumination. The panel was captured in each image on ground scale measurements with the line scanner and at the beginning of each flight with the UAV. The normalization with reference panels is an established method for field measurements. Various works used reference panels for

normalization of their data (Bravo et al. 2003; Cao et al. 2013; Yu et al. 2018; Zheng et al. 2018a; Zheng et al. 2018b). Future works should focus on an automated normalization of the data. If the current illumination is constantly measured, an online normalization of field data should be possible.

Close-scale field measurements for wheat disease detection so far were mostly performed using non-imaging spectrometers (Cao et al. 2013; Yu et al. 2018; Zheng et al. 2018a; Zheng et al. 2018b; Azadbakht et al. 2019). This kind of sensor provides hyperspectral data with a high spectral resolution. But a non-imaging sensor does not provide the possibility to do a pixel-wise analysis of images due to the lack of spatial information. The spectral information is averaged and depends on the measurement angle of the sensor optics (Mahlein 2016). Whetton et al. (2018b) used hyperspectral imaging push broom sensors for the detection of yellow rust in wheat fields. The scientists used a partial least squares regression (PLSR) with a leave-one-out cross-validation. The results indicated that yellow rust in the field can be detected by hyperspectral imaging sensors with further adaptation of analysis procedures. The measurements were performed in 0.3 m distance to the crop canopy. The image data was analyzed with pixel-wise classification, as they deployed a 100-point grid for image interpretation (Whetton et al. 2018b). The pixel-wise detection and identification of foliar diseases of wheat in the field using close-scale imaging in combination with hyperspectral imaging sensors (presented in chapter 6) is a new and promising approach in disease sensing (Bohnenkamp et al. 2019a).

On the UAV scale, the approach of imaging sensors is common and hyperspectral imaging sensors have been tested successfully (Abdulridha et al. 2019; Zhang et al. 2019). Abdulridha et al. (2019) used a DJI Matrice 600 to perform UAV-based hyperspectral images for detecting citrus canker disease in tangerine orchards. The used hyperspectral camera measured wavebands in the visible and near infrared range from 400-1000 nm. Regions of interest and vegetation indices were set to differentiate between healthy and infected trees. The UAV-based analysis reached an accuracy of 100 % for differing between healthy and diseased trees (Abdulridha et al. 2019). Zhang et al. (2019) used a UAV-based hyperspectral imaging system to detect yellow rust in wheat fields. Using snapshot-based hyperspectral imaging in combination with deep convolutional neural networks, the scientists reached an overall classification accuracy of 85 %. The UAV measurements were performed at 30 m altitude and

the spatial resolution was 2 cm per pixel (Zhang et al. 2019). This means that a single symptom cannot be solved into several pixels, but instead, a pixel-wise annotation was performed on the data. NDVI values were used to automatically label image pixels as soil, rust or healthy (Zhang et al. 2019). The results indicate that hyperspectral imaging is a promising tool for detecting diseases on the UAV scale. The UAV (and ground-scale) results presented in chapter 6 not only show a detection and classification of different crop canopy features, such as yellow rust incidence, but also a feature selection for yellow rust. The feature selection offers the opportunity to reduce the measured wavebands to a certain selection that is specific for the diseases of the desired crop. A sensor could be defined that is capable of detecting and differentiating the diseases that are relevant for decision-making in plant protection.

Imaging field data provide the possibility to annotate hyperspectral images for creating training data on the pixel and object level. The effectiveness of annotation is depending on the spatial resolution of the images. Based on the spatial resolution and the scale, a disease symptom might consist of several pixels that could be used for annotation. Several pixels could represent the spectral variability that is present in even one single symptom. In this hyperspectral data sets, various analysis approaches were performed to detect and quantify YR in the field. The accuracy of the different approaches was determined and evaluated in chapter 6. Classification results showed an accuracy for YR detection of more than 90 % on the ground canopy scale. In this regard, supervised classification methods like the spectral angle mapper and support vector machine were used. The future of data analysis will increasingly focus on deep learning approaches (Mahlein et al. 2018). Zhang et al. (2019) showed that deep convolutional neural networks reached better detection accuracies for UAV-based yellow rust detection than a random forest classifier (Zhang et al. 2019). Powerful data analysis pipelines have to be improved to introduce them for online analysis on field measurements.

The fifth objective (V) was the definition of a suitable measuring setup for future in-field disease detection. The perfect sensor for the detection of plant diseases in the field provides high resolution images with short image acquisition times. The measured wavebands are specific to the diseases that occur in a certain crop. It is combined with well-established analysis pipelines that are capable of fast online processing of the data and a fast online disease detection. This sensor also requires few human control and works autonomously in

the field with a high throughput. This sensor does not exist. But the technical progress offers interesting combinations for sensor approaches depending on what has to be measured. Two sensor systems were evaluated in the field. Both had strengths and weaknesses and the optimal sensor system at the current status quo can only be a compromise. The ground canopy measurement platform is much more sensitive as a detection of single disease symptoms is possible through the high resolution. The UAV system has a much higher throughput and the generated data size is smaller than the ground canopy data (due to the difference in the amount of measured wavebands). The UAV camera also had a shorter image acquisition time. As a suitable sensor combination, based on the experiments that are shown in this work, a low flying UAV in combination with a frame-based high spatial resolution camera system that is measuring as few wavebands as possible (based on a previous disease specific feature selection) is recommended. Based on the findings, the sensing of 15 equally distributed bands would be suitable. A tunable band configuration makes these sensors more versatile for other diseases in other crops or just the desired disease on different growth stages of the crop plant. The spatial resolution should be at 1 mm ground sampling distance to allow the detection of small symptoms and to neglect high-frequency noise caused by the complex surface of plants.

This work shows a continuous progression of hyperspectral measurements and analysis routines from controlled laboratory conditions to uncontrolled field conditions. The presented chapters pointed consecutive works and synergy effects that enabled the development of two measurement platforms in combination with a data analysis pipeline for a hyperspectral in-field detection of foliar diseases of wheat. The basic research focused on the spectral dynamic of the most important wheat diseases in Europe during their pathogenesis (chapter 2). The findings were used to generate a spectral library that combines the spectral characteristics of each disease. This spectral library was used to detect, identify and quantify the diseases under controlled conditions. Furthermore, a referencing of marker points was used to automatically perform a retrospective analysis of certain pixels back in time during the whole time series from late to early measuring days (chapter 3). This approach allowed to perform earliest detectability tests on diseased pixels where a symptom was not visible for the human eye. Based on the idea that human annotations could be error prone due to lack of objectivity, a detectability test based on pure spore spectra of yellow and brown rust was conducted (chapter 4). Also, the spectral mixed signal of a diseased leaf was fragmented to gain a deeper knowledge about how spectra are composed by different biochemical processes and leaf

properties. To test the potentials offered from deep learning, a 3D-CNN was used to detect the foliar diseases under controlled conditions (chapter 5). Based on these findings, two measurement platforms (ground-canopy and UAV) were conceptualized and introduced for field measurements (chapter 6). With both measurement platforms it was possible to gain reproducible data on different measurement days. Analysis routines were established and various approaches for data analysis were evaluated. The detection and identification of yellow rust was possible and the classification accuracy was high reaching 90 % on ground-canopy scale.

Further research continuously generates new progresses and both sensors and analysis methods improve rapidly. Hyperspectral sensors produce complex data but show high potentials for the selection of disease specific wavebands. These wavebands could be selected to define future sensors with a reduced number of wavebands that measure only the amount of data that is essential in the field. The in-field disease detection is an exciting discipline. On the one hand it is highly depending on the technical progress but on the other hand, it has tremendous potential to change and shape the way of future plant protection. The presented findings in this dissertation make a fundamental contribution to the future field approach of optical disease sensing systems.

8 References

Abdulridha, J.; Batuman, O.; Ampatzidis, Y. (2019): UAV-based remote sensing technique to detect citrus canker disease utilizing hyperspectral imaging and machine learning. In: *Remote Sensing* 11 (11), S. 1373. DOI: 10.3390/rs11111373.

Ashourloo, D.; Mobasheri, M.; Huete, A. (2014): Developing two spectral disease indices for detection of wheat leaf rust (*Puccinia triticina*). In: *Remote Sensing* 6 (6), S. 4723–4740. DOI: 10.3390/rs6064723.

Azadbakht, M.; Ashourloo, D.; Aghighi, H.; Radiom, S.; Alimohammadi, A. (2019): Wheat leaf rust detection at canopy scale under different LAI levels using machine learning techniques. In: *Computers and Electronics in Agriculture* 156, S. 119–128. DOI: 10.1016/j.compag.2018.11.016.

Behmann, J.; Acebron, K.; Emin, D.; Bennertz, S.; Matsubara, S.; Thomas, S. et al. (2018a): Specim IQ: Evaluation of a new, miniaturized handheld hyperspectral camera and its application for plant phenotyping and disease detection. In: *Sensors* 18 (2). DOI: 10.3390/s18020441.

Behmann, J.; Bohnenkamp, D.; Paulus, S.; Mahlein, A.-K. (2018b): Spatial referencing of hyperspectral images for tracing of plant disease symptoms. In: *Journal of Imaging* 4 (12), S. 143. DOI: 10.3390/jimaging4120143.

Behmann, J.; Mahlein, A.-K.; Rumpf, T.; Römer, C.; Plümer, L. (2015): A review of advanced machine learning methods for the detection of biotic stress in precision crop protection. In: *Precision Agriculture* 16 (3), S. 239–260. DOI: 10.1007/s11119-014-9372-7.

Behmann, J.; Steinrücken, J.; Plümer, L. (2014): Detection of early plant stress responses in hyperspectral images. In: *ISPRS Journal of Photogrammetry and Remote Sensing* 93, S. 98–111. DOI: 10.1016/j.isprsjprs.2014.03.016.

Berntsen, J.; Thomsen, A.; Schelde, K.; Hansen, O. M.; Knudsen, L.; Broge, N. et al. (2006): Algorithms for sensor-based redistribution of nitrogen fertilizer in winter wheat. In: *Precision Agriculture* 7 (2), S. 65–83. DOI: 10.1007/s11119-006-9000-2.

Bock, C. H.; Poole, G. H.; Parker, P. E.; Gottwald, T. R. (2010): Plant disease severity estimated visually, by digital photography and image analysis, and by hyperspectral imaging. In: *Critical Reviews in Plant Sciences* 29 (2), S. 59–107. DOI: 10.1080/07352681003617285.

Bohnenkamp, D.; Behmann, J.; Mahlein, A.-K. (2019a): In-field detection of yellow rust in wheat on the ground canopy and UAV scale. In: *Remote Sensing* 11 (21), S. 2495. DOI: 10.3390/rs11212495.

Bohnenkamp, D.; Kuska, M. T.; Mahlein, A.-K.; Behmann, J. (2019b): Hyperspectral signal decomposition and symptom detection of wheat rust diseases at the leaf scale using pure fungal spore spectra as reference. In: *Plant Pathology* 68 (6), S. 1188–1195. DOI: 10.1111/ppa.13020.

Bos, L.; Parlevliet, J. E. (1995): Concepts and terminology on plant/pest relationships: toward consensus in plant pathology and crop protection. In: *Annual Review of Phytopathology* 33, S. 69–102. DOI: 10.1146/annurev.py.33.090195.000441.

Boyd, L. A.; Ridout, C.; O'Sullivan, D. M.; Leach, J. E.; Leung, H. (2013): Plant-pathogen interactions: disease resistance in modern agriculture. In: *Trends in Genetics* 29 (4), S. 233–240. DOI: 10.1016/j.tig.2012.10.011.

Bravo, C.; Moshou, D.; West, J.; McCartney, A.; Ramon, H. (2003): Early disease detection in wheat fields using spectral reflectance. In: *Biosystems Engineering* 84 (2), S. 137–145. DOI: 10.1016/S1537-5110(02)00269-6.

Brugger, A.; Kuska, M. T.; Mahlein, A.-K. (2017): Impact of compatible and incompatible barley—*Blumeria graminis* f.sp. *hordei* interactions on chlorophyll fluorescence parameters. In: *Journal of Plant Diseases and Protection* 125, S. 177–186. DOI: 10.1007/s41348-017-0129-1.

Campbell, J. B. (2002): Introduction to remote sensing. 3. ed. London: Taylor & Francis.

Cao, X.; Luo, Y.; Zhou, Y.; Duan, X.; Cheng, D. (2013): Detection of powdery mildew in two winter wheat cultivars using canopy hyperspectral reflectance. In: *Crop Protection* 45, S. 124–131. DOI: 10.1016/j.cropro.2012.12.002.

Carter, G. A.; Knapp, A. K. (2001): Leaf optical properties in higher plants: linking spectral characteristics to stress and chlorophyll concentration. In: *American Journal of Botany* 88 (4), S. 677–684.

Chen, L.-C.; Papandreou, G.; Kokkinos, I.; Murphy, K.; Yuille, A. L. (2018): DeepLab: Semantic image segmentation with deep convolutional nets, atrous convolution, and fully connected CRFs. In: *IEEE Transactions on Pattern Analysis and Machine Intelligence* 40 (4), S. 834–848. DOI: 10.1109/TPAMI.2017.2699184.

Chen, T.; Zhang, J.; Chen, Y.; Wan, S.; Zhang, L. (2019): Detection of peanut leaf spots disease using canopy hyperspectral reflectance. In: *Computers and Electronics in Agriculture* 156, S. 677–683. DOI: 10.1016/j.compag.2018.12.036.

Clarke, K. C. (1986): Advances in geographic information systems. In: *Computers, Environment and Urban Systems* 10 (3-4), S. 175–184. DOI: 10.1016/0198-9715(86)90006-2.

Cortes, C.; Vapnik, V. (1995): Support-vector networks. In: *Machine Learning* 20 (3), S. 273–297. DOI: 10.1007/BF00994018.

De Boer, S. H.; López, M. M. (2012): New grower-friendly methods for plant pathogen monitoring. In: *Annual Review of Phytopathology* 50, S. 197–218. DOI: 10.1146/annurev-phyto-081211-172942.

Dean, R.; van Kan, J. A. L.; Pretorius, Z. A.; Hammond-Kosack, K. E.; Di Pietro, A.; Spanu, P. D. et al. (2012): The Top 10 fungal pathogens in molecular plant pathology. In: *Molecular Plant Pathology* 13 (4), S. 414–430. DOI: 10.1111/J.1364-3703.2011.00783.X.

Devadas, R.; Lamb, D. W.; Simpfendorfer, S.; Backhouse, D. (2009): Evaluating ten spectral vegetation indices for identifying rust infection in individual wheat leaves. In: *Precision Agriculture* 10 (6), S. 459–470. DOI: 10.1007/s11119-008-9100-2.

Dracatos, P. M.; Haghdoust, R.; Singh, D.; Park, R. F. (2018): Exploring and exploiting the boundaries of host specificity using the cereal rust and mildew models. In: *The New Phytologist* 218 (2), S. 453–462. DOI: 10.1111/nph.15044.

Dugyala, S.; Borowicz, P.; Acevedo, M. (2015): Rapid protocol for visualization of rust fungi structures using fluorochrome Uvitex 2B. In: *Plant Methods* 11 (54). DOI: 10.1186/s13007-015-0096-0.

Dushnicky, L. G.; Ballance, G. M.; Sumner, M. J.; MacGregor, A. W. (1998a): Detection of infection and host responses in susceptible and resistant wheat cultivars to a toxin-producing isolate of Pyrenophora tritici-repentis. In: *Canadian Journal of Plant Pathology* 20 (1), S. 19–27. DOI: 10.1080/07060669809500441.

Dushnicky, L. G.; Ballance, G. M.; Sumner, M. J.; MacGregor, A. W. (1998b): The role of lignification as a resistance mechanism in wheat to a toxin-producing isolate of Pyrenophora tritici-repentis. In: *Canadian Journal of Plant Pathology* 20 (1), S. 35–47. DOI: 10.1080/07060669809500443.

Duveiller, E.; Kandel, Y. R.; Sharma, R. C.; Shrestha, S. M. (2005): Epidemiology of foliar blights (spot blotch and tan spot) of wheat in the plains bordering the himalayas. In: *Phytopathology* 95 (3), S. 248–256. DOI: 10.1094/PHYTO-95-0248.

Elvidge, C. D. (1990): Visible and near infrared reflectance characteristics of dry plant materials. In: *International Journal of Remote Sensing* 11 (10), S. 1775–1795. DOI: 10.1080/01431169008955129.

Fernández-Quintanilla, C.; Peña, J. M.; Andújar, D.; Dorado, J.; Ribeiro, A.; López-Granados, F. (2018): Is the current state of the art of weed monitoring suitable for site-specific weed management in arable crops? In: *Weed Research* 58 (4), S. 259–272. DOI: 10.1111/wre.12307.

Gates, D. M.; Keegan, H. J.; Schleter, J. C.; Weidner, V. R. (1965): Spectral properties of plants. In: *Applied Optics* 4 (1), S. 11–20. DOI: 10.1364/AO.4.000011.

Gay, A.; Thomas, H.; Roca, M.; James, C.; Taylor, J.; Rowland, J.; Ougham, H. (2008): Nondestructive analysis of senescence in mesophyll cells by spectral resolution of protein synthesis-dependent pigment metabolism. In: *The New Phytologist* 179 (3), S. 663–674. DOI: 10.1111/j.1469-8137.2008.02412.x.

Golhani, Kamlesh; Balasundram, Siva K.; Vadamalai, G.; Pradhan, B. (2018): A review of neural networks in plant disease detection using hyperspectral data. In: *Information Processing in Agriculture* 5 (3), S. 354–371. DOI: 10.1016/j.inpa.2018.05.002.

Harrington, B. J. (2009): The staining of oocysts of cryptosporidium with the fluorescent brighteners Uvitex 2B and Calcofluor White. In: *Laboratory Medicine* 40 (4), S. 219–223. DOI: 10.1309/LM8PT49NZVVYONCB.

Harrington, B. J.; Hageage, G. J. (2003): Calcofluor White: A review of its uses and applications in clinical mycology and parasitology. In: *Laboratory Medicine* 34 (5), S. 361–367. DOI: 10.1309/EPH2TDT8335GH0R3.

He, K.; Zhang, X.; Ren, S.; Sun, J.: Deep residual learning for image recognition.

Heim, R.; Jürgens, N.; Große-Stoltenberg, A.; Oldeland, J. (2015): The effect of epidermal structures on leaf spectral signatures of ice plants (*Aizoaceae*). In: *Remote Sensing* 7 (12), S. 16901–16914. DOI: 10.3390/rs71215862.

Heim, R. H. J.; Wright, I. J.; Allen, A. P.; Geedicke, I.; Oldeland, J. (2019): Developing a spectral disease index for myrtle rust (*Austropuccinia psidii*). In: *Plant Pathology* 68 (4), S. 738–745. DOI: 10.1111/ppa.12996.

Hillnhütter, C.; Mahlein, A.-K.; Sikora, R. A.; Oerke, E.-C. (2011): Remote sensing to detect plant stress induced by *Heterodera schachtii* and *Rhizoctonia solani* in sugar beet fields. In: *Field Crops Research* 122 (1), S. 70–77. DOI: 10.1016/j.fcr.2011.02.007.

Huang, L.; Ding, W.; Liu, W.; Zhao, J.; Huang, W.; Xu, C. et al. (2019): Identification of wheat powdery mildew using in-situ hyperspectral data and linear regression and support vector machines. In: *Journal of Plant Pathology* 42, S. 3264. DOI: 10.1007/s42161-019-00334-2.

Iori, A.; Scala, V.; Cesare, D.; Pinzari, F.; D'Egidio, M. G.; Fanelli, C. et al. (2015): Hyperspectral and molecular analysis of *Stagonospora nodorum* blotch disease in durum wheat. In: *European Journal of Plant Pathology* 141 (4), S. 689–702. DOI: 10.1007/s10658-014-0571-x.

Jay, S.; Bendoula, R.; Hadoux, X.; Féret, J.-B.; Gorretta, N. (2016): A physically-based model for retrieving foliar biochemistry and leaf orientation using close-range imaging spectroscopy. In: *Remote Sensing of Environment* 177, S. 220–236. DOI: 10.1016/j.rse.2016.02.029.

Kong, W.; Zhang, C.; Huang, W.; Liu, F.; He, Y. (2018): Application of hyperspectral imaging to detect *Sclerotinia sclerotiorum* on oilseed rape stems. In: *Sensors* 18 (1), S. 123. DOI: 10.3390/s18010123.

Kruse, F. A.; Lefkoff, A. B.; Boardman, J. W.; Heidebrecht, K. B.; Shapiro, A. T.; Barloon, P. J.; Goetz, A.F.H. (1993): The spectral image processing system (SIPS)—interactive visualization and analysis of imaging spectrometer data. In: *Remote Sensing of Environment* 44 (2-3), S. 145–163. DOI: 10.1016/0034-4257(93)90013-N.

Kuska, M. T.; Wahabzada, M.; Leucker, M.; Dehne, H.-W.; Kersting, K.; Oerke, E.-C. et al. (2015): Hyperspectral phenotyping on the microscopic scale: towards automated characterization of plant-pathogen interactions. In: *Plant Methods* 11 (28). DOI: 10.1186/s13007-015-0073-7.

Leucker, M.; Mahlein, A.-K.; Steiner, U.; Oerke, E.-C. (2016): Improvement of lesion phenotyping in *Cercospora beticola*-sugar beet interaction by hyperspectral imaging. In: *Phytopathology* 106 (2), S. 177–184. DOI: 10.1094/PHYTO-04-15-0100-R.

Liakos, K. G.; Busato, P.; Moshou, D.; Pearson, S.; Bochtis, D. (2018): Machine learning in agriculture: A review. In: *Sensors* 18 (8), S. 2674. DOI: 10.3390/s18082674.

Liebisch, F.; Kirchgessner, N.; Schneider, D.; Walter, A.; Hund, A. (2015): Remote, aerial phenotyping of maize traits with a mobile multi-sensor approach. In: *Plant Methods* 11, S. 9. DOI: 10.1186/s13007-015-0048-8.

Lovell, D. J.; Hunter, T.; Powers, S. J.; Parker, S. R.; van den Bosch, F. (2004): Effect of temperature on latent period of septoria leaf blotch on winter wheat under outdoor conditions. In: *Plant Pathology* 53 (2), S. 170–181. DOI: 10.1111/j.0032-0862.2004.00983.x.

Lowe, A.; Harrison, N.; French, A. P. (2017): Hyperspectral image analysis techniques for the detection and classification of the early onset of plant disease and stress. In: *Plant Methods* 13, S. 80. DOI: 10.1186/s13007-017-0233-z.

Mahlein, A.-K. (2016): Plant disease detection by imaging sensors - parallels and specific demands for precision agriculture and plant phenotyping. In: *Plant Disease* 100 (2), S. 241–251. DOI: 10.1094/PDIS-03-15-0340-FE.

Mahlein, A.-K.; Alisaac, E.; Al Masri, A.; Behmann, J.; Dehne, H.-W.; Oerke, E.-C. (2019): Comparison and combination of thermal, fluorescence, and hyperspectral imaging for monitoring *Fusarium* head blight of wheat on spikelet scale. In: *Sensors* 19 (10), S. 2281. DOI: 10.3390/s19102281.

Mahlein, A.-K.; Rumpf, T.; Welke, P.; Dehne, H.-W.; Plümer, L.; Steiner, U.; Oerke, E.-C. (2013): Development of spectral indices for detecting and identifying plant diseases. In: *Remote Sensing of Environment* 128, S. 21–30.

Mahlein, A.-K.; Steiner, U.; Dehne, H.-W.; Oerke, E.-C. (2010): Spectral signatures of sugar beet leaves for the detection and differentiation of diseases. In: *Precision Agriculture* 11 (4), S. 413–431. DOI: 10.1007/s11119-010-9180-7.

Mahlein, A.-K.; Steiner, U.; Hillnhütter, C.; Dehne, H.-W.; Oerke, E.-C. (2012): Hyperspectral imaging for small-scale analysis of symptoms caused by different sugar beet diseases. In: *Plant Methods* 8 (3). DOI: 10.1186/1746-4811-8-3.

Mahlein, A-K; Kuska, M. T.; Behmann, J.; Polder, G.; Walter, A. (2018): Hyperspectral sensors and imaging technologies in phytopathology: State of the art. In: *Annual Review of Phytopathology* 56, S. 535–558. DOI: 10.1146/annurev-phyto-080417-050100.

Miedaner, T. (Hg.) (2018): Management von Pilzkrankheiten im Ackerbau. Erkennen, vorbeugen, bekämpfen. Unter Mitarbeit von Werner Beyer und Kerstin Flath. Erling Verlag GmbH & Co. KG. 1. Auflage. Clenze: Agrimedia.

Moshou, D.; Bravo, C.; West, J.; Wahlen, S.; McCartney, A.; Ramon, H. (2004): Automatic detection of 'yellow rust' in wheat using reflectance measurements and neural networks. In: *Computers and Electronics in Agriculture* 44 (3), S. 173–188. DOI: 10.1016/j.compag.2004.04.003.

Nutter, F. W.; Esker, P. D.; Coelho Netto, R., A. (2006): Disease assessment concepts and the advancements made in improving the accuracy and precision of plant disease data. In: *European Journal of Plant Pathology* 115 (1), S. 95–103. DOI: 10.1007/s10658-005-1230-z.

Nutter, F. W.; Schultz, P. M. (1995): Improving the accuracy and precision of disease assessments: selection of methods and use of computer-aided training programs. In: *Canadian Journal of Plant Pathology* 17 (2), S. 174–184. DOI: 10.1080/07060669509500709.

Oerke, E.-C. (2006): Crop losses to pests. In: *Journal of Agricultural Science* 144 (1), S. 31–43. DOI: 10.1017/S0021859605005708.

Pandey, P.; Ge, Y.; Stoerger, V.; Schnable, J. C. (2017): High throughput *In vivo* analysis of plant leaf chemical properties using hyperspectral imaging. In: *Frontiers in plant science* 8 (1348). DOI: 10.3389/fpls.2017.01348.

Parnell, S.; van den Bosch, F.; Gottwald, T.; Gilligan, C. A. (2017): Surveillance to inform control of emerging plant diseases: An epidemiological perspective. In: *Annual Review of Phytopathology* 55, S. 591–610. DOI: 10.1146/annurev-phyto-080516-035334.

Reckleben, Y. (2014): Sensoren für die Stickstoffdüngung - Erfahrungen in 12 Jahren praktischem Einsatz. In: *Journal für Kulturpflanzen* 66 (2), S. 42–47. DOI: 10.5073/JFK.2014.02.02.

Robert B. (2016): Robots poised to revolutionise agriculture. In: *Industrial Robot: An International Journal* 43 (5), S. 450–456. DOI: 10.1108/IR-05-2016-0142.

Roosjen, P.; Suomalainen, J.; Bartholomeus, H.; Clevers, J. (2016): Hyperspectral reflectance anisotropy measurements using a pushbroom spectrometer on an unmanned aerial vehicle—results for barley, winter wheat, and potato. In: *Remote Sensing* 8 (11), S. 909. DOI: 10.3390/rs8110909.

Sandmeier, S.; Müller, C.; Hosgood, B.; Andreoli, G. (1998): Physical mechanisms in hyperspectral BRDF data of grass and watercress. In: *Remote Sensing of Environment* 66 (2), S. 222–233. DOI: 10.1016/S0034-4257(98)00060-1.

Seelig, H.-D.; Hoehn, A.; Stodieck, L. S.; Klaus, D. M.; Adams III, W. W.; Emery, W. J. (2008): The assessment of leaf water content using leaf reflectance ratios in the visible, near-, and short-wave-infrared. In: *International Journal of Remote Sensing* 29 (13), S. 3701–3713. DOI: 10.1080/01431160701772500.

Steinberg, G. (2015): Cell biology of *Zymoseptoria tritici*: Pathogen cell organization and wheat infection. In: *Fungal Genetics and Biology* 79, S. 17–23. DOI: 10.1016/j.fgb.2015.04.002.

Steiner, U.; Bürling, K.; Oerke, E.-C. (2008): Sensorik für einen präzisierten Pflanzenschutz. In: *Gesunde Pflanzen* 60 (4), S. 131–141. DOI: 10.1007/s10343-008-0194-2.

Strelkov, S. E.; Lamari, L. (2003): Host–parasite interactions in tan spot [*Pyrenophora tritici-repentis*] of wheat. In: *Canadian Journal of Plant Pathology* 25 (4), S. 339–349. DOI: 10.1080/07060660309507089.

Suomalainen, J.; Anders, N.; Iqbal, S.; Roerink, G.; Franke, J.; Wenting, P. et al. (2014): A lightweight hyperspectral mapping system and photogrammetric processing chain for unmanned aerial vehicles. In: *Remote Sensing* 6 (11), S. 11013–11030. DOI: 10.3390/rs61111013.

Suprem, A.; Mahalik, N.; Kim, K. (2013): A review on application of technology systems, standards and interfaces for agriculture and food sector. In: *Computer Standards & Interfaces* 35 (4), S. 355–364. DOI: 10.1016/j.csi.2012.09.002.

Thomas, S.; Kuska, M. T.; Bohnenkamp, D.; Brugger, A.; Alisaac, E.; Wahabzada, M. et al. (2018): Benefits of hyperspectral imaging for plant disease detection and plant protection: a technical perspective. In: *Journal of Plant Diseases and Protection* 125 (1), S. 5–20. DOI: 10.1007/s41348-017-0124-6.

Tomas, A. (1987): Cultivar-specific toxicity of culture filtrates of *Pyrenophora tritici-repentis*. In: *Phytopathology* 77 (9), S. 1337–1340. DOI: 10.1094/Phyto-77-1337.

Torriani, S. F. F.; Melichar, J. P. E.; Mills, C.; Pain, N.; Sierotzki, H.; Courbot, M. (2015): *Zymoseptoria tritici*: A major threat to wheat production, integrated approaches to control. In: *Fungal Genetics and Biology* 79, S. 8–12. DOI: 10.1016/j.fgb.2015.04.010.

Wahabzada, M.; Mahlein, A.-K.; Bauckhage, C.; Steiner, U.; Oerke, E.-C.; Kersting, K. (2015): Metro maps of plant disease dynamics--automated mining of differences using hyperspectral images. In: *PloS one* 10 (1). DOI: 10.1371/journal.pone.0116902.

Wahabzada, M.; Mahlein, A.-K.; Bauckhage, C.; Steiner, U.; Oerke, E.-C.; Kersting, K. (2016): Plant phenotyping using probabilistic topic models: Uncovering the hyperspectral language of plants. In: *Scientific reports* 6 (22482). DOI: 10.1038/srep22482.

Wang, E.; Dong, C.; Park, R. F.; Roberts, T. H. (2018): Carotenoid pigments in rust fungi: Extraction, separation, quantification and characterisation. In: *Fungal Biology Reviews* 32 (3), S. 166–180. DOI: 10.1016/j.fbr.2018.02.002.

Wendel, A.; Underwood, J. (2017): Illumination compensation in ground based hyperspectral imaging. In: *ISPRS Journal of Photogrammetry and Remote Sensing* 129, S. 162–178. DOI: 10.1016/j.isprsjprs.2017.04.010.

West, J. S.; Bravo, C.; Oberti, R.; Lemaire, D.; Moshou, D.; McCartney, H. A. (2003): The potential of optical canopy measurement for targeted control of field crop diseases. In: *Annual Review of Phytopathology* 41, S. 593–614. DOI: 10.1146/annurev.phyto.41.121702.103726.

Whetton, R. L.; Hassall, K. L.; Waine, T. W.; Mouazen, A. M. (2018a): Hyperspectral measurements of yellow rust and fusarium head blight in cereal crops: Part 1: Laboratory study. In: *Biosystems Engineering* 166, S. 111–115. DOI: 10.1016/j.biosystemseng.2017.11.008.

Whetton, R. L.; Waine, T. W.; Mouazen, A. M. (2018b): Hyperspectral measurements of yellow rust and fusarium head blight in cereal crops: Part 2: On-line field measurement. In: *Biosystems Engineering* 167, S. 144–158.

Yao, Z.; Lei, Y.; He, D. (2019): Early visual detection of wheat stripe rust using visible/near-infrared hyperspectral imaging. In: *Sensors* 19 (952). DOI: 10.3390/s19040952.

Yu, K.; Anderegg, J.; Mikaberidze, A.; Karisto, P.; Mascher, F.; McDonald, B. A. et al. (2018): Hyperspectral canopy sensing of wheat septoria tritici blotch disease. In: *Frontiers in plant science* 9, S. 1195. DOI: 10.3389/fpls.2018.01195.

Yuan, L.; Huang, Y.; Loraamm, R. W.; Nie, C.; Wang, J.; Zhang, J. (2014): Spectral analysis of winter wheat leaves for detection and differentiation of diseases and insects. In: *Field Crops Research* 156, S. 199–207. DOI: 10.1016/j.fcr.2013.11.012.

Zhang, X.; Han, L.; Dong, Y.; Shi, Y.; Huang, W.; Han, L. et al. (2019): A deep learning-based approach for automated yellow rust disease detection from high-resolution hyperspectral UAV images. In: *Remote Sensing* 11 (13), S. 1554. DOI: 10.3390/rs11131554.

Zheng, Q.; Huang, W.; Cui, X.; Dong, Y.; Shi, Y.; Ma, H.; Liu, L. (2018a): Identification of wheat yellow rust using optimal three-band spectral indices in different growth stages. In: *Sensors* 19 (1), S. 35. DOI: 10.3390/s19010035.

Zheng, Q.; Huang, W.; Cui, X.; Shi, Y.; Liu, L. (2018b): New spectral index for detecting wheat yellow rust using sentinel-2 multispectral imagery. In: *Sensors* 18 (3), S. 868. DOI: 10.3390/s18030868.

Zhu, H.; Chu, B.; Zhang, C.; Liu, F.; Jiang, L.; He, Y. (2017): Hyperspectral imaging for presymptomatic detection of tobacco disease with successive projections algorithm and machine-learning classifiers. In: *Scientific reports* 7 (1), S. 4125. DOI: 10.1038/s41598-017-04501-2.

9 Acknowledgements

Ich möchte mich ganz herzlich bei xarvio™ - Digital Farming Solutions für die Finanzierung dieses Projektes bedanken.

Herzlichen Dank an Prof. Dr. Jens Léon für das Begutachten meiner Dissertation als Zweitprüfer.

Ich bedanke mich außerdem bei allen Mitarbeitern des INRES Pflanzenkrankheiten und Pflanzenschutz für die tollen Jahre in der Nussallee, ganz besonders bei Caro, Kerstin und Jenny.

Ich bedanke mich auch bei Frau Dr. Steiner und Herrn Dr. Oerke für die fachliche Unterstützung, die konstruktiven Diskussionen und Ratschläge sowohl im Labor, wie auch zu jeder Zeit zwischen Tür und Angel.

Danke Jan für die gute Zusammenarbeit im Projekt und all die Hilfestellungen und Geduld.

Vielen Dank an meine Familie, und besonders an meine Eltern Angelika und Günter, die mich all die Jahre bedingungslos unterstützt haben und auf die ich mich immer verlassen kann.

Mein ganz besonderer Dank gilt Anne für die tolle Möglichkeit bei ihr zu promovieren. Danke für all die Hilfestellungen, Anleitung und Möglichkeiten zur Entfaltung, die Du mir während meiner Promotion hast zuteilwerden lassen. Ich habe die Jahre in diesem Projekt zu jeder Zeit genossen und werde sie besonders in Erinnerung behalten. Dein Beispiel an fachlicher Kompetenz, Engagement und einem besonderen Führungsstil nehme ich mir als Vorbild.